

Conditions Favorable for the Occurrence of Trapped Mountain Lee Waves Downstream of O‘ahu

A THESIS SUBMITTED TO THE GRADUATE DIVISION OF THE UNIVERSITY OF
HAWAI‘I AT MĀNOA IN PARTIAL FULFILLMENT OF THE REQUIREMENTS FOR THE

DEGREE OF

MASTER OF SCIENCE

IN

METEOROLOGY

May 2015

By

Liye Li

Thesis Committee:

Yi-leng Chen, Chairperson

Michael Bell

Jennifer Griswold

Gary Barnes

Keywords: trapped lee wave, synoptic conditions, scorer parameter, model simulation

ACKNOWLEDGEMENTS

I am grateful to my advisor Dr. Yi-leng Chen for his time and dedication towards my research progress and the completion of my thesis. I would also like to thank my committee members Dr. Gary Barnes, Dr. Michael Bell, and Dr. Jennifer Griswold for their suggestions that led to improvements in my thesis.

I would like to thank Chin-Ying Chen and Feng Hsiao for their advice on many technical issues.

ABSTRACT

The purpose of this study is to determine the synoptic conditions necessary for trapped lee wave development over O‘ahu. The study also shows that the high-resolution mesoscale numerical models could possibly provide valuable numerical guidance for the onset, development and dissipation of trapped lee wave events in Hawai‘i.

The occurrence of trapped lee wave clouds is possible in Hawai‘i, especially downstream of the island of O‘ahu. The Ko‘olau and Wai‘anae mountain ranges of O‘ahu are oriented NW-SE. The pre-frontal southwesterly wind in winter has a large wind component perpendicular to these mountain ranges. With the presence of an inversion aloft, trapped lee waves may occur during the wintertime. In the summer time, northeast trade wind is persistent and trapped lee wave event is relatively rare.

In this study, environmental conditions related to the development of three trapped lee wave events (27 January, 2010—TRAP1; 24 January—TRAP2, 2003; 26 January, 2014—TRAP3, 25 August, 1977) are analyzed using soundings, charts, satellite images. The available model input datasets for the summer case in 25 August, 1977 is ERA-40 in the resolution of $2.5^{\circ} \times 2.5^{\circ}$, which is not enough to simulate high-resolution model in 1-km. With input analysis datasets in the resolution of $1.25^{\circ} \times 1.25^{\circ}$, the three wintertime events are successfully predicted by the high-resolution WRF model. Among them, TRAP1 and TRAP2 are initialized using the National Centers for Environmental

Prediction (NCEP) Climate Forecast System Reanalysis (CFSR), and TRAP3 is initialized with NCEP Climate Forecast System Version 2 (CFSv2) output.

Results from a WRF model simulation with a horizontal 1-km grid indicate that the trapped lee waves are most significant just beneath the inversion. There are several common factors involved in the occurrence of these trapped mountain wave events: 1) the presence of a well-defined inversion above the ridge tops; 2) abundant low-level moisture; 3) strong low-level winds with Froude Number (Fr) > 1 impinging on the mountain ranges; and (4) wind shear with increasing wind speed with respect to height through the inversion. A strong pre-frontal southwesterly flow is the typical synoptic setting for the occurrence of trapped mountain waves in winter, whereas in the summer months the presence of an upper-level disturbance with easterly winds aloft is a necessary prerequisite.

The vertical wind profile is the key element to determine whether trapped lee waves or downslope winds form. None of the trapped lee wave events in winter or summer have a critical level. If a critical level exists between 500 hPa to 300 hPa, and wind decreases with height in the low level, a downslope wind storm or mountain wave may occur instead of trapped lee waves. Sensitivity tests for the 27 January, 2010 case are performed with reduced relative humidity (RH). With lower RH, trapped lee waves have smaller amplitudes and shorter wavelengths suggesting a latent heat release feedback to the environmental flow.

Contents

ACKNOWLEDGEMENTS	i
ABSTRACT	ii
List of Figures	vi
List of Tables.....	x
Chapter 1	- 1 -
Introduction	- 1 -
1.1 Background	- 1 -
1.2 Climatology background and topography	- 3 -
1.3 Objectives.....	- 4 -
Chapter 2	- 6 -
Overview of Mountain Waves.....	- 6 -
2.1 Airflow Interactions with Terrain.....	- 6 -
2.2 Linear Theoretical Framework of Trapped Lee Waves.....	- 7 -
2.3 Nonlinear Mountain Waves.....	- 10 -
Chapter 3	- 13 -
Data and Method	- 13 -
3.1 Synoptic Data	- 13 -
3.2 Model Description.....	- 14 -
Chapter 4	- 16 -
Synoptic Analysis of Trapped Lee Wave Event in Winter	- 16 -
4.1 TRAP1---26-27 January, 2010	- 16 -
4.2 TRAP2---24-25 January, 2003	- 17 -
4.3 TRAP3---26 January, 2014	- 19 -
Chapter 5	- 21 -
Model Simulation of Trapped Lee Wave in Winter	- 21 -
5.1 TRAP1---26-27 January, 2010	- 21 -

5.1.1 Wave Structure	- 21 -
5.1.2 Time Series of the Upstream Flow	- 23 -
5.2 TRAP2---24-25 January, 2003	- 26 -
5.2.1 Wave Structure	- 26 -
5.2.2 Time Series of Upstream Flow	- 27 -
5.3 TRAP3--26 January, 2014	- 28 -
5.3.1 Wave Structure	- 28 -
5.3.2 Time Series of Upstream Flow	- 29 -
5.4 Summary for model simulated wave structure and upstream flow	- 30 -
5.5 Trapped lee waves over the Hawaiian Islands.....	- 31 -
Chapter 6	- 34 -
A Trapped Lee Wave Event in Summer.....	- 34 -
6.1 Synoptic Conditions for A Trapped Lee Wave Event.....	- 34 -
6.2 A Comparison of Trapped Lee Waves in Winter and Summer.....	- 35 -
Chapter 7	- 37 -
Comparison between Trapped Lee Waves and Other Type of Mountain Waves	- 37 -
7.1 Downslope Wind Storm: 14-15 February, 2001	- 37 -
7.2 Mountain Waves: 31 July, 2013	- 38 -
7.3 Common and Different Factors for Trapped Lee Waves and Other Wave Types	- 40 -
Chapter 8	- 42 -
Impact of Latent Heat Release	- 42 -
Chapter 9	- 45 -
Conclusion.....	- 45 -
9.1 Summary of Trapped Lee Wave Development Conditions.....	- 45 -
9.2 Implications for Forecasting.....	- 48 -
References	- 51 -

List of Figures

Figure 1. ARW Elevation contour over the island of O‘ahu in the unit of meters.	56 -
Figure 2. Climatological high pressure system and wind pattern over the Hawaiian Islands in January (upper Figure) and July (bottom Figure) in the unit of hPa. From Atlas of Hawai‘i. Chapter 2 the Physical Environment. (Schroeder, 1993)	57 -
Figure 3. Features of airflow across a long mountain range (Wallington, 1960).....	58 -
Figure 4. Streamlines in steady airflow over an infinite series of sinusoidal ridges when $N=0.01 \text{ s}^{-1}$, $U=15 \text{ m s}^{-1}$. m is the vertical wavenumber of mountain waves. The flow is from left to right, and the wavelengths of the topography are (a) 8 km (case $m^2 < 0$) (b) 40 km (case $m^2 > 0$). The lowest streamline coincides with the topography. (Durrán, 2003).....	59 -
Figure 5. Streamlines in steady airflow over an isolated mountain series as predicted by linear theory when (a) mountain width is 10 km, N is constant, and $Nh/U = 0.06$ (b) mountain width is 5 km, N is constant throughout each of two layers such that between the surface and 3 km $Nh/U = 0.06$, and above 3 km $Nh/U = 0.24$	60 -
Figure 6. Model domain nesting for trapped lee wave cases in winter, 27 January, 2010 and 25 January, 2003. The resolution for three domains is 9 km, 3 km, and 1 km respectively.	62 -
Figure 7. GOES-west visible satellite imagery for the Hawaiian Islands from early to mature stage of the trapped lee wave case on 27 January, 2010. (from Mauna Kea Weather Center)-	64 -
Figure 8. Surface maps of 26-27 January, 2010 trapped lee wave case at different stages. The unit of pressure is hPa.	65 -
Figure 9. Sounding and wind profile at Lihue during different stages at the trapped lee wave case in 26-27 January 2010. (From University of Wyoming)	66 -
Figure 10. GOES-10 VIS satellite imagery for the trapped mountain lee wave case in 24-25 January 2003.....	67 -
Figure 11. Synoptic pattern of surface pressure (shading) and wind (vector) in the unit of hPa at different wave evolution phase.....	68 -
Figure 12. Sounding and wind profile at Lihue during different stage in the trapped lee wave case on 24-25 January 2003. (From University of Wyoming)	69 -

Figure 13. Surface maps from 26 Jan, 2014 trapped lee wave case in different stages. The unit of pressure is hPa. - 71 -

Figure 14. GOES-10 VIS Imagery in 1km resolution from Mauna Kea Weather Center (MKWC). - 72 -

Figure 15. Skew T-log p soundings and vertical wind profiles from Lihue station at (left figure) 1200 UTC, 26 January, 2014; (right figure) 0000 UTC, 27 January, 2014..... - 73 -

Figure 16. The wind vector at 850 hPa at mature stage for the case in (a) 0300 UTC, 27 January, 2010 and (b) 2000 UTC, 24 January, 2003. - 74 -

Figure 17. Model simulated vertical motion at 850 hPa for the trapped lee wave case of 26-27 January, 2010. The unit of vertical motion is m s^{-1} with upward motion being positive. - 75 -

Figure 18. Equivalent potential temperature θ (contour) and relative humidity (shading) during the different phases of 27 January, 2010 trapped lee wave case. White dashed line is the area with relative humidity greater than 90%, where the clouds are very likely to occur. - 76 -

Figure 19. Time series of upstream airflow for the case on 26-27 Jan, 2010 on different properties..... - 78 -

Figure 20. Model simulated vertical motion at 850 hPa for the trapped lee wave case of 24-25 January, 2003. The unit of vertical motion is m s^{-1} with upward motion being positive. - 79 -

Figure 21. Equivalent potential temperature θ (contour) and relative humidity (shading) during the different phases of 24-25 January, 2003 trapped lee wave case..... - 80 -

Figure 22. Time series of upstream airflow for the case on 24-25 Jan, 2003 on different properties..... - 81 -

Figure 23. Model simulated vertical motion at 850 hPa for the trapped lee wave case of 26 January 2014. The unit of vertical motion is m s^{-1} with upward motion being positive. - 83 -

Figure 24. Equivalent potential temperature θ (contour) and relative humidity (shading) during the different phase of 26 January, 2014 trapped lee wave case..... - 84 -

Figure 25. Time series of upstream airflow for the TRAP4 (26 Jan, 2014) case on different properties..... - 85 -

Figure 26. Trapped lee waves over other Hawaiian Islands..... - 87 -

Figure 27. SMS-2 1 km VIS image for the trapped lee wave case in 25 August, 1977. K—Kaua‘i, O--O‘ahu, Mo--Moloka‘i, M--Maui and H--Hawai‘i. - 88 -

Figure 28. Geo-potential height (shading) and wind pattern (barb) in low, middle and upper level before and during the development of the trapped lee wave case on 25 August, 1977. One pennant, full barb and half barb represent 20, 4 and 2 m s⁻¹, respectively. - 89 -

Figure 29. Skew T-log p soundings and vertical wind profiles from Lihue station. - 90 -

Figure 30. Surface analyses for 0000 UTC on (a) 13 and (b) 14 February 2001 (adapted from the subjective analyzes by forecaster at the NWS Forecast Office in Honolulu). Isobars are every 4 hPa. (From Yongxin’s paper) - 91 -

Figure 31. Observed, and RSM-LSM and MSM-LSM simulated 10m (left) wind speeds (m s⁻¹) and (right) wind direction at Kahuku, O‘ahu and Bellows O‘ahu. (From Yongxin Zhang’s paper) - 92 -

Figure 32. Skew-T chart (courtesy of the Department of Atmospheric Science, University of Wyoming; <http://weather.uwyo.edu/upperair/sounding.html>) for Lihue, Kaua‘i at 0000 UTC, 15 February, 2001..... - 93 -

Figure 33. Model simulated vertical motion in 850 hPa for the mountain wave case on 01 August, 2001. The corresponding moment is 0100 UTC, 15 February 2001. The unit of vertical motion is m s⁻¹ with upward motion being positive. - 94 -

Figure 34. MODIS satellite images at 2337 UTC, 31 July, 2013 over the island of O‘ahu.... - 95 -

Figure 35. Surface analyses for 1800 UTC on 30 July, 2013 (from the subjective analyzes by forecaster at the NWS Forecast Office in Honolulu). Isobars are every 4 hPa. - 96 -

Figure 36. Geopotential height (shading) and horizontal wind barbs at 850 hPa over the Hawaiian Islands in 0000 UTC, 1 August, 2013..... - 97 -

Figure 37. Skew-T chart (courtesy of the Department of Atmospheric Science, University of Wyoming; <http://weather.uwyo.edu/upperair/sounding.html>) for Lihue, Kaua‘i at 0000 UTC, 01 August, 2013. - 98 -

Figure 38. Model simulated (a) vertical motion at 850 hPa, (b) relative humidity and potential temperature for the mountain wave case ob 01 August, 2013. The corresponding moment is

0000 UTC, 01 August 2013. The unit of vertical motion is m s^{-1} with upward motion being positive. - 99 -

Figure 39. Model simulated cross-barrier wind speed (shading and contour) along vertical cross sections for trapped lee wave cases in wintertime..... - 100 -

Figure 40. Model simulated cross-barrier wind speed (shading and contour) along vertical cross sections during the downslope wind case and the mountain wave case..... - 101 -

Figure 41. Model simulated w-component (shading and contour) along vertical cross sections for trapped lee wave cases in wintertime from surface to 18 km. - 102 -

Figure 42. Model simulated w-component (shading and contour) along vertical cross section during downslope wind case and mountain wave case from surface to 18 km. - 103 -

Figure 43. Time series of upstream airflow wavelengths in the unit of km. The location of two vertical cross sections are shown in Figure 16. - 104 -

List of Tables

Table 1. WRF model set up in three trapped lee wave cases in winter time, a downslope wind storm case and a mountain wave case over O‘ahu.	- 61 -
Table 2. Temporal and spatial resolution, initial time and total simulated hours, and input data sources used for WRF model in all simulated events.....	- 63 -
Table 3. Observed wavelengths from satellite images and calculated wavelengths using equation (9), and corresponding horizontal wave number k for TRAP1, TRAP2, and TRAP3 events-	105

-

Chapter 1

Introduction

1.1 Background

In a stably stratified atmosphere, vertical displacement of an air parcel by topography can trigger gravity waves propagating downstream of a mountain ridge. When the mountain range is less than 100 km in width, the Rossby deformation radius $\lambda_R \equiv f_0^{-1} \sqrt{gH}$ (f_0 is the Coriolis parameter, g is the gravitational acceleration, and H is the width of the mountain range) is on the order of 10^3 km. Therefore, the rotational effect of airflow is negligible, and waves develop in the vertical x-z plane (Durran 1986). The basic wave structure is determined by the size and shape of the mountain and by the vertical profiles of temperature, wind speed and moisture of the impinging flow (Durran 2003). For mountain-induced mesoscale waves, they may be conveniently divided into those occurring over the mountain (mountain waves), and those occurring in the lee of the mountain (lee waves) (Atkinson 1981). Lee waves have been observed in both the troposphere and stratosphere (Nicholls 1973), and they can sometimes be detected by cloud formations, such as smooth lenticular clouds or ragged rotor clouds. In other cases, without enough moisture, lee waves may generate regions of clear-air turbulence, which can pose a potential hazard to aviation (Doyle and Durran 2002).

Abundant observations of lee waves or mountain waves have been recorded by satellites (Gjevik and Marthinsen 1978), aircraft (Caccia et al. 1997; Lilly 1978), radars or lidars (Ralph and Neiman 1997; Reeder et al. 1999; Vachon et al. 1994), and constant level balloons in different parts of the world, such as over the Sierra Nevada (Holmboe & Klieforth, 1957), the Rocky Mountains (Klemp and Lilly 1975), the Appalachians (Lindsay 1962), and Pennines of England (Aanensen 1965). From observational studies, it is clear that, given a mountain ridge, the occurrence of lee waves depends primarily on two atmospheric characteristics: static stability and winds. The airflow should have a large wind component perpendicular to the ridge and be maintained through a considerable depth of the atmosphere under a stably stratified atmosphere (Atkinson 1981). It is noted that the maximum amplitude of lee waves is usually in or near the layers of maximum static stability (Starr and Browning 1972).

Observations and numerical simulations indicate evolving mountain waves with time (Nance and Durran 1997). In the third intensive observation period (IOP3) of the Momentum Budget over the Pyrenées (PYREX) around the Pyrenean chain during October and November 1990, lee waves were found to be far from stationary during their lifetime, whereas there were some periods, never longer than 1.5 h, during which the waves were quasi-stationary (Caccia et al. 1997). Changes in the wave environment can be revealed by hourly observed vertical profiles of wind and virtual temperature (Ralph and Neiman 1997). The deepening of the mixed boundary layer thins the elevated stable layer, and thus can cause the temporal increase of the horizontal wavelength (Ralph and Neiman 1997). In this study, changes in the upstream conditions,

such as, the vertical wind profile and inversion layer will be examined to study the temporal variations of lee waves.

1.2 Climatology background and topography

Wind patterns and vertical structure of the atmosphere over the Hawaiian Islands are influenced by the synoptic variations of high pressure patterns. In summer, the subtropical high is well developed. The center of the subtropical high is located around 150 °W, 38 °N, with a maximum surface pressure of 1025 hPa. The pressure ridge lies well north of the islands, with steady northeast trade winds. Statistically, trade winds have a maximum chance of occurrence (93%) during August (Schroeder 1993). The occurrence of trapped lee waves is relatively less.

The island of O‘ahu has two mountain ranges, the Ko‘olau mountain range and the Wai‘anae mountain range, with peaks of 944 and 1,227 m, respectively (Fig. 1), well below the typical trade-wind inversion (TWI) height (~ 2 km). Both of them are oriented in the northwest to southeast direction, therefore northeasterly trade wind flow is nearly perpendicular to the mountain ridges. In summer, the change in the vertical wind profile due to the presence of upper-level low pressure disturbance may favor the development of trapped lee waves downstream of the island of O‘ahu (Sonia et al. 1998).

In winter (Fig. 2), the subtropical high-pressure cell lies farther southeast than its summer location with the center located around 130°W, 32°N, with a mean central

pressure of ~ 1021 hPa. The ridge of the subtropical high (SH) extends westward from the center to just north of the Hawaiian Island chain (Schroeder, 1993). The SH ridge migrates north or south of its mean position. When the ridge is near the island chain, winds are lighter than normal. When the ridge is to the north of the islands, northeast trade winds prevail.

Cold fronts are common between October and April. They are typically associated with mid-latitude cyclones and moisture tongue, which brings clouds and rain. Prior to the arrival of the fronts, winds frequently turn from southeasterly to southwesterly, which has a large component perpendicular to mountain ranges over O‘ahu. However, when cold fronts pass directly over the islands, winds become northwesterly at first, then northerly, and finally shift to northeasterly as the migratory high behind the cold front propagates eastward, crosses the Hawaiian Island chain, and merging with the subtropical high (Burroughs and Larson 1979; Sonia et al. 1998).

1.3 Objectives

With sufficient moisture, trapped lee wave clouds could possibly be observed over the Hawaiian Islands from visible satellite images during the daytime, especially downstream of the Island of O‘ahu. Trapped lee waves have been observed during both the winter and summer months over Hawai‘i, when the prevailing winds have a large wind component perpendicular to the mountain ranges and no critical level between 500 hPa to 300 hPa. Despite plenty of previous lee wave studies, synoptic conditions

conductive to trapped lee wave clouds over O‘ahu have not been fully examined.

Furthermore, most of the previous theoretical studies are based on idealized 2-D flow.

The purpose of this study is to determine the preferential synoptic conditions for the occurrence of trapped lee waves downstream of O‘ahu in summer and winter, the high-resolution model efficiency on local trapped lee wave simulation, and the wave structure as well as evolution with time. High-resolution model simulations is conducted in 3-D, using real island terrain initialized by the global analyses provided by the National Center for Environment Prediction (NCEP). The evolution of trapped lee waves are examined by analyzing the response to changes in upstream conditions. Comparison between trapped lee waves and mountain waves may give some clues concerning the crucial factors which determine the wave types. Lastly, the influence of latent heat release on trapped lee waves over O‘ahu is discussed.

Chapter 2

Overview of Mountain Waves

2.1 Airflow Interactions with Terrain

The interaction between the upstream flow and a 3-D-mountain has been studied theoretically (Rotunno et al. 1999; Schär and Durran 1997; Epifanio and Rotunno 2005; Smolarkiewicz et al. 1988; Schär and Smith 1993; Smolarkiewicz and Rotunno 1989). A common way to examine the airflow past an isolated 3-D mountain is by calculating the Froude number (Fr), which is defined as $Fr = U/NH$, where U is the upstream cross-mountain wind speed, N is the Brunt–Väisälä frequency and H is mountain height. For a given mountain height, U/N can be compared with H . When $U/N > H$, the surface air parcel can move directly over the mountain with a large-amplitude gravity wave over the peak (Smolarkiewicz et al. 1988; Smolarkiewicz and Rotunno 1989). For U/N much smaller than H , the low-level flow is deflected around the flanks of the terrain. These studies have shown that the Froude number ($Fr = U/NH$) is the control parameter for the transition between the “flow over” and the “flow around” state. For the case of O‘ahu, the ridge heights vary from 0.9-1.2 km, therefore, the cross-barrier wind speed should be large enough such that a U/N should be at least greater than 0.9 km (Nguyen et al. 2010).

2.2 Linear Theoretical Framework of Trapped Lee Waves

In order to study the synoptic conditions for the occurrence of trapped lee wave development, it is necessary to start from dynamic theories on mountain-induced gravity waves. The most fundamental properties of orographic waves can be examined by considering the steady-state, two-dimensional airflow over a “small amplitude” mountain using the linear theory (Durran 1986; Scorer 1949; Queney 1948). Queney (1948) gave solutions for a uniform stream with wave motion to the lee of barrier, however, these waves are insignificant and disappear downstream. If the phenomenon is considered on a small enough scale so that the earth’s rotation can be ignored, then these waves are quite negligible (Queney 1948). In those earlier works, wind and stability were considered to be constant with height.

However, Scorer (1949) showed that waves could possibly occur in the lee of the barrier depending mainly on the existence of wind variation with height, and are referred to as the “lee-waves”. For a wave-like corrugation of the ground of wavelength $\frac{2\pi}{k}$, small enough for the earth’s rotation to be neglected, the stream function of the disturbance satisfies the following relationship

$$\frac{d^2\psi}{dz^2} - \left(\frac{g}{c^2} + N^2\right)\frac{d\psi}{dz} + (L^2 - k^2)\psi = 0 \quad (1)$$

where g is the gravity, c is the adiabatic speed of sound, N^2 is the Brunt–Väisälä frequency, U is horizontal wind along the streamline, and k is the horizontal wave number. In order for lee waves to occur, the parameter l must decrease upward, where

$$L^2 = \frac{N^2}{U^2} - \left(\frac{1}{U}\right) \left(\frac{d^2U}{dz^2}\right) \quad (2)$$

From a two layer model, these waves could occur if

$$L_l^2 - L_u^2 > \frac{\pi^2}{4H^2} \quad (3)$$

and

$$L_l^2 > k^2 > L_u^2 \quad (4)$$

where L_l and L_u are the Scorer parameters in the lower and upper layers, respectively; and H is the depth of the lower layer.

Observations suggests that the conditions commonly associated with waves usually have multiple layers (Pilsbury 1955; Mason 1954). Taking surface friction into consideration, a three layer model (Fig. 5) is proposed by C. E. Wallington (1960) from previous observations, comprising of: (1) a layer of low stability (high temperature-lapse rate) at low levels; (2) a stable layer (such as, isothermal layer or inversion) above this lower layer, and (3) an upper layer of low stability in the upper troposphere.

Based on Scorer's idealized two-layer model, Durran (2003) applied the Boussinesq approximation to linearized internal gravity wave equations, and thus obtain a single equation for the vertical velocity w :

$$\frac{\partial^2 w}{\partial z^2} + \frac{\partial^2 w}{\partial x^2} + L^2 w = 0 \quad (5)$$

Neglecting surface friction, and considering the boundary conditions as:

$$h(x) = h_0 \sin(kx) \quad (6)$$

$$w(x, 0) = U \frac{\partial h}{\partial x} \quad (7),$$

where $h(x)$ is the topography along the flow direction, the solution is

$$w(x, z) = \tilde{w}_1(z) \cos kx + \tilde{w}_2(z) \sin kx \quad (8),$$

with the following dispersion relationship:

$$\frac{d^2 \tilde{w}_i}{dz^2} + (L^2 - k^2) \tilde{w}_i = 0 \quad i = 1, 2 \quad (9),$$

and

$$L^2 - k^2 = m^2 \quad (10),$$

where m is the vertical wave number, and k is the horizontal wave number. For a terrain-induced buoyancy oscillations, horizontal wave number is related to mountain shape. A greater mountain width would result in a smaller horizontal wave number k , and vice versa. From equation (2), L^2 is determined by wind speed, static stability and vertical wind shear. With a smaller mean wind speed, larger stability, and greater wind shear, L^2 is expected to be smaller. Whether vertical wavenumber m has a real solution or not depends on the relative magnitudes of the Scorer parameter L and the horizontal wavenumber k . When $L^2 < k^2$, there is no real solution for m and waves decay exponentially with height (Fig. 3a); When $L^2 > k^2$, m^2 is positive and a wave can propagate vertically with wave crests tilting upstream with height, as shown in Figure 3b under the conditions of vertically uniform stability and wind.

Vertical variation of stability and wind speed result in different vertical wave structures. Durran (2003) conducted idealized experiments to analyze how decreasing L^2 with height modifies the buoyancy oscillations. Figure 4a is the airflow with L^2 constant to height, and appropriate N and U are chosen so that $m^2 > 0$. Waves propagate in both horizontal and vertical directions. Wave crests tilt upstream with height. However, a two-layer simulation with decreasing L^2 (Figure 4b) suggests different types of streamlines. In this figure, constant N throughout each of the two layers and a larger U above 3 km results in vertical decrease in L^2 . From the surface to the 3-km level, L^2 is large enough so that $m^2 > 0$ and vertical propagation is possible. Above 3 km, L^2 is smaller than k^2 , and the wave decays exponentially. Therefore, the vertical propagation in the lower layer is trapped by the layer above with smaller L^2 , and the waves bounce between the surface and the trapped layer.

2.3 Nonlinear Mountain Waves

It is reasonable to describe small amplitude trapped lee waves using linear theory, but nonlinear theory is more proper for downslope winds, which are usually accompanied by a hydraulic jump. The atmospheric hydraulic jumps is analogous to bores in rivers and proposed as an explanation of squall lines by Freeman (1948, 1951). Through a turbulent hydraulic jump, the accelerated flow adjusts back from supercritical to the ambient subcritical conditions. In the cases where the nonlinear waves are much larger than their linear counterparts, the highest stability is found in the lower layer and

the flow resembles a hydraulic jump (Durran 1986). Sometimes mountain waves with large-amplitudes on the lee side are observed over the Hawaiian Islands, causing localized downslope wind storms. Generally, two types of synoptic disturbances have the capability of bringing high winds to the Hawaiian Islands: cold fronts and Kona storms (Blumenstock and Price 1967). Before the cold front, heavy rains and strong southerly winds are frequently observed. After the frontal passage, the post-frontal high pressure system merges with the semi-permanent subtropical high with a high pressure center just to the north of the Hawaiian Islands. Therefore, strong and gusty northeasterly trade winds dominate the Hawaiian Island chain. Below the inversion, downslope winds are strong on the lee-side (Zhang et al. 2005; Simpson 1952; Ramage 1962). In this study, the difference in large-scale conditions between the trapped lee waves and downslope winds over O‘ahu will be discussed further.

Several previous studies have described downslope wind storms in different areas and suggests similar elements. From the analysis of 20 Boulder windstorms, Brinkmann (1974) concluded that a stable layer and relatively strong winds above the mountaintop are the favorable large-scale conditions for the development of downslope windstorms. Klemp and Lilly(1975) suggest that the strong downslope winds occur when the atmosphere has a multilayer structure with a superposition of reflected waves, so that the vertical propagating mountain waves are reflected by the variations in vertical static stability. They (Klemp and Lilly 1978) further note that such reflections could occur due to the presence of a critical level where the winds reverse its direction aloft. Even without a critical level in the ambient flow, a growing wave may break and generate a

“self-induced” critical level. Having analyzed a number of historical events, Colman and Dierking (1992) identify three necessary criteria for strong downslope, including 1) strong cross-barrier flow near ridge top, 2) an inversion at or just above ridge top; and 3) cross-barrier flow decreasing with height with a critical level aloft.

Chapter 3

Data and Method

3.1 Synoptic Data

In this study, satellite observations, synoptic charts, and skew-T plots are used for synoptic analysis. To identify lee wave clouds, we used several 1 km-resolution visible (VIS) images from Geostationary Operational Environmental Satellites (GOES), which was provided by the Comprehensive Large Array-Data Stewardship System (CLASS) from National Oceanic and Atmospheric Administration (NOAA). For the summertime trapped lee wave case on 25 August, 1977, satellite images from the Synchronous Meteorological Satellite (SMS)-2 1 km VIS channel are used.

Based on the evolution of trapped lee wave clouds observed by satellite, wave cases are divided into several stages. Synoptic conditions during each stage are examined. NCEP Climate Forecast System Reanalysis (CFSR) (Saha and Coauthors 2010) or NCEP Climate Forecast System Version 2 (CFSv2) (Saha and Coauthors 2011) 6-hourly products at $0.5^{\circ} \times 0.5^{\circ}$ spatial resolution are used to depict the synoptic pressure and wind patterns. Other sources used for synoptic background analysis include surface maps from the Ocean Prediction Center of National Weather Service. The Lihue soundings from the University of Wyoming are used to delineate the wind profiles and vertical atmosphere stratification.

3.2 Model Description

For the Hawaiian Island chain, previous studies have simulated island circulations under different trade wind regimes and their response to various initial conditions (Zhang et al. 2005; Yang et al. 2005; Yang and Chen 2008; Nguyen et al. 2010; Carlis et al. 2010). Among those simulations, the first 12-h of model runs are considered to be the model spin-up period. After spin-up, the orographic influences on the airflow are represented well in the high-resolution nested domains.

The Weather Research Forecasting (WRF) Model version 3.5 is used to simulate the trapped lee waves and mountain waves in three dimensions. The following events over O'ahu are simulated: three trapped lee wave cases in winter time (24 January, 2003; 27 January, 2010; 26 January, 2014); a downslope wind storm case on 14-15 February, 2001; and a mountain wave case on 1 August, 2013. We used the Betts-Miller-Janjic cumulus parameterization (Janjić 2000, 1994), the Yonsei University (YSU) planetary boundary layer (PBL) scheme (Hong et al. 2006), new Eta (Ferrier, 2001) microphysics options (Roger et al. 2001), and Rapid Radiative Transfer Model (RRTM) for General Circulation Model (GCM) as radiation scheme (Iacono et al. 2008). The RRTM for GCMs (RRTMG) improves inefficiencies with minimal loss of accuracy for GCM applications. Details are provided in Table 1. Land-surface model is Noah with vegetation cover and soil properties compiled by Zhang et al. (2005). Soil moisture and soil temperature input are spun up for two months prior to the simulation period (Yang et al. 2005) with the updated soil moisture and soil temperature.

The CFSR 6-hourly data with a horizontal grid of $0.5^{\circ} \times 0.5^{\circ}$ is used to initialize the model. The modeling strategy is consistent with three nesting domains with horizontal grid spaces of 9 km, 3 km, and 1 km, respectively (Fig. 5). The 1 km domain covers the entire island of O‘ahu. There are 38 vertical levels¹ from the surface to the 100-hPa level. Specific initial time and running hours are documented in Table 2. The spin-up time for each case is 12 hours.

¹ The full sigma levels are 1.000, 0.994, 0.983, 0.968, 0.950, 0.930, 0.908, 0.882, 0.853, 0.821, 0.788, 0.752, 0.715, 0.677, 0.637, 0.597, 0.557, 0.517, 0.477, 0.438, 0.401, 0.365, 0.332, 0.302, 0.274, 0.248, 0.224, 0.201, 0.179, 0.158, 0.138, 0.118, 0.098, 0.078, 0.058, 0.038, 0.018, 0.000

Chapter 4

Synoptic Analysis of Trapped Lee Wave Event in Winter

In this study, three wintertime trapped lee wave cases are analyzed. They are the trapped lee waves of 26-27 January, 2010 (TRAP1), 24-25 January, 2003 (TRAP2), and 26 January, 2014 (TRAP3).

4.1 TRAP1---26-27 January, 2010

On 27 January, 2010, a typical wintertime trapped lee wave event occurred downstream of the island of O‘ahu. On 1800 UTC, 26 January 2010, trapped lee wave clouds were observed to the northeast of the Ko‘olau mountain range (Fig. 7a), and became more organized after 0000 UTC, 27 January 2010 (Fig. 7b). With southwesterly airflow perpendicular to the mountain, lee waves were propagating to the northeast. Maximum wavelengths were around 12 km at 0300 UTC, 27 January 2010 (Fig. 7c). Based on the wave evolution captured by the satellite VIS images, this trapped lee wave case can be divided into (1) developing (1800 UTC, 26 -- 2300 UTC, 26 January); (2) mature (0000 UTC --- 0400 UTC, 27 January); and (3) decaying (0500 UTC --- 1200 UTC, 27 January) phases. As will be shown later, the evolution of this wave event is highly related to the variations in synoptic conditions including the inversion height.

Before this trapped lee wave event, with a relatively southward shift of the subtropical high, the inversion was below the 1.5-km level (Fig. 9a). With the ridge axis to the south of the island of O‘ahu (Fig. 8a), low level winds over O‘ahu were weak and

southerly (Fig. 9a). A mid-latitude cyclone was presented to the northwest of the Hawaiian Islands, with a cold front extending in the NE-SW direction. As the cold front moved toward the island of O‘ahu from 1800 UTC, 26 January to 0000 UTC, 27 January 2010 (Figs. 8a, b), the subtropical high retreated towards the east. Concurrently, the wind direction shifted from southerly to southwesterly (Fig. 9b) and the inversion was lifted by the approaching cold front from 1.5 km to 2 km (Fig. 9b). During this period, well developed trapped lee wave clouds were observed (Fig. 7c). After the cold front passed the island of O‘ahu around 0600 UTC, 27 January (Fig. 8c), low level winds turned to northwesterlies, paralleled to the mountain ridge. In the meantime, the inversion was lifted to the 3-km level (Fig. 9c). Then, the trapped lee waves decayed quickly and the lenticular clouds dissipated.

4.2 TRAP2---24-25 January, 2003

On 2000 UTC, 24 January 2003, another wintertime trapped lee wave case was observed by GOES-10 VIS satellite images (Fig. 10). This trapped lee wave event could be classified into several stages based on the satellite observations: (1) developing (1800 UTC -- 2100 UTC, 24 January 2003); (2) mature (2100 UTC -- 2300 UTC, 24 January 2003); and (3) decay (2300 UTC -- 0500 UTC, 25 January 2003). At 1800 UTC, 24 January 2003 (Fig. 10b), the trapped lee wave clouds became visible to the northeast of the island of O‘ahu. At 2200 UTC, 24 January 2003, well-shaped sequential lenticular clouds had propagated more than 200 km downstream under the southwesterly winds.

The synoptic conditions favorable for the trapped lee wave clouds included the approaching cold front and the retreating subtropical high. Before this event, no trapped lee wave clouds were observed except some orographic clouds over the mountains (Fig. 10a). The horizontal distribution of geopotential height at 0000 UTC, 24 January, 2003 (Fig. 11a) shows that the subtropical high was to the east of the Hawaiian Islands with the ridge axis to the south. With a mid-latitude cyclone located to the north of the Hawaiian Islands, the low-level winds over O‘ahu were southwesterly flow. From 0000 UTC (Fig. 11a) to 1800 UTC (Fig. 11b) at 24 January, 2003, O‘ahu was in the prefrontal region, whereas the cyclone and the cold front were moving eastward towards O‘ahu. Meanwhile, the ridge axis of the subtropical high extended westward with an increased central pressure from 1020 hPa to 1025 hPa. As a result, the pressure gradient between high and low pressure systems increased, and the pre-frontal southwesterly flow strengthened (Fig. 11b).

In addition to low-level winds, the vertical wind profile and the inversion height were also influenced by the approaching cold front. At 1200 UTC, 23 January 2003 (Fig. 12a), the atmosphere was highly stratified with a dry and stable layer around 1.5 km. As the cold front moved closer, the inversion height was lifted to 2 km at 1200 UTC, 24 January 2003 (Fig. 12b). However, the cold front passed over the island of O‘ahu at 1200 UTC, 25 January 2003 (Fig. 11c), and the inversion no longer existed (Fig. 12c), thereby ending this trapped lee wave event immediately.

4.3 TRAP3---26 January, 2014

Another recent wintertime trapped lee wave event was observed on 26 January, 2014 (TRAP3). Compared with the previous two cases, TRAP3 has shorter time period for each stage. The development and mature stages of TRAP1 and TRAP2 all lasted more than 7 hours, whereas the entire duration of TRAP3 was around 4-5 hours. The changes in the synoptic pattern during this case are shown in Figure 13. At 1200 UTC, 26 January 2014, a mid-latitude cyclone was located around 42°N, 145°W with a central pressure of 972 hPa. A cold front extended from the center of low pressure to the southwest. The island of O‘ahu, as noted by the red dot in Figure 13a, was just to the east of the cold front. The subtropical high was separated into two high pressure centers by the cold front. Accompanied with the eastward propagation of the cold front, the high pressure center east of the cold front retreated eastward. With the ridge axis south of the Hawaiian Island chain, low-level winds over O‘ahu were southwesterlies. At 1800 UTC, O‘ahu was still in the prefrontal regime, and the cold front continued to move toward the Hawaiian Islands (Fig. 13b). A series of lenticular clouds were observed downstream of O‘ahu from the GOES-west visible images (Fig. 14a). In the following two hours (Figs. 14b, c), trapped lee waves developed and propagated to the northeast of O‘ahu. After 2200 UTC, 26 January 2014, cold front passed the island of O‘ahu, as shown from the satellite VIS image at the same time (Fig. 14 d) and the synoptic chart at 0000 UTC, 27 January 2014 (Fig. 13 c).

Before the TRAP3 event, the inversion base from the Lihue sounding was located at the 1-km height level, and at 1200 UTC, 26 January 2014, low level winds are weak westerlies (Fig. 15a). At 0000 UTC, 27 January 2014 (Fig. 15b), the inversion base was lifted to the height of 3.5 km. The low-level post-frontal winds turned northwesterly and weakened. No more trapped lee waves were observed from satellite images.

To summarize, during the development of trapped mountain lee waves in winter, common synoptic settings include an approaching cold front to the west and a retreating subtropical high to the east of O‘ahu. Prefrontal winds turned to southwesterly and strengthened because of the increase in pressure gradients. Meanwhile, westerly flow prevails in the upper level without a critical level in the wind profile. The inversion was lifted slightly but still existed, which is the one of the prerequisites for the development of trapped lee waves.

Chapter 5

Model Simulation of Trapped Lee Wave in Winter

Initialized by the global data and nested in regional domain, a 1 km-grid island-scale WRF model over O‘ahu is employed (Fig 6). The vertical sections perpendicular to the mountain ridges at different stages will be constructed from model results to study the evolution of three wintertime events (TRAP1, TRAP2 and TRAP3) under changing synoptic conditions. The vertical transection lines in each case are almost parallel to the horizontal winds and crossing the Wai‘anae and Ko‘olau Mountains (Fig. 16). The dots in Figure 16 are the locations used to construct time series of vertical profiles of atmospheric properties in the upstream environment.

5.1 TRAP1---26-27 January, 2010

5.1.1 Wave Structure

Figure 17 shows the evolution of the vertical motion at the 850-hPa level at different stages of the trapped lee wave development for the 26-27 January 2010 case. As evident from the Lihue sounding during the developing stage, the base of the dry stable layer for this case was at the 2.5-km height level with the moisture confined underneath (Fig. 9b). The 850-hPa level is used to depict the vertical motion of trapped lee waves within the marine boundary layer and is in good agreement with satellite observations (Fig. 7).

Before the event, airflows on the leeward side of the Ko‘olau Mountains are dominated by the descending airflow (Fig. 17a). In the developing stage (Fig. 17b), waves are simulated between the Wai‘anae and Ko‘olau Mountains and propagate to the northeast of O‘ahu. The oscillations in the vertical motion could be divided into two branches: one to the north which is the resonance of waves triggered by the Wai‘anae and Ko‘olau Mountains; the other to the south, is mainly caused by the Ko‘olau Mountains solely. The two branches of vertical motion simulated by the model are consistent with the satellite observations of lenticular clouds (Figs. 17b, c; Fig. 7b). In the mature stage, the simulated trapped lee wave clouds are more organized, and propagate farther downstream (Fig. 17c). The maximum vertical motion w reaches 1.5 m s^{-1} . The simulated wavelength is around 12 km in agreement with the satellite images. During the decaying stage (Fig. 17d), as the favorable wind and stability conditions no longer exist, the simulated lee waves disappear without vertical motion oscillations off the leeward coast of O‘ahu. In all, the evolution of simulated vertical oscillations coincides well with cloud formation in the satellite images during the trapped lee wave event of 26-27, January 2010.

The relative humidity distribution in the vertical cross section suggests the change of water vapor and the possibility of cloud formation during this trapped lee wave event. Figure 18 shows moisture distribution (shading) and isentropic line (contour) along the cross section. Before the trapped lee wave development (Fig. 18a), moisture is confined by an inversion at a typical height around 1.5 km, and leeward side oscillations exist in the dry stable layer above the 2-km level. In the developing stage (Fig. 18b), the

low-level oscillations below the inversion are more significant, but cloud formation is only possible over the upslope region of Wai‘anae with relative humidity greater than 90%, as shown by the white dashed lines; in the mature stage (Fig. 18c), the gravity waves between the surface and the inversion are well developed. Based on the moisture distribution, the 308-K potential temperature contour line is approximately at the base of the inversion. From the developing (Fig. 18b) to mature stage (Fig. 18c), the inversion base is lifted from 1.5 km to 2.5 km with increasing moisture amount underneath (Fig. 9). Wave amplitude is the greatest around the 308 K potential temperature contour line, corresponding to the inversion base. In the decaying phase, southwesterly wind component weakens and the buoyancy oscillations die out without trapped lee wave clouds, despite the availability of sufficient moisture (Fig.18d).

5.1.2 Time Series of the Upstream Flow

The temporal changes of synoptic conditions result in evolving upstream conditions and different interactions between airflows and mountain ridges. In Figure 19, time series of upstream flow are presented, including the evolution of wind, wavelengths λ , U/N and the square of the Scorer parameter L^2 . In Fig. 19 the panels on the left hand side are upstream flow at Dot 1 and the panels on the right are the ones at Dot 2. In general, the upstream conditions at Dot 1 and Dot 2 were similar except the slight difference due to location, since the cold front in wintertime usually passes the island of O‘ahu from the northwest to the southeast.

Figures 19a and 19b show the presence of wind shear and enhanced wind speed during the trapped lee wave development. As the strong pre-frontal southwesterly flow approaches, the upstream flow between 1 km and 2 km increases from 8 m s⁻¹ to over 10 m s⁻¹. From 2200 UTC to 0400 UTC, wind increase with height through the inversion (~ 1.5- 2.5 km). However, after 0600 UTC, 27 January 2010, the low-level cross-barrier flow decreases significantly and shifts to a westerly direction, ending the trapped lee wave event.

As indicated by the relationship that $\lambda v = c$ (λ is wavelength, v is the frequency, and c is wave speed), if upstream airflow strengthened, the wavelength will increase correspondently. A simple way to estimate the wavelength is:

$$\lambda = \frac{2\pi U}{N} = \frac{2\pi U}{\left[\frac{g(\Gamma-\gamma)}{T}\right]^{\frac{1}{2}}} \quad (9)$$

where T is the temperature with unit of K, Γ is the dry adiabatic lapse rate of approximately 9.8 °C km⁻¹, γ is the environmental lapse rate, and U is the cross-barrier wind speed. A lower stability and stronger winds favor longer wavelengths (Atkinson, 1981). In this equation, N is calculated in unsaturated air, which is the ‘dry’ condition without latent heat release. The wavelength differences with or without latent heat will be discussed in Chapter 8.

Figures 19c and 19d are the calculated wavelengths based on equation (9), both of which indicate elongated wavelengths related to increasing cross-barrier wind speed. With increasing southwesterly wind after 1800 UTC, 26 January 2010 (Fig. 19a), the

wavelengths at the 1.5-km level increases to over 6 km. After the passage of a cold front at 0600 UTC, 27 January 2010, winds decelerate and turn to westerlies. The wavelengths decrease simultaneously. Vertical variation of wavelengths suggests the influence of stability. During the trapped lee wave development, oscillations are simulated in the layer from 1.5 to 2.0 km layer, which is the inversion, with shorter wavelength than those in the lower layer or upper layer. In Figure 19e, U/N increases from 0.7 to 1.0 km during the trapped lee wave development, satisfying the requirement of $U/N > H$.

Figures 19g and 19h show the time series of vertical Scorer parameter square (L^2) profile for this case. From 0000 UTC to 0600 UTC, 27 January 2010, the bottom layer between 0.5-km and 1.5-km has L^2 smaller than 1 km^{-2} . The middle layer between 1.5-km and 2.5-km has L^2 larger than 1.4 km^{-2} . However, L^2 decreases to less than 0.8 km^{-2} at the upper level above the 3-km. The difference between the square of the Scorer parameter in lower layer L_l^2 and upper layer L_u^2 is 0.6 km^{-2} . If one select 2.5 km as the height of lower layer in equation (7), $\frac{\pi^2}{4H^2}$ is around 0.39 km^{-2} . It can be concluded that the decrease of the Scorer parameter in the vertical direction is large enough for the trapped lee wave development.

5.2 TRAP2---24-25 January, 2003

5.2.1 Wave Structure

Without enough moisture, a gravity wave may still exist with significant vertical oscillations in the lee side, but no cloud can be observed. During the early stage of wave evolution of TRAP2, satellite images at 0300 UTC, 24 January 2003 show clear skies with limited clouds over the mountains and the leeward side (Figs. 10a, b), whereas the model results suggest that oscillations in vertical motion are already present (Fig. 20a). This may be related to insufficient moisture during the early stage.

After 0300 UTC, 24 January 2003, the vertical motion at the 850-hPa level (Fig. 20a) and the potential temperature contours (Fig. 18a) all suggest significant leeward oscillations, propagating to the northeast of O‘ahu. The distribution of relative humidity in the vertical cross section (Fig. 21a) indicates an extremely dry layer between 1.5-km and 3.5-km, which is the inversion layer as shown in the Lihue sounding at 1200 UTC (Fig. 12b). Therefore, in addition to the clouds in the upslope regions and over the mountain tops, due to orographic lifting, only one cloudy area is in the leeward side as shown by the GOES VIS images (Fig. 10a). In the early stage (Figs. 20a, 21a), trapped lee waves are present but without lee wave clouds. From 0300 UTC to 1800 UTC, 24 January 2003, the cold front moved closer toward the island of O‘ahu from the northwest. The strengthened prefrontal winds elongate the wavelengths and amplify the vertical motions (Figs 20a, b). The wavelength from ~12 km to ~18 km and the wave amplitude in the leeward side is more significant with the maximum vertical motion

increasing from 1 m s^{-1} to greater than 1.5 m s^{-1} . The inversion is lifted (Fig. 12b). Lee side clouds are evident both in the satellite images (Fig. 10b) as well as in low level of model simulation (Fig. 21b) with relative humidity greater than 90%. In the mature stage, the cross-barrier wind speed is stronger than earlier. The simulated vertical motions at the 850-hPa level (Fig. 20c) and the potential temperature contours (Fig. 21c) all indicate the presence of trapped lee waves. At 0300 UTC, 25 January 2003, the cold front has passed O‘ahu, so the simulated oscillations on the leeward side dissipate (Fig. 21d). Despite abundant water vapor, buoyancy oscillations no longer exist.

5.2.2 Time Series of Upstream Flow

For the TRAP2 case on 25 January, 2003, low-level winds are light southwesterlies ($\sim 6\text{-}8 \text{ m s}^{-1}$) before the cold front approached. After 0600 UTC, 24 January 2003, the upstream airflow at the stable layer (1.5 km) increases from 12 m s^{-1} to more than 20 m s^{-1} (Fig. 22a). The horizontal wind speed from the surface to the inversion base increase with respect to height through the inversion. Wind directions are almost perpendicular to the mountain ridges. After the passage of the cold front at 0300 UTC, 25 January 2003, winds turn to westerlies and weaken, and trapped lee waves dissipate. From 0000 UTC to 1800 UTC, 24 January 2003, the simulated wavelength increases from 6 km to 10 km as the upstream flow strengthens (Figs. 22c, d). At 0000 UTC, 25 January 2003, the maximum simulated wavelengths ($> 10 \text{ km}$) occurs at the height from 1-km to

1.5-km. The layer between 2 km to 2.5 km has wavelengths shorter than 6 km due to relatively strong stability.

The maximum upstream wind speed during TRAP2 is almost twice as that during TRAP1 (Figs. 19a and b, 22a and b). The calculated U/N is over 1.5 km during the trapped lee wave development, which is much higher than the mountain height of 0.6-0.9 km. With Froude number (Fr) greater than 1, airflow can move over the mountain ridges. The vertical profiles of the Scorer parameter (Figs. 22g, h) indicates that the most favorable period for trapped lee wave development is between 0600 UTC to 1800 UTC, corresponding to the simulated vertical motion evolution in Figure 20. The square of the Scorer parameter L^2 decreases from 1.2 km^{-2} to 0.4 km^{-2} from the 2-km level to the 3-km level (Figs. 22g, h). If 2-km is taken as the interface between upper and lower layer in Scorer's two-layer mountain wave theory, $\frac{\pi^2}{4H^2}$ is around 0.62 km^{-2} . The difference between L_l^2 and L_u^2 is 0.8 km^{-2} , so the decrease of L^2 with respect to height is large enough for the trapped lee wave development according to equation (7).

5.3 TRAP3---26 January, 2014

5.3.1 Wave Structure

The trapped lee wave case on 26 January, 2014 (TRAP3) has a shorter duration comparing with TRAP1 and TRAP2 as observed by satellite images (Fig. 14) and the

simulated vertical motion at the 850-hPa level (Fig. 23). The entire TRAP3 event lasts for 5 hours. Before the event, descending motion is simulated over the leeward side of the mountain ridges (Fig. 23). Moisture is limited over the upslope regions and the mountain tops (Fig. 24a). At 1800 UTC, trapped lee wave clouds were observed from satellite VIS images (Fig. 14a). At this time, sequential oscillations are developing to the east of the Ko‘olau Mountains in the model simulation (Fig. 23b), reaching its maximum intensity at 2000 UTC with vertical motion greater than 1.5 m s^{-1} . The pre-frontal airflow is relatively moist (Fig. 24b), and sequential lenticular clouds are likely to occur as indicated by the 90%-relative-humidity contours. At 2000 UTC, the cold front arrived at the northwest tip of the island of O‘ahu (Fig. 14c) with simulated rising vertical motions in the frontal zone (Fig. 23c). From 1200 UTC to 2000 UTC, 26 January 2014, the inversion height is lifted from the 2.5-km level to the 3.5-km level (Figs. 24a, c). At the inversion base, the simulated trapped lee waves have the greatest amplitude as evident from the isentropic contours (Figs. 24b and 24c). At 2200 UTC, no trapped lee waves are simulated in the model (Fig. 23d) in agreement with observations (Fig. 14d).

5.3.2 Time Series of Upstream Flow

Since the cold front moves faster during TRAP3 than the other two cases, this trapped lee wave event only lasts from 1800 UTC to 2100 UTC, 26 January 2014. The upstream southwesterly flow between the 1.5-km and 2.5-km levels increases from 5 m s^{-1} to 8 m s^{-1} during the development of this event (Figs. 25a, b). Between 2100 UTC

and 2200 UTC, the cold front is passing over the island of O‘ahu. After 2200 UTC, postfrontal winds shift to northerlies and weaken to 1 m s^{-1} (Figs. 25a, b). The maximum prefrontal wind speed aloft the mountaintop in TRAP3 ($\sim 8 \text{ m s}^{-1}$) is smaller, compared with that in TRAP1 ($\sim 12 \text{ m s}^{-1}$) and TRAP2 ($\sim 20 \text{ m s}^{-1}$). The calculated horizontal wavelengths from equation (9) is $\sim 4 \text{ km}$ (Figs. 25c, d), shorter than that in TRAP1 and TRAP2 (Table 3) because of the weaker upstream flow.

The calculated U/N (Figs. 25e, f) between 1800 UTC and 2100 UTC is greater than 0.6 km , indicating the ability of the upstream flow to move over the mountains. From 1800 UTC to 2100 UTC, 25 January 2014, the square of the Scorer parameter decreases from greater than 2.2 km^{-2} at the 2.5-km level to less than 1.4 km^{-2} at the 3.5-km level. Accounting for 2.5 km as the height of inversion level, $\frac{\pi^2}{4H^2}$ is around 0.39 km^{-2} , and the difference between L_l^2 and L_u^2 is 0.8 km^{-2} , so trapped lee waves could exist between 1800 UTC and 2100 UTC, 26 January 2014.

5.4 Summary for model simulated wave structure and upstream flow

The 3-D wave structures of TRAP1, TRAP2, and TRAP3 are simulated well in the high-resolution (1 km) WRF model. Trapped lee wave clouds can be observed during the daytime only if sufficient moisture is present. Under relatively dry conditions, trapped lee waves may still exist as clear air turbulence. The vertical distributions of relative humidity and the potential temperature suggest that the inversion is always

lifted before a trapped lee wave event. The vertical stratification of environmental flow matches the three-layer model presented by C. E. Wallington (1960).

Analysis of wave structures and upstream airflow in this chapter indicates that the crucial features necessary for the trapped lee wave development in wintertime are: (1) The presence of an inversion, which is the level with the greatest amplitude and shortest wavelength of trapped mountain lee waves, with the longest wavelength below the inversion base; (2) a stronger pre-frontal cross-barrier wind component related to the approaching cold front with a Fr greater than 1; (3) decreasing Scorer parameter related to the wind shear and stability through inversion should larger than $\frac{\pi^2}{4H^2}$.

5.5 Trapped lee waves over the Hawaiian Islands

For the TRAP1, TRAP2 and TRAP3 events, the Hawaiian Island chain was under similar synoptic background conditions. Trapped lee wave clouds were not observed for all of the Hawaiian Islands for these periods. The formation of trapped lee wave clouds requires sufficient wind speed so that the air flow can move over the mountains, and the air parcel is lifted enough for the water vapor to condense.

The highest mountain heights over the Big Island are more than 4 km, which is well above the inversion layer. Therefore, the low-level airflow is deflected around the island instead of moving over the mountain peaks. Trapped lee waves hardly occur in the lower troposphere over the Big Island. However, it is possible in the upper troposphere since the tropopause could act as an inversion and trap the lee waves beneath, which is

the case on November 25, 2003 (Figs. 26a, b). For that case, lenticular clouds were observed over the Big Island and the highest cloud top reached 12 km.

The highest mountain peaks on Maui, Haleakalā, is more than 3 km, but the highest elevation of the west Maui mountain range is around 1.7 km. The mountain height on Kaua‘i is about 1.6 km, and elevation over Moloka‘i has the highest peaks around 1.5 km. When wind is strong enough with a Froude number greater than 1, trapped lee waves are possible to occur on the leeward side of western Maui, Kaua‘i or Moloka‘i. The mountains over Moloka‘i are long ridges oriented in the E-W direction, whereas terrain over Kaua‘i is single round shape peak. The trapped lenticular clouds would be easier to be observed over Moloka‘i as compared with Kaua‘i.

During TRAP2, trapped lee waves were also observed on the leeward side of western Maui, Moloka‘i and Kaua‘i (Figs. 26e, f). Firstly, the wind speed was as strong as 20 m s^{-1} in the mature stage (Figs. 22a, b), and the calculated U/N of upstream flow was greater than 1.5 km (Figs. 22e, f). Therefore, Fr of the upstream flow toward Kaua‘i and western Maui was greater than 1 and the low-level air flow could move over the mountains. Secondly, the calculated lifted condensation level (LCL) was around 0.5 km, lower than the mountaintops over Kaua‘i and western Maui. As the air parcel was lifted, water vapor could condense to form clouds.

During TRAP1, no trapped lee waves were observed on the leeward side of the western Maui (Fig. 26d). The maximum wind speed was less than 12 m s^{-1} (Figs. 19a, b), and the calculated U/N was smaller than 1.2 km (Figs. 19e, f). Thus the Froude

number for western Maui was less than 1 and airflow was deflected around the mountains. For a lower terrain over Moloka'i (1.1 km) and mountain ridges at northeast Kaua'i (0.4 km), Fr was greater than 1 and lenticular clouds were evident on the leeward side (Figs. 26c, d).

For the trapped lee wave clouds to occur, the mountain height should be right between U/N and lifted condensed level (LCL). The elevation of O'ahu is low enough such that the Fr of the pre-frontal southwesterlies is greater than 1, but high enough to lift the air to reach saturation. Thus, trapped lee waves are more likely to occur in the pre-frontal southwesterly flow for O'ahu as compared to the other islands.

Chapter 6

A Trapped Lee Wave Event in Summer

6.1 Synoptic Conditions for A Trapped Lee Wave Event

Trapped lee wave clouds over O‘ahu are less frequent in summer than in winter. A rare case on 25 August, 1977 was reported by Burroughs and Larson (1979). The SMS-2 1 km visible images (Fig. 27) depict the development of wave clouds downstream of the Ko‘olau Mountains under prevailing northerly to northeast winds. At 1845 UTC, the first wave cloud formed over central O‘ahu. Three hours later, lenticular clouds extended 165 km downstream with a wavelength around 9 km (Fig. 27b).

Figure 28 shows the geopotential height and wind patterns before and during the trapped lee wave development at the 1000-hPa, 700-hPa and 300-hPa levels. Before the trapped lee wave development, at 0000 UTC, 25 August 1977, the subtropical high was to the north of the Hawaiian Islands (Figs. 28 c, e) with prevailing easterly or northeasterly winds at low levels (Fig. 28e). At the 300-hPa level (Fig. 28a), the normal westerly winds aloft were disrupted by upper-level disturbances. An omega blocking pattern (Lupo and Smith 1995) was present over O‘ahu with the high pressure center around 25°N, 160°W, two low pressure centers around 25°N, 175°W and 21°N, 159°W, respectively. Over the next 24 hours (0000 UTC, 25 August --- 0000 UTC, 26 August, 1977), at the 300-hPa level (Figs. 28a, b), the omega blocking pattern strengthened and moved westward/northwestward. Correspondently, upper level winds over O‘ahu rotated from southerlies to northeasterlies. At the 700-hPa level (Figs. 28c, d), an

inverted trough was approaching O‘ahu from the east. The pressure gradients between the subtropical high and the inverted trough increased with the strengthening of the northeasterly winds over O‘ahu. At the 1000-hPa level (Figs. 28e, f), the subtropical high was stronger than earlier with the center located farther north.

The ENE winds near the crest of the mountain range increased from 12 m s^{-1} at 1845 UTC to 18 m s^{-1} at 2145 UTC (Burroughs and Larson 1979). Cross-barrier wind speed was sufficiently large so that Fr was greater than 1. The trade wind inversion base was lifted from 1.5 km at 1200 UTC, 25 August (Fig. 29a) to above the 2-km level at 0000 UTC, 26 August (Fig. 29b). An unusually deep layer of easterly wind component up to the 250-hPa level was evident based on the Lihue sounding at 0000 UTC, 26 August, 1979. In the lower troposphere, the wind speed of the east-northeast trade winds increased significantly with respect to height with a maximum above the trade-wind inversion.

6.2 A Comparison of Trapped Lee Waves in Winter and Summer

The prerequisites for trapped lee wave development in summertime are similar to that in wintertime: a strong cross-barrier wind component, increasing wind speed through the inversion and a stable layer. The vertical wind profile is also a crucial factor for their development in both winter and summer. In wintertime, favorable winds are southwesterly to westerly from the surface to the upper level for trapped lee wave development. In summer, climatologically, low level winds are northeasterly trade

winds while westerlies prevail aloft. Only if an omega blocking shifts the westerly wind to easterlies between 500 hPa and 300 hPa with increasing wind speed aloft, can trapped lee waves development become possible.

Chapter 7

Comparison between Trapped Lee Waves and Other Type of Mountain Waves

7.1 Downslope Wind Storm: 14-15 February, 2001

During 14-15 of February 2001, a wintertime downslope wind case occurred over O‘ahu. At 0000 UTC, 14 February 2001 (Fig. 30a), a cold front was to the northwest of the Hawaiian Islands with enhanced surface northeasterlies, followed by a high pressure cell in the post-front region. Twenty-four hours later (Fig. 30b), the cold front had already passed the island of O‘ahu. The post-frontal high pressure merged with the semi-permanent subtropical high and strengthened. The low-level winds across the Hawaiian Island therefore increased.

Figure 31 shows the observation and model simulated 10-m winds from Zhang and Chen (2005). The 10-m wind speed at Kahuku (Fig. 31a), which is at the northeast point of O‘ahu, increased from $\sim 6 \text{ m s}^{-1}$ at 0500 HST (1500 UTC, 14 February) to a maximum around 14 m s^{-1} at 1500 HST (0100 UTC, 15 February). Observations at Bellows (Fig. 31b), which is on the southeastern coast of O‘ahu, also show a gradual increase in wind speed from a minimum of 8 m s^{-1} at 0500 HST (1500 UTC, 14 February) to a maximum of 16 m s^{-1} at 1000 HST (2000 UTC, 14 February). The low-level prevailing flow was easterly/northeasterly (Figs. 31b, d).

Aside from strong winds, the existence of an inversion is critical. Smith (1985) (1985) and Durran (1986) have shown that the development of strong downslope winds is prevented without an inversion above the crest. The Lihue sounding (Fig. 32) at 0000 UTC, 15 February 2001 indicated an inversion with its base at the 2.5-km level. The top of the inversion layer was lifted on the windward side and reached the highest level before reaching the crest (Zhang et al. 2005). A critical level was present around the 400-hPa level, with northeasterly winds below and westerly winds above. Low-level winds decreased with respect to height until the critical level. The model simulated vertical motions at the 850-hPa level (Fig. 33a), suggesting the downslope winds below the inversion in the leeward side. Moisture is limited at the upslope region and over the mountaintops (Fig. 33b).

In summary, for this case, a critical level below the 400-hPa level, strong cross-barrier flow with a wind speed decreasing with respect to height, and an inversion are the main large-scale factors for the development of downslope wind storms (Zhang et al. 2005).

7.2 Mountain Waves: 31 July, 2013

A mountain wave event occurred on 31 July, 2013. It had a strong cross-barrier wind component with the wind speed increasing with respect to height, and a stable layer above the ridge tops. However, because of the wind profile, a mountain wave instead of a trapped lee wave occurred. Water vapor was confined above the terrain as shown by

water vapor images from the MODIS satellite (Fig. 34), rather than propagating further away to the southwest under the prevailing northeasterly upstream flow.

This case is associated with a remnant low associated with tropical cyclone Flossie. By 1200 UTC on 25 July, 2013, Flossie intensified into a tropical storm, and attained peak winds of 31 m s^{-1} on 27 July. After entering the central Pacific Ocean, it weakened to a remnant low at 1200 UTC, 30 July 2013, but kept moving west-northwest at about 6.7 m s^{-1} . At 1800 UTC (Fig. 35), the remnant trough was to the west of the island of O‘ahu. During the same time, the subtropical high intensified and the ridge axis extended to the north of the Hawaiian Islands. With large horizontal pressure gradients (Fig. 36), the low-level northeasterly flow strengthened. The inversion was lifted as seen in the sounding at 0000 UTC, 15 February (Fig. 37). The mid-level air was more humid than on a typical trade wind day. Since the disturbance occurred in the lower layer, upper level winds were still westerly above the 300-hPa level, whereas low-level winds were northeasterly to easterly from the surface to the 500-hPa level, and a critical level existed at the 500-hPa level. The model simulated maximum leeward side vertical motion (Fig. 38a) is greater than 2.5 m s^{-1} , but there is no further propagation after the airflow goes over the mountain and descends in the leeward side. Moisture is limited in the upslope regions (Fig. 38b).

7.3 Common and Different Factors for Trapped Lee Waves and Other Wave Types

As concluded above, with an inversion layer above the mountaintop as a prerequisite, the stronger pre-frontal winds are favorable for trapped lee wave development in wintertime cases TRAP1, TRAP2 and TRAP3. The inversion layer and stronger cross-barrier flow also existed in the downslope wind storm event of 14-15 February, 2001 and the mountain wave case of 30 July, 2013. Therefore, it is evident that a significant cross-barrier wind component and an inversion are required for the development of trapped lee waves as well as downslope wind storms.

The differences are vertical wind profiles and the existence of critical level between trapped lee wave events and severe downslope storms. All trapped lee wave cases have increasing wind speed from the surface to mid-levels (Fig. 39) and a uniform wind direction from the surface to the 300-hPa level (Figs. 9, 12, 15, 22, and 29). However, for the case of downslope wind (14-15 February, 2001) or the mountain wave (30 July, 2013), a critical level exists around the 500-hPa level (Figs. 32, 37). Upstream flow has decreasing wind speed from mountaintop level to above (Figs. 40 a, b, c, d).

The presence of critical level results in different wave types. Without the critical level, vertical wave propagation is weakened due to the vertical structure of stability and wind shear. The model simulated w-component along the vertical cross section in TRAP1, TRAP2, and TRAP3 (Fig. 41) suggest multiple wave trains triggered by topography, propagating both upwards and eastwards. The vertical oscillations in Figure 41e is not as strong as others, because the cold front already influenced the northern part

of O‘ahu in TRAP3 at that moment, and the Scorer Parameter was almost constant through surface to inversion height (Fig. 25g). With a critical level during a downslope wind storm case, the vertical propagation of energy is strongly suppressed. Vertical oscillations are limited to the lower layer and decays rapidly with height (Fig. 42).

An inversion at the mountaintop level is a common element for downslope wind storms and trapped lee wave development, as shown by soundings (Figs. 9, 12, 15, 22, 32 and 37). However, the importance of inversion is different. The trapped lee waves need a stable layer for buoyancy oscillations. The more stable the atmosphere is, the stronger the restoring force is. Therefore the lee wave amplitude is maximum at the inversion layer with the greatest static stability, decreasing both upwards and downwards. The inversion layer acts as a lid to confine vertical propagation in the downslope wind and mountain wave cases.

In summary, common elements for trapped lee waves and downslope winds include strong low level wind, a wind direction perpendicular to the mountain ridge, and the existence of an inversion. The cross-barrier flow should be strong enough, so that the decrease of L^2 from lower layer to upper layer is greater than $\frac{\pi^2}{4H^2}$. If taken 2 to 2.5 km as the typical height of inversion before a cold front, the difference should be greater than 0.39 to 0.62 km^{-2} . However, the wind profile is significantly different between them. Trapped lee wave development requires increasing wind speed through the inversion and no critical level aloft. Conversely, a decreasing wind speed up to the critical level will produce a downslope wind.

Chapter 8

Impact of Latent Heat Release

The effects of latent heat release on the airflow cannot be ignored (Ogura 1963; Takeda 1971). In addition to the vertical wind shear, a cross-barrier flow, and a stable layer, latent heat release may be another factor that influences the wavelengths as well as the wave amplitudes for trapped lee waves. A parcel of fluid, if displaced vertically upward, will cool at the adiabatic lapse rate. If it is initially saturated, water condenses out and heats the parcel (Kuo 1961, 1965). The buoyancy restoring force is decreased (Durran and Klemp 1982a). Therefore, the upward movement of oscillations will be amplified.

Lalas and Einaudi (1974) have shown that in a saturated environment, the linear wave equations have exactly the same form as that for a dry atmosphere, if the stability parameter is appropriately altered to include the influence of moist processes. The commonly-used formula for the Brunt–Väisälä frequency is valid for an unsaturated dry atmosphere. When the atmosphere is saturated, the effective Brunt–Väisälä frequency N_m changes (Durran and Klemp 1982a; Lalas and Einaudi 1974; Dudis 1972; Hobbs et al. 1973). The estimated N_m should be smaller than the dry Brunt–Väisälä frequency. For most situations, the wave response is significantly more complicated than that predicted by simply replacing the dry stability with an equivalent moist stability in the saturated layer (Durran and Klemp 1982). With the aid of two-dimensional numerical simulations, Durran and Klemp (1982) concluded that the resonant waves in a stable

stratified environment are distorted by an increase in moisture. Changes in the humidity in the upper layer are found to amplify or damp the wave response, depending on the depth of the lower layer.

In order to compare the wave structures with different amounts of latent heat release, a series of model sensitivity tests are conducted. For the wintertime case of 26-27, January 2010. The control run is the simulation with the same model set-up as described earlier. Two model sensitive tests, RH80 and RH30, are performed and compared with the control run with reducing relative humidity to 80% and 30% of the original values throughout the whole vertical layers, respectively.

Figure 43 is the vertical distribution of relative humidity and potential temperature along the cross section shown in Figure 16. With sufficient moisture in the control run, abundant lenticular clouds are simulated over the mountaintop and on the lee side. In the RH80 run (Fig. 43c, d), moisture with relative humidity greater than 90% are limited in the upslope region and over the mountain, whereas in RH30, no clouds are simulated and it is a dry case without latent heat release.

As the latent heat reduces, the lee wave in horizontal direction has smaller amplitudes. The stability is lowered due to the release of latent heat associated with condensation process. The maximum wave amplitude in RH30 is only 2/3 of that in the control run (Figs 43 a, b, e, and f). Aside from wave amplitude, wavelength also varies with changing latent heat release amount. With more moisture content in the airflow,

wave crests are widened and wavelengths are longer. In the control run, the wavelengths at the 2-km level were about twice of that in the RH30 simulation (Figs 43a, b, e, and f).

Table 3 shows the observed wavelengths during the mature stage of three wintertime trapped lee wave cases, and the calculated wavelengths from equation (9) respectively. Without considering the influence of latent heat release on wavelength, equation (9) underestimates the wavelengths by about 40% to 55%. The existence of latent heat will result in longer wavelengths and larger wave amplitudes.

Correspondingly, horizontal wave number k is overestimated without taking latent heat release into account.

Chapter 9

Conclusion

9.1 Summary of Trapped Lee Wave Development Conditions

Trapped lee waves can occur over O‘ahu under a stronger pre-frontal southwesterly flow regime in wintertime and under the influence of an upper-level disturbance in summer. The essential factors are the same: (1) Strong low-level winds with $Fr > 1$ impinging on the mountain ridges; (2) abundant low-level moisture and sufficient lifting for condensation; (3) a stable layer for buoyancy oscillations; (4) increasing wind speed with respect to height through the inversion and no critical level aloft. Only with a mountain height greater than the LCL and $Fr > 1$, could trapped lee wave clouds possibly form in the lower troposphere. With maximum ridges height around 0.9-1.2 km, O‘ahu has the most frequently observed trapped lee wave clouds compared to the other Hawaiian Islands.

During summertime, when an upper-level low shifts the prevailing westerlies into northeasterlies, the wind profile has no critical level, and is thus favorable for trapped lee wave development. In low levels, the subtropical high pressure cell strengthens, the pressure gradient over the island of O‘ahu intensifies, and northeasterly trade winds are relatively strong. In wintertime, favorable synoptic conditions for trapped lee waves include an approaching cold front, strengthening pre-frontal southwesterlies and a weakened subtropical high retreating eastwards. An inversion is essential in summer as well as in winter. Without sufficient moisture, trapped lee wave clouds hardly form and

cannot be observed from the satellite images. Under relatively dry conditions, lee waves may exist as clear air turbulences.

Model simulated environmental conditions and wave structure demonstrate the three-layer stratification. At the inversion, the Scorer parameter L^2 are maximum, wave amplitude are the greatest and wavelength are the shortest. The evolution of upstream flow influences the wave structure, amplitude and wavelength. Under the presence of an inversion above the ridge tops, the wind speed increases with a large wind component perpendicular to the mountain ridge. The Scorer parameter decreases with respect to height. For $Fr > 1$, lee side oscillations occur. The maximum wave amplitude is at the inversion layer. With strong cross-barrier flow, wavelengths are longer and lenticular clouds propagate farther downstream. After upstream airflow weakens or wind direction shifts, the wavelength shortened with a decrease in Fr , trapped lee waves decay correspondingly. Once the wind shear is weakened or inversion no longer exists, the trapped lee wave event ends.

The inversion above the mountaintop and a strong cross-barrier flow are essential in both trapped lee wave development and downslope winds. The vertical wind profile is crucial to determine whether trapped lee waves or downslope winds will occur. In the wintertime, the pre-frontal southwesterly flow regime with upper-level westerlies is the favorable large scale setting for the occurrences of trapped lee waves. In the summertime, with the persistent north/northeasterly trade-wind flow in low levels and westerly flow aloft, trapped lee waves do not occur frequently. Only if the upper-level

wind shifts to easterlies, could the trapped lee waves possibly occur under summer trade-wind weather. If the low-level winds decrease with height and the winds reverse its direction with the existence of a critical level aloft, a downslope wind storm or mountain wave event may occur instead of trapped lee waves.

The influence of latent heat on trapped lee waves is significant on the wave amplitude as well as wavelengths. From model sensitivity tests and comparing observations with calculations, it is confirmed that latent heat release will reduce the stability and thus amplify the wave amplitude, and widen the wave crests producing longer wavelengths.

At this time, the evolution of trapped lee waves can only be monitored by the 1-km visible GOES data during the daytime. It is possible to improve the real-time forecast of trapped lee waves with higher resolution satellite data in conjunction with high-resolution models with a horizontal grid on the order of 1 km. In the future, Geostationary Operational Environmental Satellite R-Series (GOES-R) is able to deliver 0.5-km visible (0.64 μm), 1-km multispectral true color, and 2-km short-wave IR (3.9 μm)/ multiple channel fog product every 5 minutes. GOES-R datasets is a promising tool for model verification and monitoring of trapped lee wave events during the daytime in addition to the visible channel data (0.64 μm). At night, the shortwave IR/ fog product from GOES-R with higher spatial and temporal resolution will be useful for validation of model results.

9.2 Implications for Forecasting

Forecasting the occurrence of low-level mountain waves over mountainous terrain is very challenging yet crucial. On 14 February, 2015, heavy showers with winds up to 26 m s^{-1} occurred over the Hawaiian Islands during the passage of a cold front. Trapped mountain lee waves were observed on satellite VIS images in the northeastern leeside of O‘ahu under strong prefrontal southwesterly flow, and were simulated by the real-time high-resolution model. The United Airlines Flight 15 from Newark to Honolulu encountered sudden turbulence during landing around 0400 HST, 14 February, 2015. Seven passengers on board were injured (Hawaiian News Now, 14 Feb 2015). More than 2,000 residents of in the northeastern coastal areas of the Temple Valley, Punaluu, and Kaneohe had lost power due to the wind storms and turbulence (Daily Mail, 15 February 2015). Accurate forecasts of trapped lee waves or downslope wind storms are important to tourisms, aviation safety and local communities.

The high-resolution mesoscale numerical models could provide valuable numerical guidance for the onset, development, and dissipation of trapped lee wave events in Hawai‘i. For the satellite observations of trapped mountain lee waves, current GOES VIS images with an 1-km resolution is adequate to capture these types of events during the daytime. At night, the current infrared images shortwave IR with a horizontal grid $\sim 4 \text{ km}$ are ineffective in monitoring the lee wave clouds. Future GOES-R satellite shortwave IR images (or fog product) with a horizontal grid of 2 km every 5 minutes could be useful for monitoring this type of event at night. Nevertheless, low-level

trapped lee waves could possibly occur as clear sky turbulences if not enough moisture is present. Therefore, the monitoring and prediction of trapped mountain lee wave events requires a combination of satellite observations and high-resolution mesoscale numerical model with a horizontal grid on the order of 1 km.

The results from this study improve our basic understanding of the occurrence of trapped lee wave forecasting over the Hawaiian Islands. During the wintertime, if the surface map or the 850 hPa level chart shows an approaching mid-latitude cyclone with a cold front to the northwest of the O‘ahu, trapped lee wave event could possibly occur in the northeastern lee-side of the major Hawaiian Islands with tops or ridge heights below the trade-wind inversion, especially O‘ahu. The 850-hPa charts as well as the Lihue soundings could possibly be used to estimate the prefrontal wind speed of the southwesterly flow, the vertical wind profile, the trade-wind inversion height and Fr to assess the likelihood of the occurrences of trapped lee wave events in the lee-side of each island. The propagating speed of the cold front could possibly be determined by the surface charts every 6 hours to estimate the approximately time that the trapped lee waves could possibly occur. Nevertheless, the Lihue soundings are available only every twelve hours and trapped lee wave events typically only last 12-18 hours. The 12-hourly soundings are marginal in resolving the temporal resolution of the vertical structure of the atmosphere to assess the timing of the initiation and duration of these events. In this regards, high-resolution models with hourly output would provide value aided information in advance.

In summertime, the typical wind profile is characterized by decreasing wind speed through the trade-wind inversion with a critical level aloft under summer trade-wind conditions. Thus, trapped lee wave events are rare. Our study shows that if an omega blocking exists aloft, the upper-level westerlies would be replaced by easterlies with strong low-level winds with increasing wind speed through inversion, allowing trade lee waves to occur. Thus, sounding data as well as upper-level charts would be useful to assess if trapped lee waves could possibly occur.

References

- Aanensen, C. J. M., 1965: Gales in Yorkshire in February 1962. *Geophysical Memoirs*, Meteorological Office, London, p. 108.
- Atkinson, B. W., 1981: Meso-scale atmospheric circulations. Academic Press, London; New York, 25–79.
- Blumenstock, D. I., and S. Price, 1967: Climates of the United States: Hawaii. *Climates of the United States: Hawaii*, U. S. Govt. Printing Office, Washington, D. C., p. 27.
- Brinkmann, W. A. R., 1974: Strong Downslope Winds at Boulder, Colorado. *Mon. Weather Rev.*, **102**, 592–602.
- Burroughs, L. D., and R. N. Larson, 1979: Wave Clouds in the Vicinity of Oahu Island. *Mon. Weather Rev.*, **107**, 608–611.
- Caccia, J., B. Benech, and V. Klaus, 1997: Space-time description of nonstationary trapped lee waves using ST radars, aircraft, and constant volume balloons during the PYREX experiment. *J. Atmos. Sci.*, **54**, 1821–1833.
- Carlis, D. N. L., Y.-L. Chen, and V. R. Morris, 2010: Numerical Simulations of Island-scale Airflow over Maui and the Maui Vortex under Summer Trade-wind Conditions. *Mon. Weather Rev.*, **138**, 100802101247096, doi:10.1175/2010MWR3236.1.
- Colman, B. R., and Carl F. Dierking, 1992: The Taku Wind of Southeast Alaska--its Identification and Prediction.pdf. *Weather Forecast.*, **7**.
- Doyle, J. D., and D. R. Durran, 2002: The Dynamics of Mountain-Wave-Induced Rotors. *J. Atmos. Sci.*, **59**, 186–201, doi:10.1175/1520-0469(2002)059<0186:TDOMWI>2.0.CO;2.
- Dudis, J. J., 1972: The Stability of a Saturated, Stably-Stratified Shear Layer. *J. Atmos. Sci.*, doi:10.1175/1520-0469(1972)029<0774:TSSOASS>2.0.CO;2.
- Durran, D., and J. Klemp, 1982a: On the effects of moisture on the Brunt-Väisälä frequency. *J. Atmos. Sci.*, **39**, 2152–2158.
- , and ———, 1982b: The effects of moisture on trapped mountain lee waves. *J. Atmos. Sci.*, **39**, 2490–2506.

- Durrán, D. R., 1986: Another Look at Downslope Windstorms. Part 1: The Development of Analogs to Supercritical Flow in an Infinitely Deep, Continuously Stratified Fluid. *J. Atmos. Sci.*, **43**, 2527–2543.
- Durrán, D. R., 2003: Lee Waves and Mountain Waves. *Encycl. Atmos. Sci.*, 13, doi:10.1175/1520-0469(1982)039<2490:TEOMOT>2.0.CO;2. http://www.atmos.washington.edu/2010Q1/536/2003AP_lee_waves.pdf.
- Epifanio, C. C., and R. Rotunno, 2005: The Dynamics of Orographic Wake Formation in Flows with Upstream Blocking. *J. Atmos. Sci.*, **62**, 3127–3150, doi:10.1175/JAS3523.1.
- Gjevik, B., and T. Marthinsen, 1978: Three-dimensional lee-wave pattern. *Q. J. R. Meteorol. Soc.*, **104**, 947–957.
- Hobbs, P. V., R. C. Easter, and A. B. Fraser, 1973: A Theoretical Study of the Flow of Air and Fallout of Solid Precipitation Over Mountainous Terrain: Part II. Microphysics. *J. Atmos. Sci.*, **30**, 813–823, doi:10.1175/1520-0469(1973)030<0813:ATSOTF>2.0.CO;2.
- Hong, S.-Y., Y. Noh, and J. Dudhia, 2006: A New Vertical Diffusion Package with an Explicit Treatment of Entrainment Processes. *Mon. Weather Rev.*, **134**, 2318–2341, doi:10.1175/MWR3199.1.
- Iacono, M. J., J. S. Delamere, E. J. Mlawer, M. W. Shephard, S. a. Clough, and W. D. Collins, 2008: Radiative forcing by long-lived greenhouse gases: Calculations with the AER radiative transfer models. *J. Geophys. Res. Atmos.*, **113**, 2–9, doi:10.1029/2008JD009944.
- Janjić, Z. I., 1994: The Step-Mountain Eta Coordinate Model: Further Developments of the Convection, Viscous Sublayer, and Turbulence Closure Schemes. *Mon. Weather Rev.*, **122**, 927–945, doi:10.1175/1520-0493(1994)122<0927:TSMECM>2.0.CO;2.
- , 2000: Comments on “Development and Evaluation of a Convection Scheme for Use in Climate Models.” *J. Atmos. Sci.*, **57**, 3686–3686, doi:10.1175/1520-0469(2000)057<3686:CODAEO>2.0.CO;2.
- Klemp, J., and D. Lilly, 1978: Numerical simulation of hydrostatic mountain waves. *J. Atmos. Sci.*, **35**, 78–107.
- Klemp, J. B., and D. R. Lilly, 1975: The Dynamics of Wave-Induced Downslope Winds. *J. Atmos. Sci.*, **32**, 320–339, doi:10.1175/1520-0469(1975)032<0320:TADOWID>2.0.CO;2.

- Kuo, H. L., 1961: Convection in Conditionally Unstable Atmosphere. *Tellus*, **13**, 441–459.
- Lalas, D. P., and F. Einaudi, 1974: On the Correct Use of the Wet Adiabatic Lapse Rate in Stability Criteria of a Saturated Atmosphere. *J. Appl. Meteorol.*, **13**, 318–324, doi:10.1175/1520-0450(1974)013<0318:OTCUOT>2.0.CO;2.
- Lilly, D. K., 1978: A Severe Downslope Windstorm and Aircraft Turbulence Event Induced by a Mountain Wave. *J. Atmos. Sci.*, **35**, 59–77, doi:10.1175/1520-0469(1978)035<0059:ASDWAA>2.0.CO;2.
- Lindsay, C. V., 1962: MOUNTAIN WAVES IN THE APPALACHIANS. *Mon. Weather Rev.*, **90**, 271–276, doi:10.1175/1520-0493(1962)090<0271:MWITA>2.0.CO;2.
- Lupo, A. R. and P. J., Smith, 1995: Planetary and synoptic-scale interactions during the life cycle of a mid-latitude blocking anticyclone over the North Atlantic.
- Mason, D., 1954: Hill standing waves and safety heights. *Weather*, **9**, P45.
- Nance, L. B., and D. R. Durran, 1997: A Modeling Study of Nonstationary Trapped Mountain Lee Waves. Part I: Mean-Flow Variability. *J. Atmos. Sci.*, **54**, 2275–2291, doi:10.1175/1520-0469(1997)054<2275:AMSONT>2.0.CO;2. *Tellus A*, **64**, 3-28.
- Van Nguyen, H., Y.-L. Chen, and F. Fujioka, 2010: Numerical Simulations of Island Effects on Airflow and Weather during the Summer over the Island of Oahu. *Mon. Weather Rev.*, **138**, 2253–2280, doi:10.1175/2009MWR3203.1. <http://journals.ametsoc.org/doi/abs/10.1175/2009MWR3203.1> (Accessed May 7, 2014).
- Nicholls, J. M., 1973: The airflow over mountains: research 1958-1972. *WMO Tech. Note*, **127**.
- Ogura, Y., 1963: The Evolution of a Moist Convective Element in a Shallow, Conditionally Unstable Atmosphere: A Numerical Calculation. *J. Atmos. Sci.*, **20**, 407–424, doi:10.1175/1520-0469(1963)020<0407:TEOAMC>2.0.CO;2.
- Pilsbury, R. K., 1955: Preliminary analysis of standing wave reports received at Northolt during the winter of 1953-54. *Meteorol. Mag.*, **84**, 313.
- Queney, P., 1948: The problem of air flow over mountains: A summary of theoretical studies. *Bull. Am. Meteorol. Soc.*, **29**, 16–26.
- Ralph, F., and P. Neiman, 1997: Observations, simulations, and analysis of nonstationary trapped lee waves. *J. ...*, **54**, 1308–1333.

- Ramage, C. S., 1962: The subtropical cyclone. *J. Geophys. Res.*, **67**, 1401–1411, doi:10.1029/JZ067i004p01401.
- Reeder, M. J., N. Adams, and T. P. Lane, 1999: Radiosonde observations of partially trapped lee waves over Tasmania, Australia. *J. Geophys. Res.*, **104**, 16719, doi:10.1029/1999JD900038.
- Roger, E., T. Black, B. Ferrier, D. Parrish, and G. DiMego, 2001: Changes to the NCEP Meso Eta analysis and forecast system: Increase in resolution, new cloud microphysics, modified precipitation assimilation, modified 3DVAR analysis. *Web doc.*, <http://www.emc.ncep.noaa.gov/mmb/mmbpll/eta12tpb/>.
- Rotunno, R., V. Grubišić, and P. K. Smolarkiewicz, 1999: Vorticity and Potential Vorticity in Mountain Wakes. *J. Atmos. Sci.*, **56**, 2796–2810, doi:10.1175/1520-0469(1999)056<2796:VAPVIM>2.0.CO;2.
- Saha, S., and Coauthors, 2010: NCEP Climate Forecast System Reanalysis (CFSR) 6-hourly Products, January 1979 to December 2010. Research Data Archive at the National Center for Atmospheric Research, Computational and Information Systems Laboratory, Boulder, CO. [Available online at <http://dx.doi.org/10.5065/D69K487J>]. Accessed 02 March, 2015.
- Saha, S., and Coauthors, 2011: NCEP Climate Forecast System Version 2 (CFSv2) 6-hourly Products. Research Data Archive at the National Center for Atmospheric Research, Computational and Information Systems Laboratory, Boulder, CO. [Available online at <http://dx.doi.org/10.5065/D61C1TXF>]. Accessed 27 October, 2014.
- Schär, C., and R. B. Smith, 1993: Shallow-Water Flow past Isolated Topography. Part I: Vorticity Production and Wake Formation. *J. Atmos. Sci.*, **50**, 1373–1400, doi:10.1175/1520-0469(1993)050<1373:SWFPIT>2.0.CO;2.
- , and D. R. Durran, 1997: Vortex Formation and Vortex Shedding in Continuously Stratified Flows past Isolated Topography. *J. Atmos. Sci.*, **54**, 534–554, doi:10.1175/1520-0469(1997)054<0534:VFAVSI>2.0.CO;2.
- Schroeder, T., 1993: Climate controls. *Prevailing Trade Winds: Climate and Weather in Hawaii*, M. Sanderson, Ed., University of Hawaii Press, 12–36.
- Scorer, R. S., 1949: Theory of Waves in the Lee of Mountains. *Q. J. R. Meteorol. Soc.*, **75**, 41–56, doi:10.1002/qj.49707532308.
- Simpson, R. H., 1952: Evolution of the Kona Storm a Subtropical Cyclone. *J. Meteorol.*, **9**, 24–35, doi:10.1175/1520-0469(1952)009<0024:EOTKSA>2.0.CO;2.

- Smith, R. B., 1985: On Severe Downslope Winds. *J. Atmos. Sci.*, **42**, 2597–2603, doi:10.1175/1520-0469(1985)042<2597:OSDW>2.0.CO;2.
- Smolarkiewicz, P. K., and R. Rotunno, 1989: Low Froude Number Flow Past Three-Dimensional Obstacles. Part I: Baroclinically Generated Lee Vortices. *J. Atmos. Sci.*, **46**, 1154–1164, doi:10.1175/1520-0469(1989)046<3611:COFNFP>2.0.CO;2.
- , R. M. Rasmussen, and T. L. Clark, 1988: On the Dynamics of Hawaiian Cloud Bands. Island Forcing. *J. Atmos. Sci.*, **45**, 1872–1905, doi:10.1175/1520-0469(1993)050<1560:OTDOHC>2.0.CO;2.
- Sonia, P. J., O. J. James, and R. P. Thomas, 1998: Atlas of Hawaii.
- Starr, J. R., and K. A. Browning, 1972: Observations of lee waves by high power radar. *Q. J. R. Meteorol. Soc.*, **98**, 73–85.
- Takeda, T., 1971: Numerical Simulations of a Precipitating Convective Cloud: The Formation of a “Long-Lasting” Cloud. *J. Atmos. Sci.*, **28**, 350–376.
- Vachon, P. W., O. M. Johannessen, and J. A. Johannessen, 1994: An ERS 1 synthetic aperture radar image of atmospheric lee waves. *J. Geophys. Res.*, **99**, 22,482–22,490.
- Wallington, C. E., 1960: An introduction to lee waves in the atmosphere. *Weather*, **15**, 269–276.
- Yang, Y., and Y.-L. Chen, 2008: Effects of Terrain Heights and Sizes on Island-Scale Circulations and Rainfall for the Island of Hawaii during HaRP. *Mon. Weather Rev.*, **136**, 120–146, doi:10.1175/2007MWR1984.1. <http://journals.ametsoc.org/doi/abs/10.1175/2007MWR1984.1> (Accessed May 10, 2014).
- , ———, and F. M. Fujioka, 2005: Numerical Simulations of the Island-Induced Circulations over the Island of Hawaii during HaRP. *Mon. Weather Rev.*,.
- Zhang, Y., Y. Chen, and K. Kodama, 2005: Validation of the Coupled NCEP Mesoscale Spectral Model and an Advanced Land Surface Model over the Hawaiian Islands . Part II : A High Wind Event. *Weather Forecast.*, **20**, 873–895.

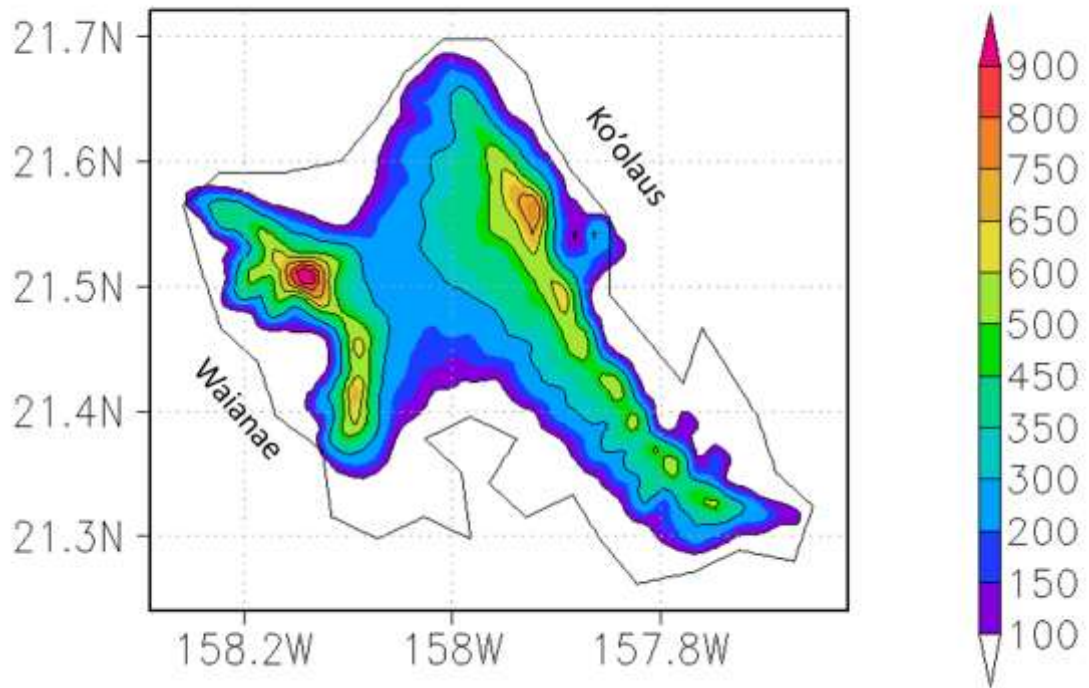


Figure 1. ARW Elevation contour over the island of O'ahu in the unit of meters.

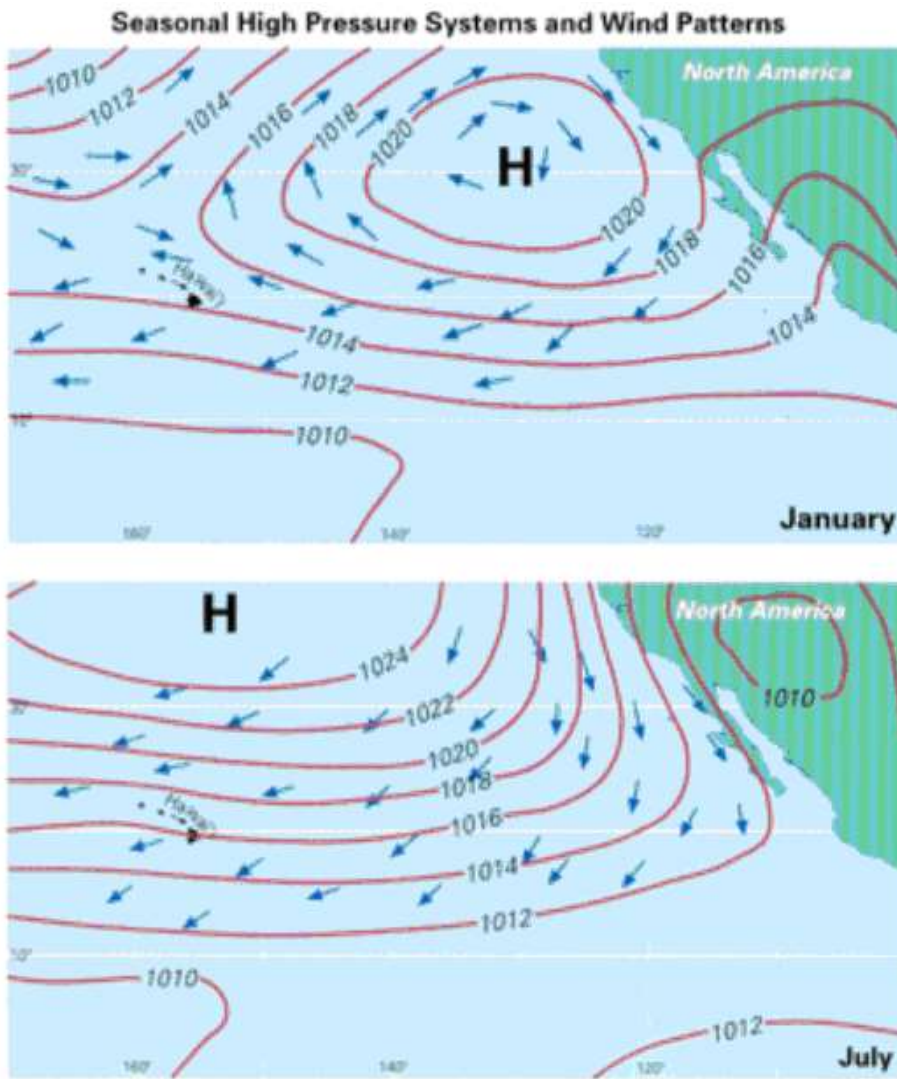


Figure 2. Climatological high pressure system and wind pattern over the Hawaiian Islands in January (upper Figure) and July (bottom Figure) in the unit of hPa. From Atlas of Hawai‘i. Chapter 2 the Physical Environment. (Schroeder, 1993)

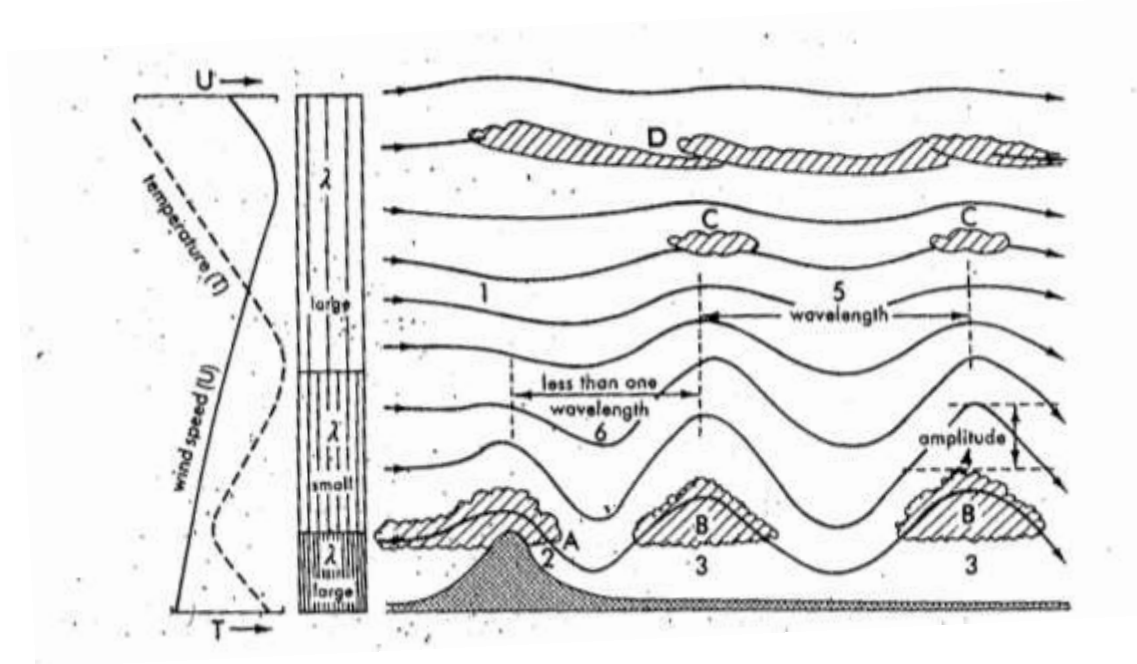


Figure 3. Features of airflow across a long mountain range: (1) downdraft may occur at some levels to windward of ridge; (2) strong surface wind down lee slope; (3) variable surface wind; (4) maximum amplitude in stable layer; (5) order of wavelengths, 5-30 km; (6) first wave crest usually less than one wavelength downstream of ridge. (A) Foehnwall; (B) roll cloud; (C) altocumulus lenticularis; (D) cirrus, λ denotes the natural wavelength determined by the airstream wind and temperature conditions. (Wallington, 1960)

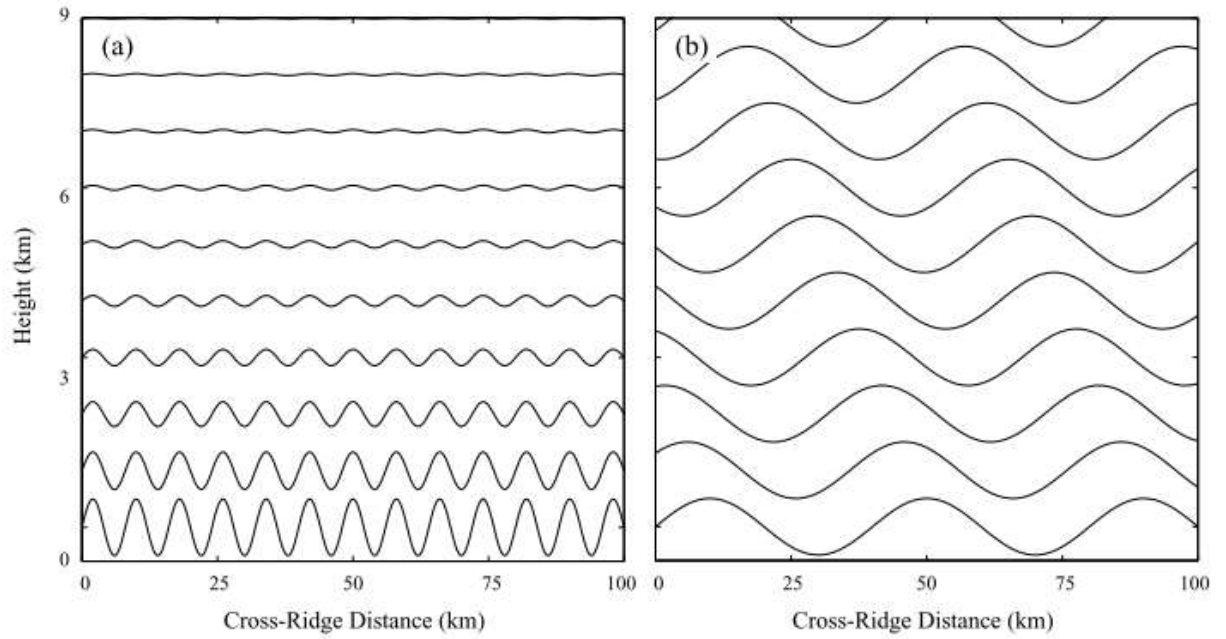


Figure 4. Streamlines in steady airflow over an infinite series of sinusoidal ridges when $N=0.01 \text{ s}^{-1}$, $U=15 \text{ m s}^{-1}$. m is the vertical wavenumber of mountain waves. The flow is from left to right, and the wavelengths of the topography are (a) 8 km (case $m^2 < 0$) (b) 40 km (case $m^2 > 0$). The lowest streamline coincides with the topography. (Durran, 2003)

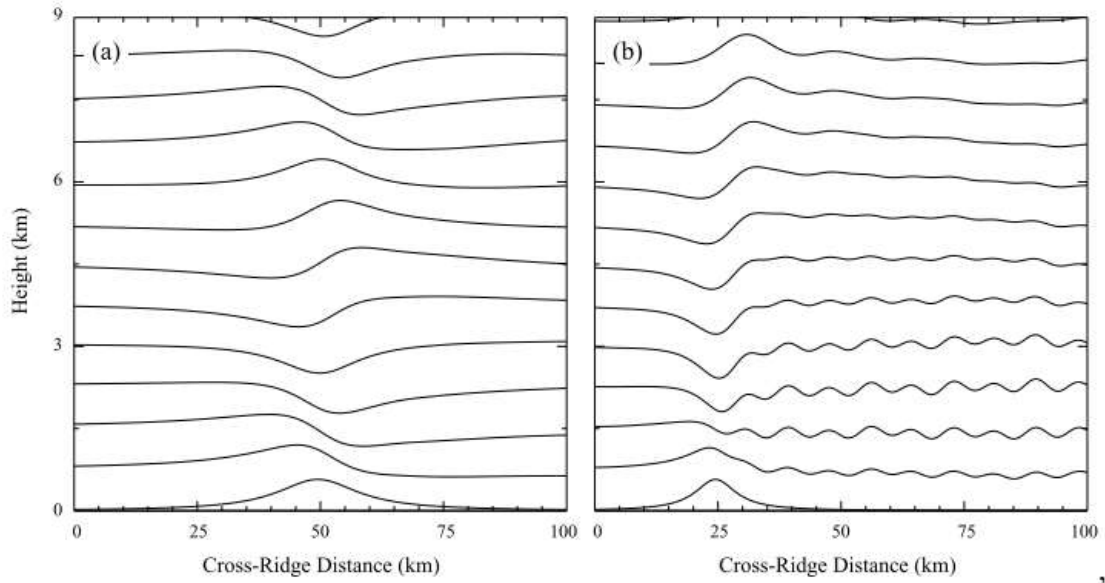


Figure 5. Streamlines in steady airflow over an isolated mountain series as predicted by linear theory when (a) mountain width is 10 km, N is constant, and $\frac{Nh_0}{U} = 0.06$ (b) mountain width is 5 km, N is constant throughout each of two layers such that between the surface and 3 km $\frac{Nh_0}{U} = 0.06$, and above 3 km $\frac{Nh_0}{U} = 0.24$.

Microphysics option	Ferrier microphysics
Long wave	Rrtmg_lw
Short wave	Rrtmg_sw
Surface-layer option	MM5 Monin-obukhov Scheme
Boundary-layer option	YSU from Yonsei University
Cumulus option	Betts-Miller-Janjic Scheme
Four layer of soil layers	Noah land-surface model

Table 1. WRF model set up in three trapped lee wave cases in winter time (24 January, 2003; 27 January, 2010; 26 January, 2014), a downslope wind storm case on 14-15 February, 2001 and a mountain wave case on 1 August, 2013 over O‘ahu.

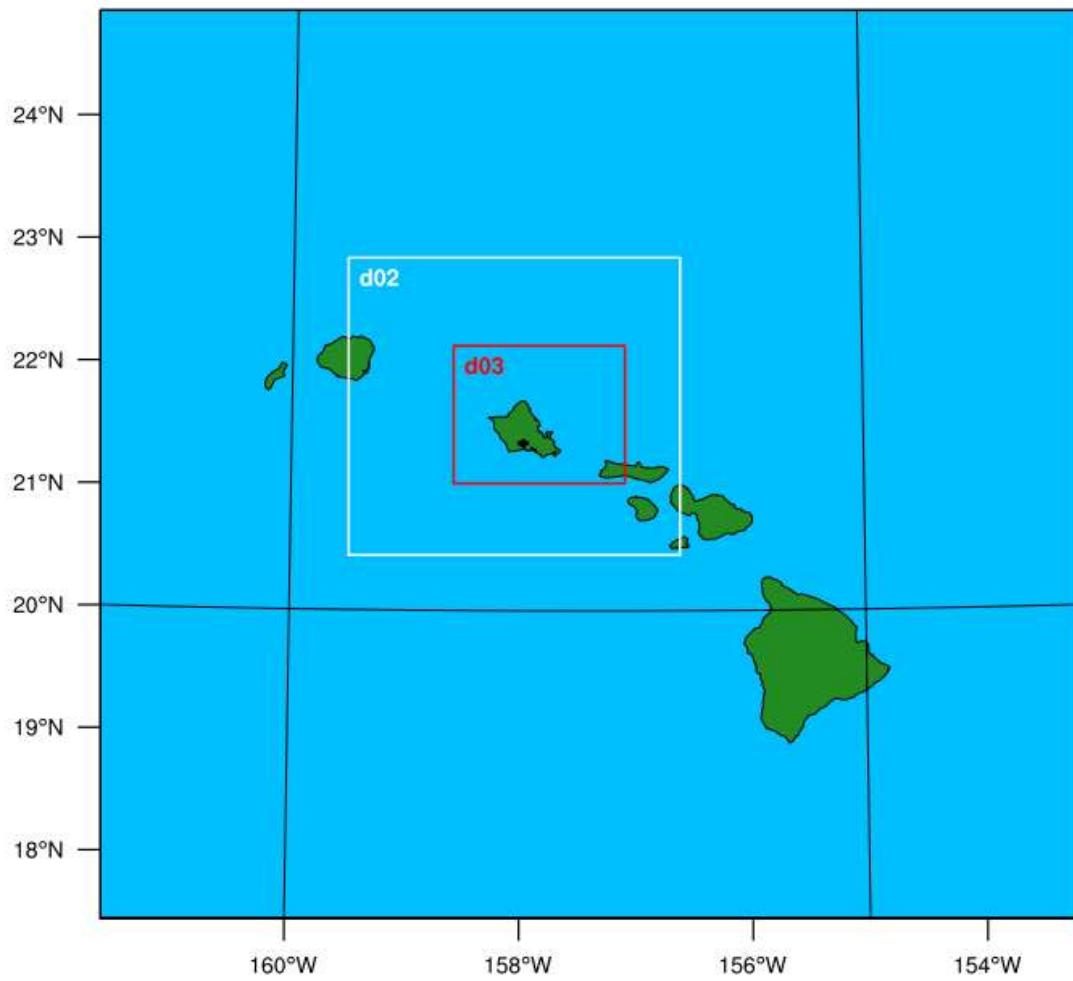


Figure 6. Model domain nesting for trapped lee wave cases in winter, 27 January, 2010 and 25 January, 2003. The resolution for three domains is 9 km, 3 km, and 1 km respectively.

	Trapped Lee Waves			Mountain Waves	Downslope Wind
Case	27 Jan, 2010	24 Jan, 2003	26 Jan, 2014	01 Aug, 2013	14 Feb, 2001
Initial time	1200 UTC, 25 January	1200 UTC, 22 January	1200 UTC, 25 January	1200 UTC, 30 July	1200 UTC< 13 February
Running hours	72 hour	72 hour	48 hour	48 hour	48 hour
Input data	CFSR	CFSR	CFSv2	CFSv2	CFSR
Input resolution	0.5°×0.5° 6hr				
Output resolution	Horizontal: 1km × 1km Vertical: 38 levels 1hr				

Table 2. Temporal and spatial resolution, initial time and total simulated hours, and input data sources used for WRF model in three trapped lee wave cases in winter time (24 January, 2003; 27 January, 2010; 26 January, 2014), a downslope wind storm case on 14-15 February, 2001 and a mountain wave case on 1 August, 2013 over O‘ahu.

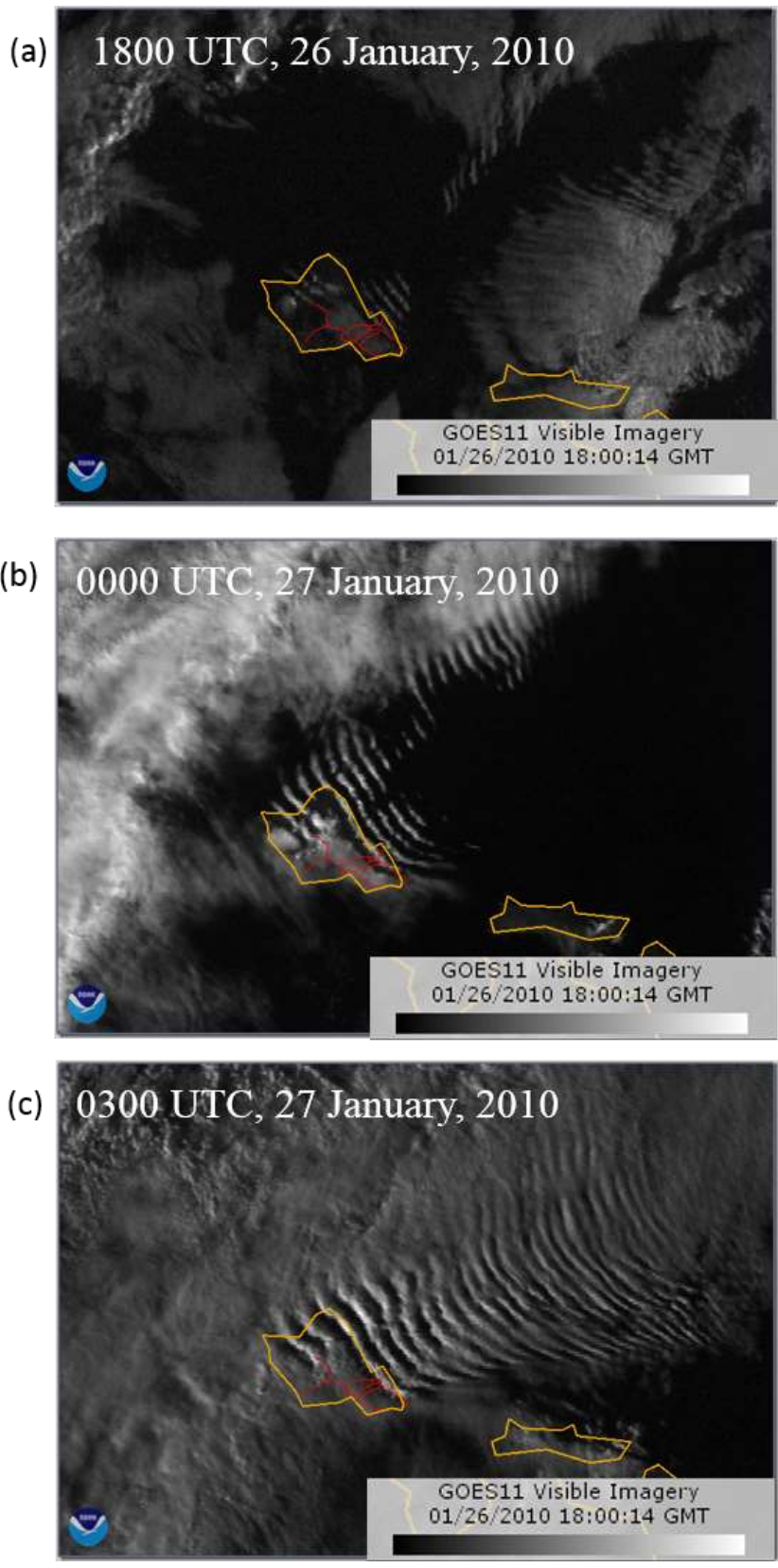


Figure 7. GOES-west visible satellite imagery for the Hawaiian Islands from early to mature stage of the trapped lee wave case on 27 January, 2010. The corresponding moment is (a) 1800 UTC, 26 January, (b) 0000 UTC, 27 January 2010 and (c) 0300 UTC, 27 January, 2010 (from Mauna Kea Weather Center)

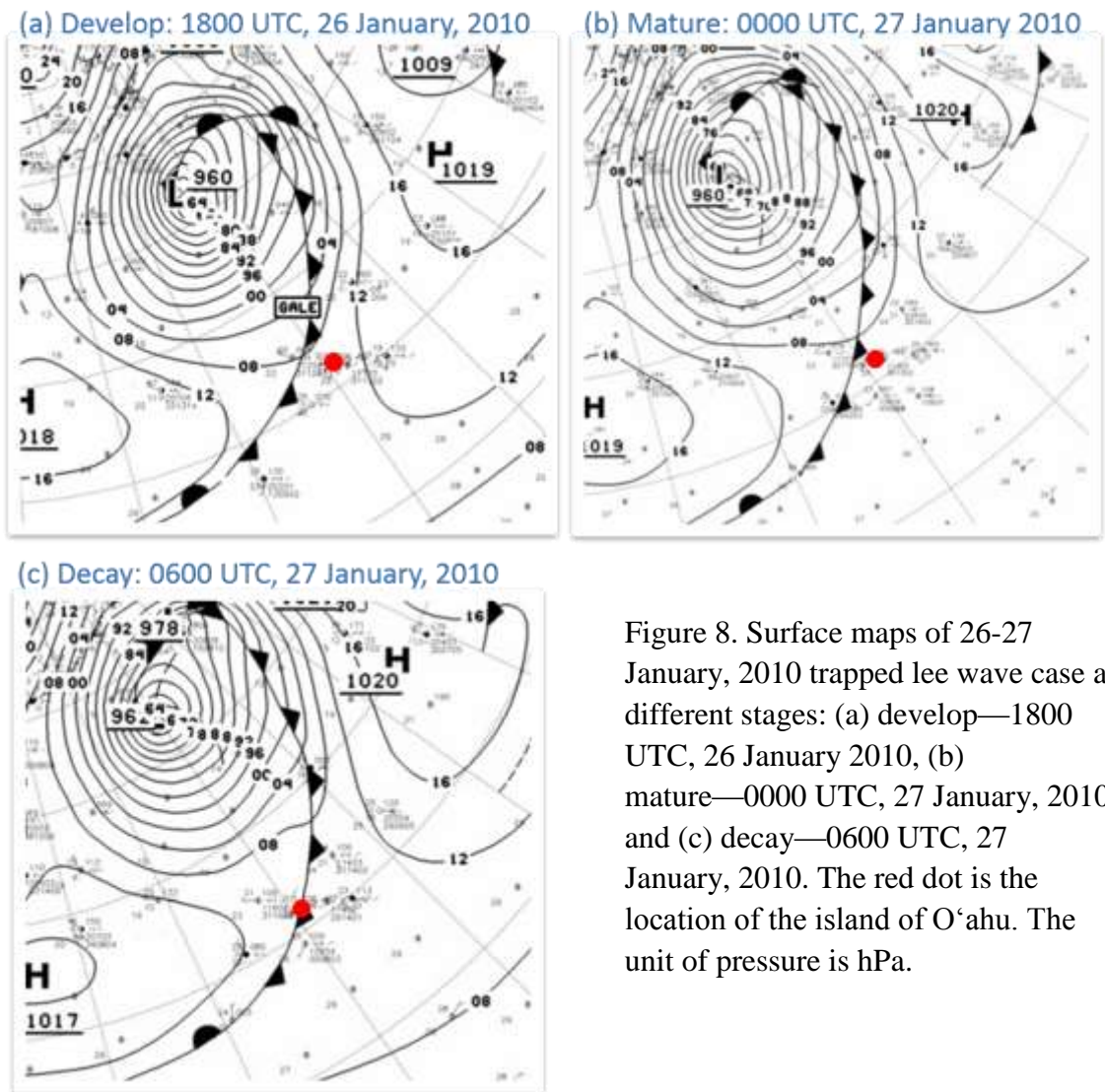


Figure 8. Surface maps of 26-27 January, 2010 trapped lee wave case at different stages: (a) develop—1800 UTC, 26 January 2010, (b) mature—0000 UTC, 27 January, 2010 and (c) decay—0600 UTC, 27 January, 2010. The red dot is the location of the island of O‘ahu. The unit of pressure is hPa.

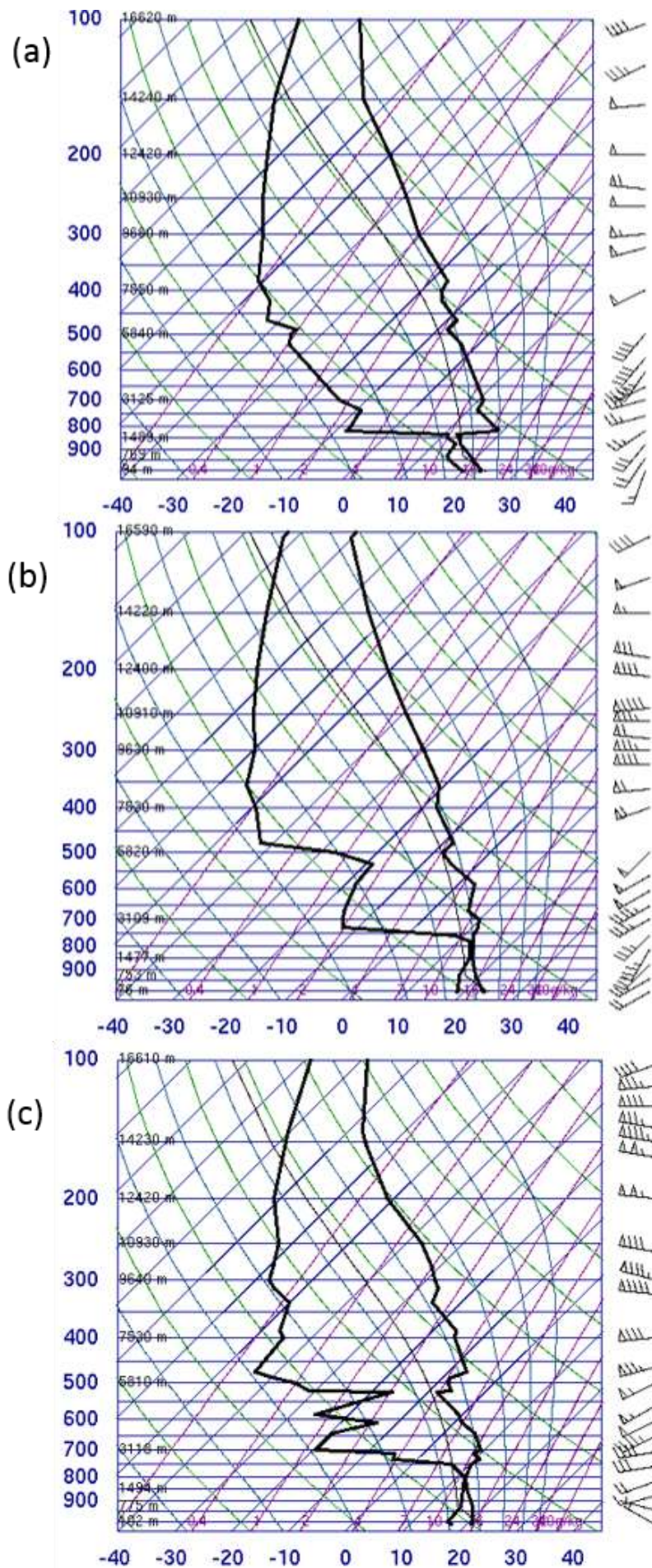


Figure 9. Sounding and wind profile at Lihue during different stages at the trapped lee wave case in 26-27 January 2010. The corresponding moment is (a) before: 1200 UTC, 26 January 2010; (b) mature: 0000 UTC, 27 January 2010 and (c) decay: 1200 UTC, 27 January 2010. (From University of Wyoming)

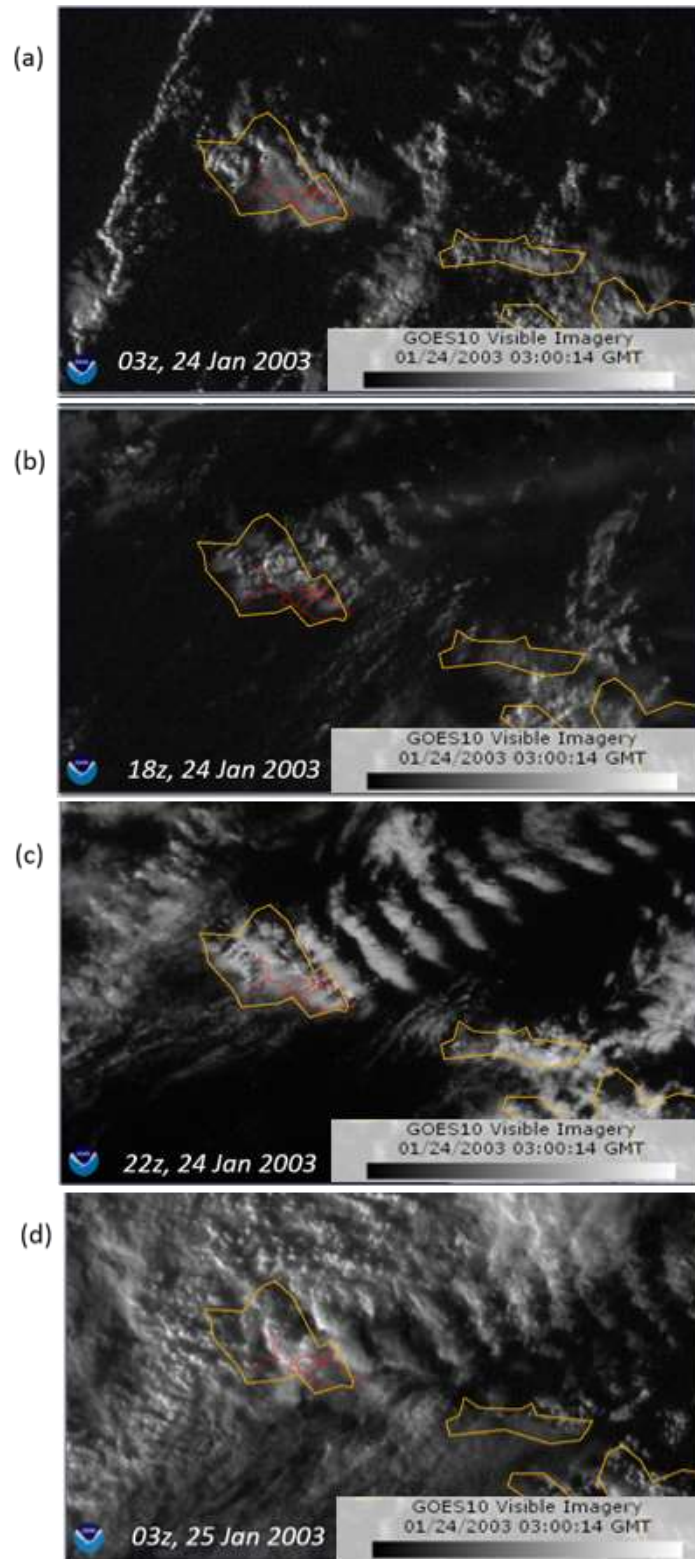


Figure 10. GOES-10 VIS satellite imagery for the trapped mountain lee wave case in 24-25 January 2003. The corresponding stage is (a) before: 0300 UTC, 24, January, 2003, (b) development: 1800 UTC, 24 January 2003; (c) mature: 2200 UTC, 24 January 2003; and (d) decay: 0300 UTC, 25 January 2003.

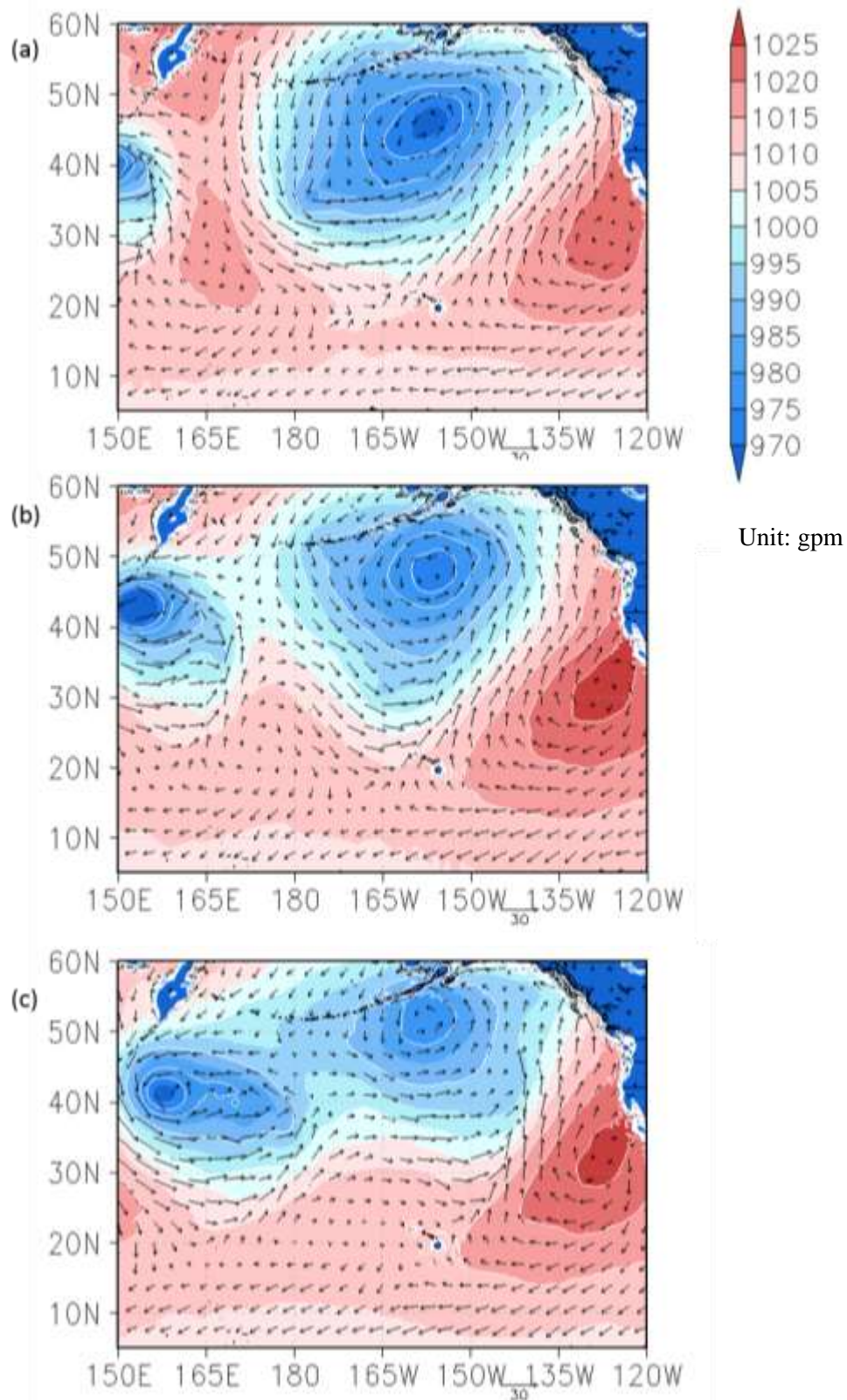


Figure 11. Synoptic pattern of surface pressure (shading) and wind (vector) in the unit of hPa at different wave evolution phase: (a) before: 0000 UTC, 24 January 2003; (b) development and mature: 1800 UTC, 24 January 2003; (c) decay: 1200 UTC, 25 January 2003.

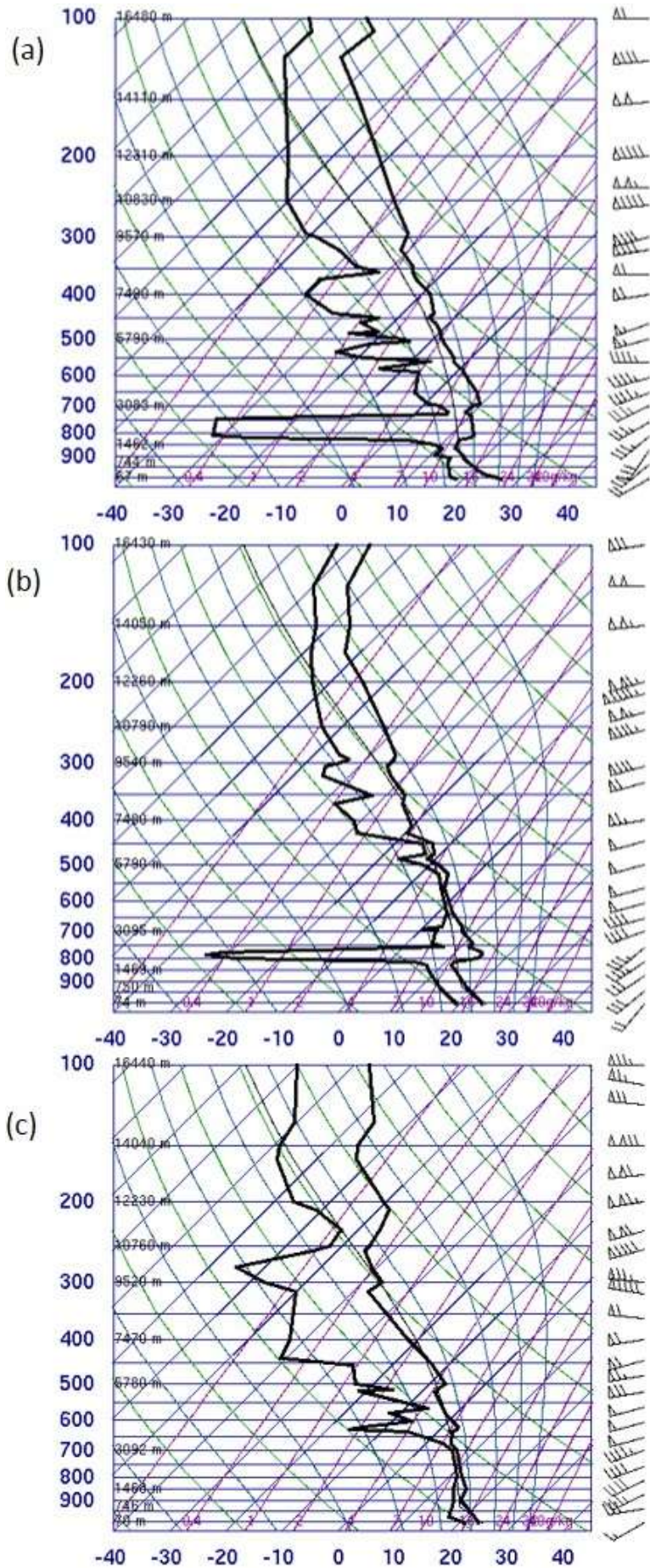


Figure 12. Sounding and wind profile at Lihue during different stage in the trapped lee wave case on 24-25 January 2003. The corresponding moment is (a) before: 1200 UTC, 23 January 2003; (b) develop: 1200 UTC, 24 January 2003 and (c) decay: 1200 UTC, 25 January 2003. (From University of Wyoming)

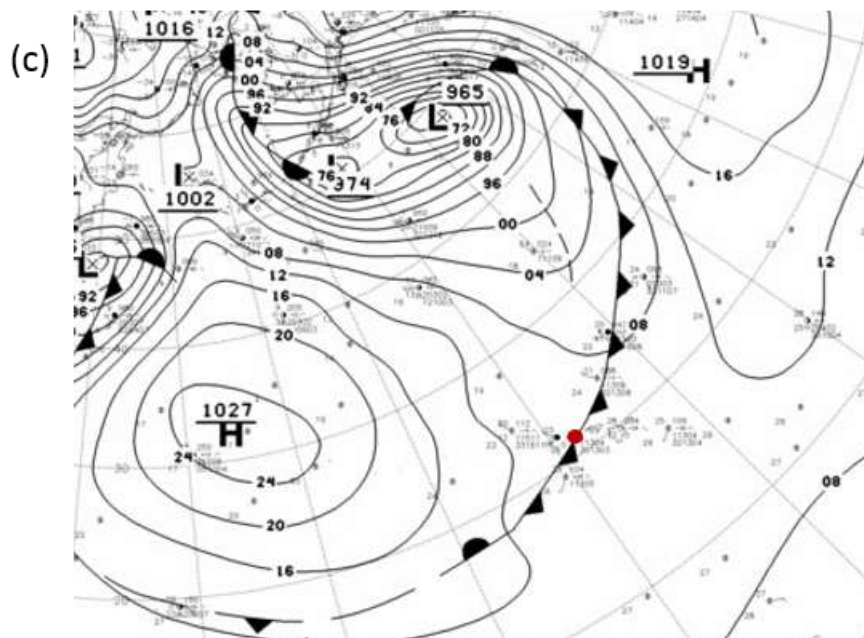
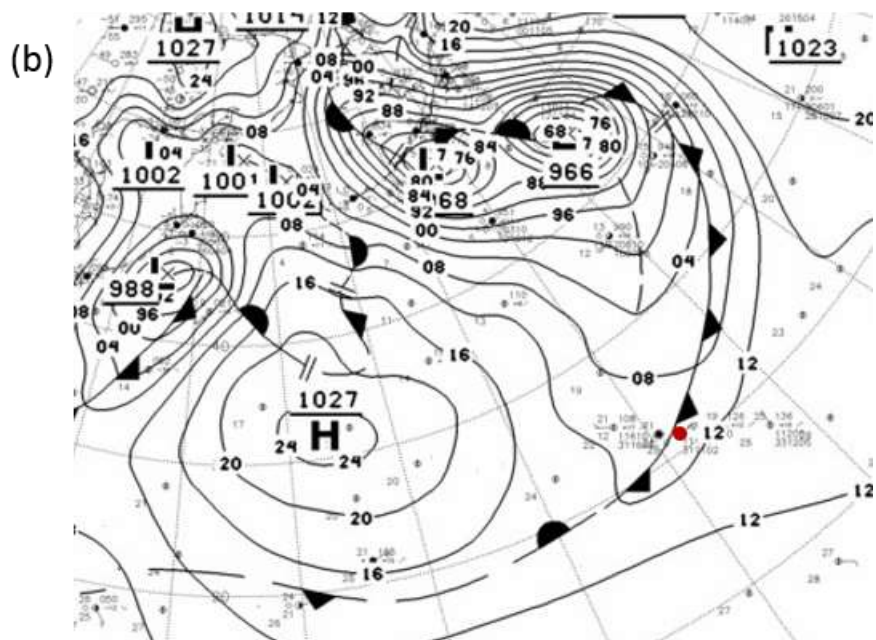
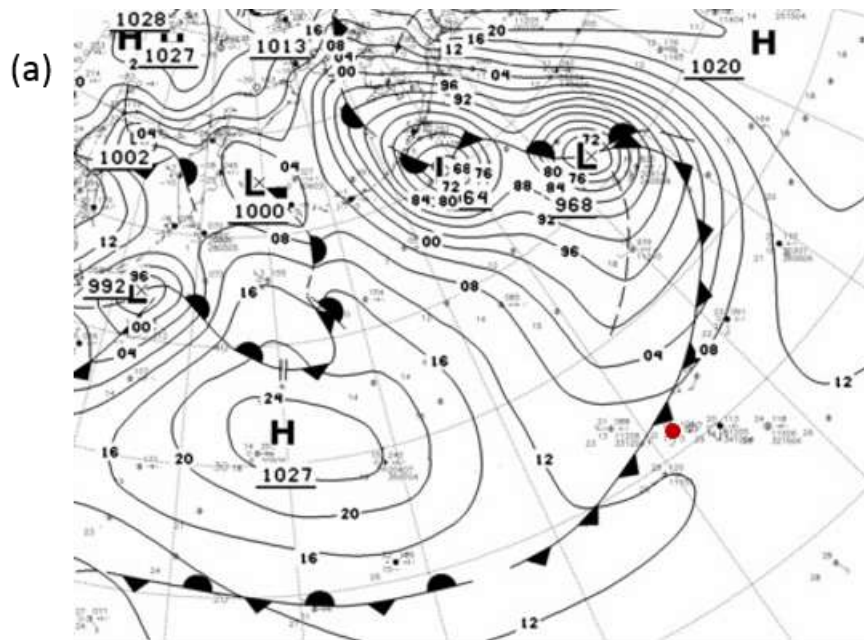
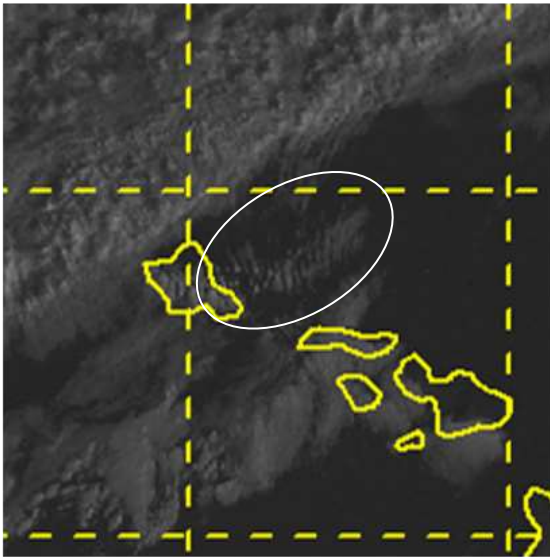
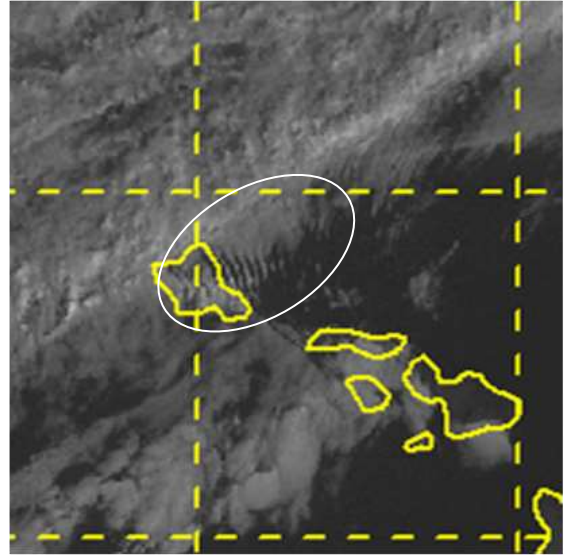


Figure 13. Surface maps from 26 Jan, 2014 trapped lee wave case in different stages: (a) before—1200 UTC, 26 January, 2014; (b) development—1800 UTC, 26 January, 2014; (c) after—0000 UTC, 27 January 2014. The red dot is the location of the island of O‘ahu. The unit of pressure is hPa.

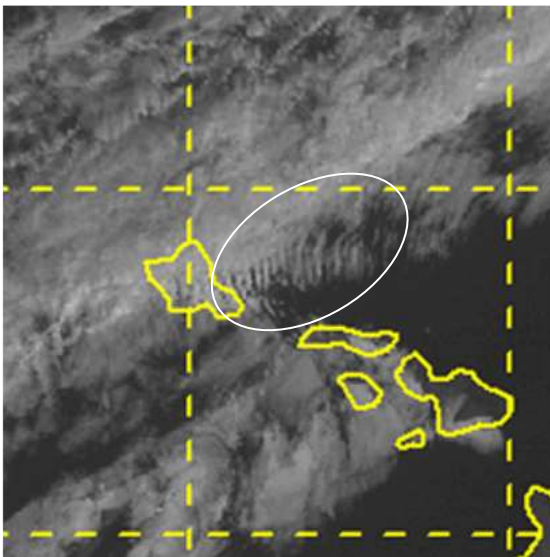
(a) 1800 UTC, 26 January, 2014



(b) 1900 UTC, 26 January, 2014



(c) 2000 UTC, 26 January, 2014



(d) 2200 UTC, 26 January, 2014

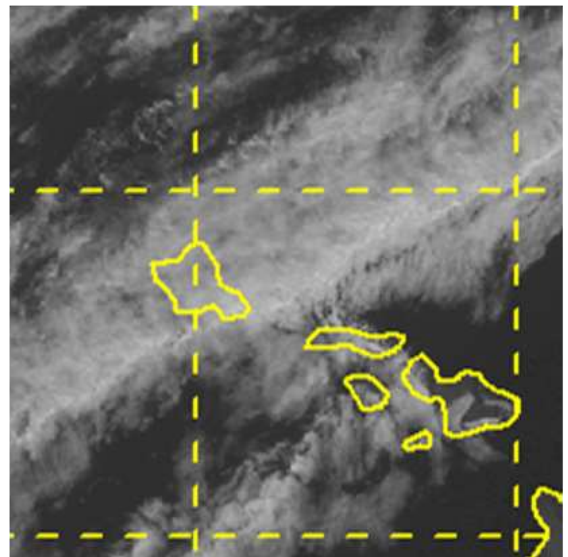


Figure 14. GOES-10 VIS Imagery in 1km resolution from Mauna Kea Weather Center (MKWC) at (a) 1800 UTC, 26 January, 2014; (b) 1900 UTC, 26 January, 2014; (c) 2000 UTC, 26 January, 2014; (d) 2200 UTC, 26 January, 2014.

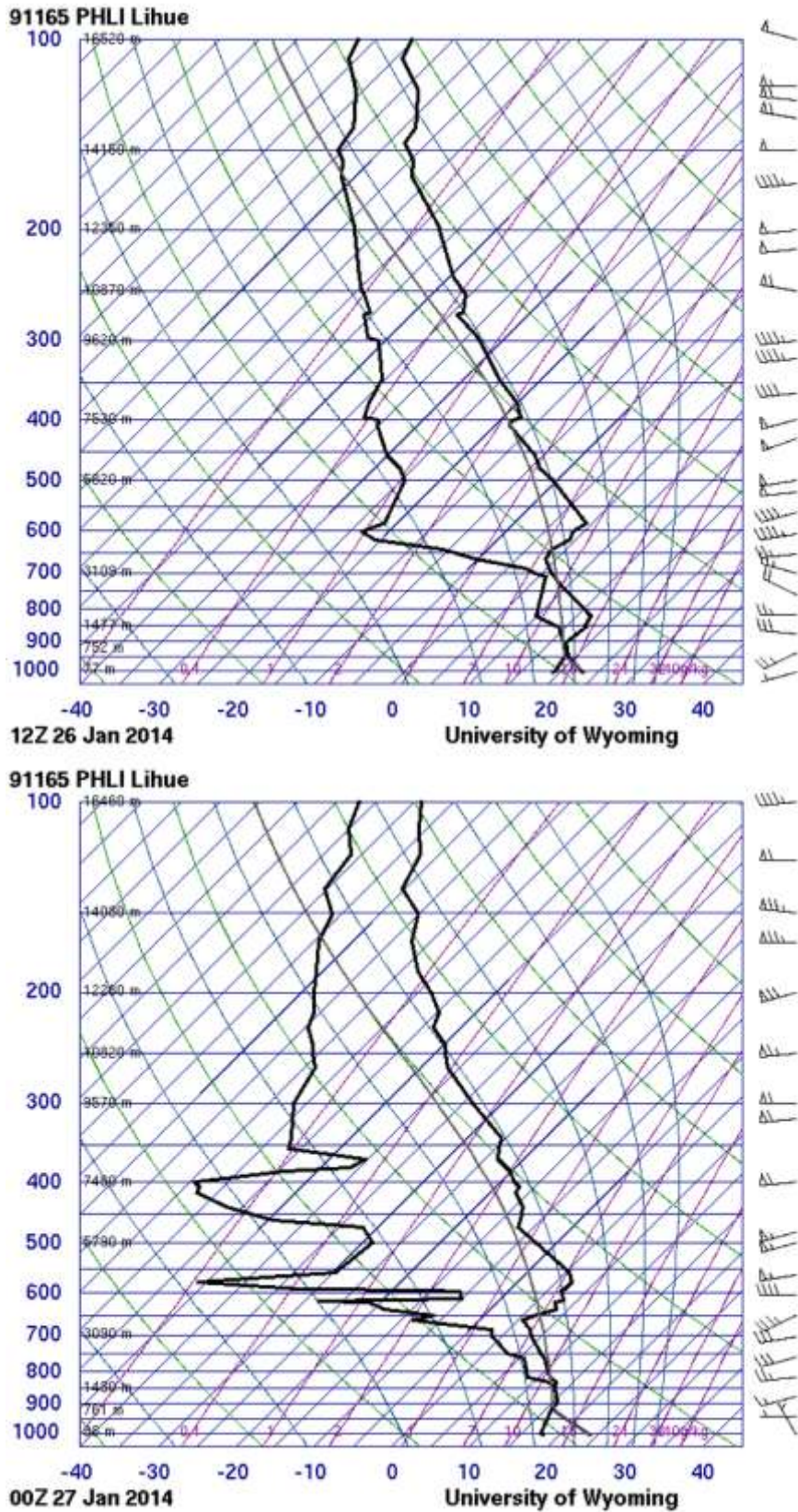


Figure 15. Skew T-log p soundings and vertical wind profiles from Lihue station at (left figure) 1200 UTC, 26 January, 2014; (right figure) 0000 UTC, 27 January, 2014.

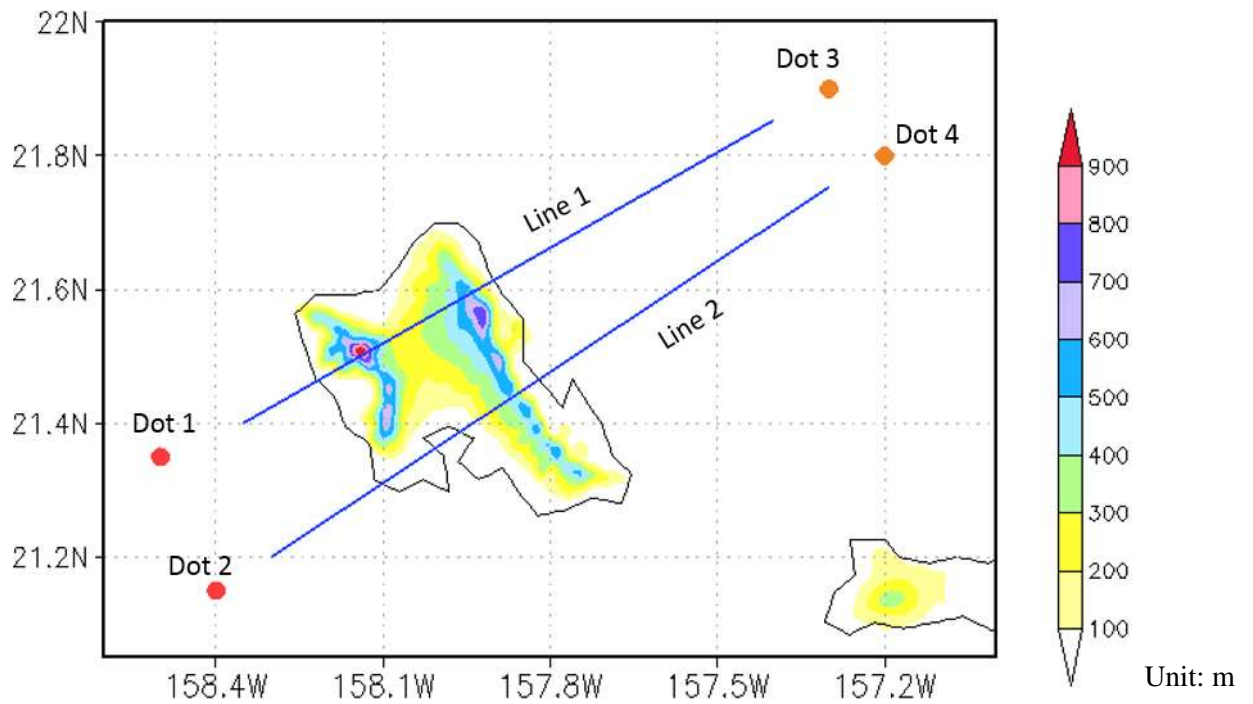


Figure 16. Shading is the terrain height (m) over O‘ahu. The detailed location for each dots are as follows: Dot 1 (21.35 °N, 158.5 °W); Dot 2 (21.15 °N, 158.4 °W); Dot 3(21.9 °N, 157.3 °W); and Dot 4 (21.8 °N, 157.2 °W). Line 1 is from (21.4 °N, 158.35 °W) to (21.85 °N, 157.4 °W); and line 2 is from (21.2 °N, 158.3 °W) to (21.75 °N, 157.3 °W). The unit of height is meters.

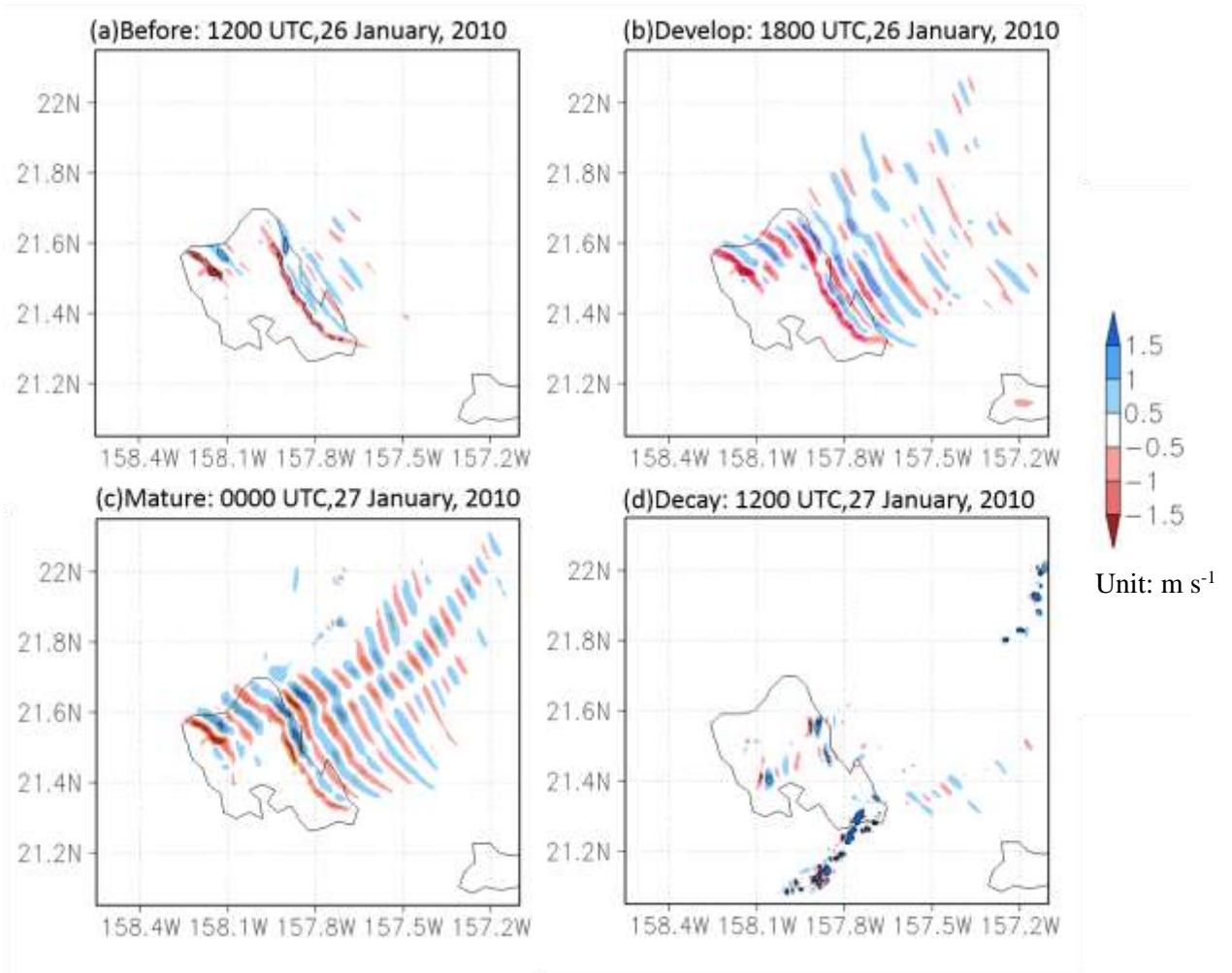


Figure 17. Model simulated vertical motion at 850 hPa for the trapped lee wave case of 26-27 January, 2010. The corresponding moment is (a) before: 1200 UTC, 26 January 2010; (b) develop: 1800 UTC, 26 January 2010; (c) mature: 0000 UTC, 27 January 2010; and (d) decay: 1200 UTC, 27 January 2010. The unit of vertical motion is m s^{-1} with upward motion being positive (blue).

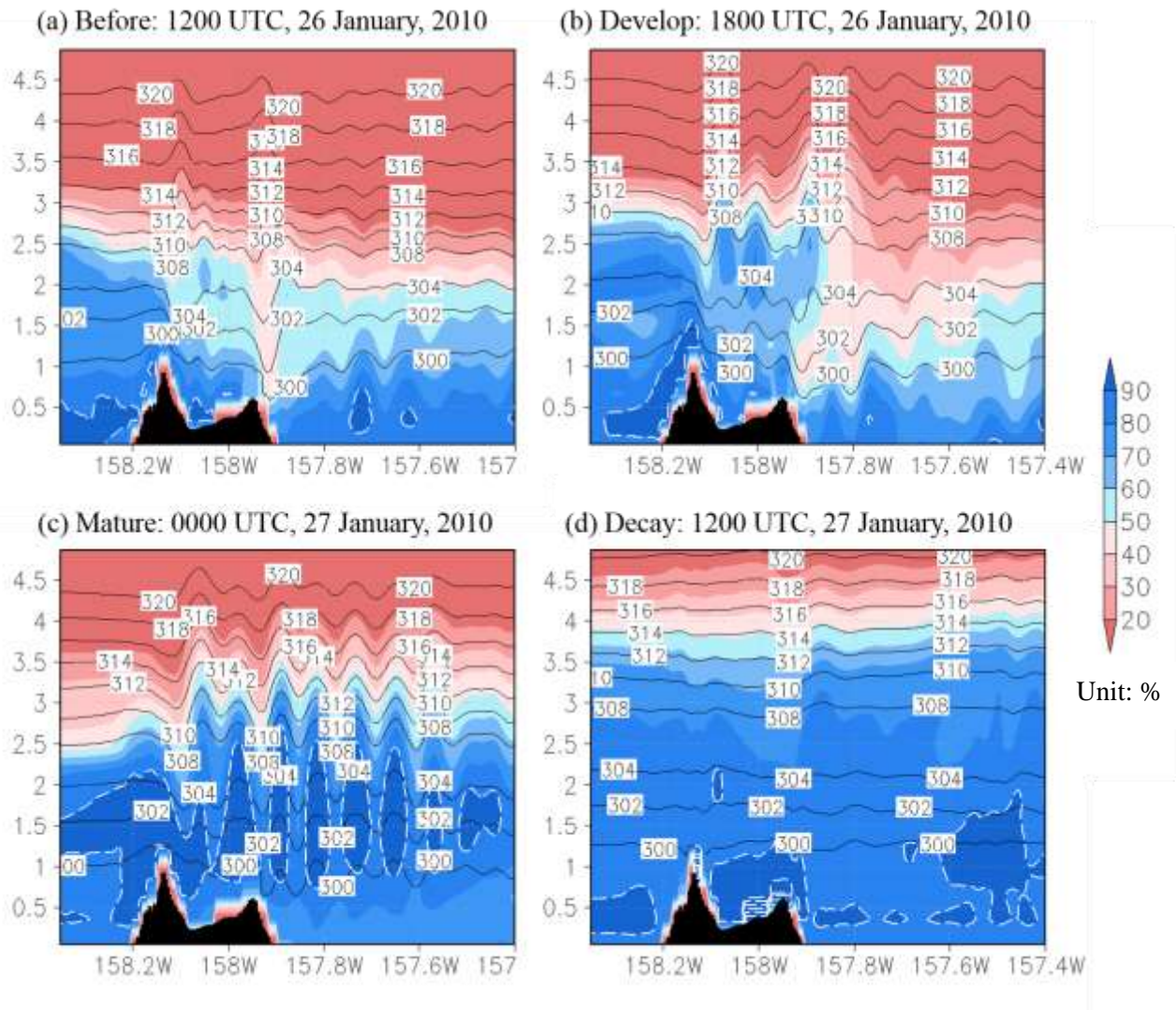


Figure 18. Equivalent potential temperature θ (contour) and relative humidity (shading) during the different phases of 27 January, 2010 trapped lee wave case. White dashed line is the area with relative humidity greater than 90%, where the clouds are very likely to occur. The unit of potential temperature is K and of relative humidity is %.

Dot 1

Dot 2

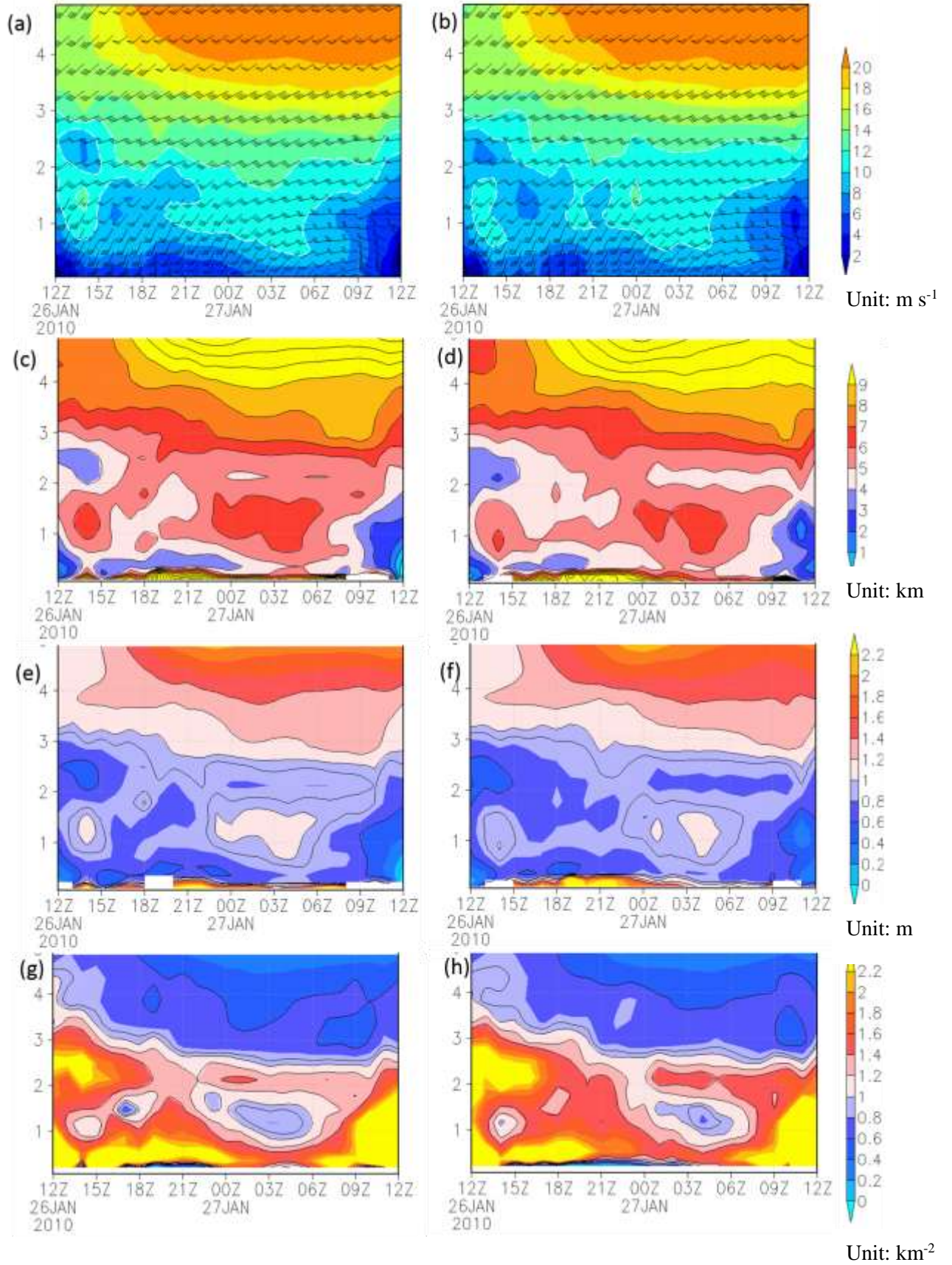


Figure 19. Time series of upstream airflow for the case on 26-27 Jan, 2010 on different properties: (a, b) upstream wind speed (contour) and horizontal wind vector (barb). One pennant, full barb, and half barb represent 20, 4, and 2 m s^{-1} , respectively; (c, d) wavelengths of buoyancy oscillations in the unit of km. (e, f) U/N , where U (m s^{-1}) is cross-barrier wind speed and N (s^{-1}) is static stability; (g, h) square of the Scorer parameter L^2 . Among them, figures in the left column (a, c, e, g) are upstream properties located at Dot 1 as shown in Figure 16, which suggest the upstream flow toward Wai‘anae and Ko‘olau; Figures in the right column (b, d, f, h) are upstream properties located at Dot 2, which is more southeasterly and depict the upstream flow towards Ko‘olau Mountain solely.

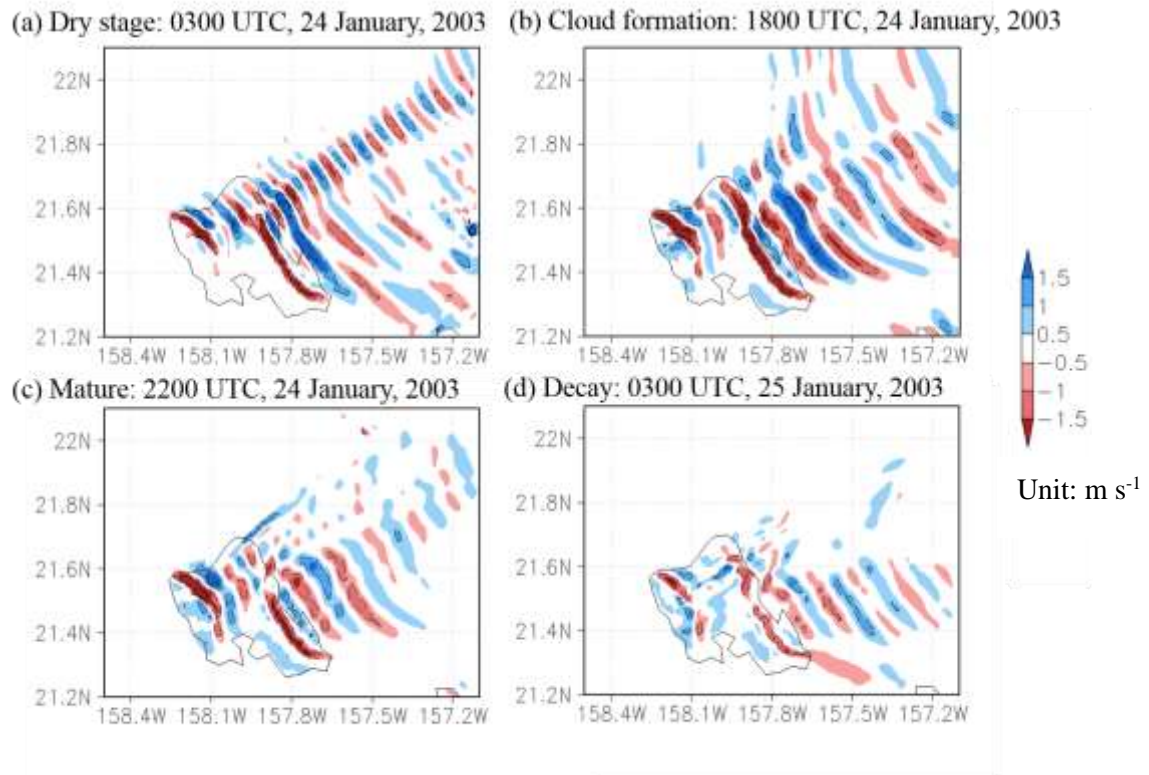


Figure 20. Model simulated vertical motion at 850 hPa for the trapped lee wave case of 24-25 January, 2003. The corresponding moment is (a) 0300 UTC, 24 January, 2003, (b) 1800 UTC, 24 January 2003; (c) 1800 UTC, 24 January 2003; (d) 0300 UTC, 25 January 2003. The unit of vertical motion is m s^{-1} with upward motion being positive.

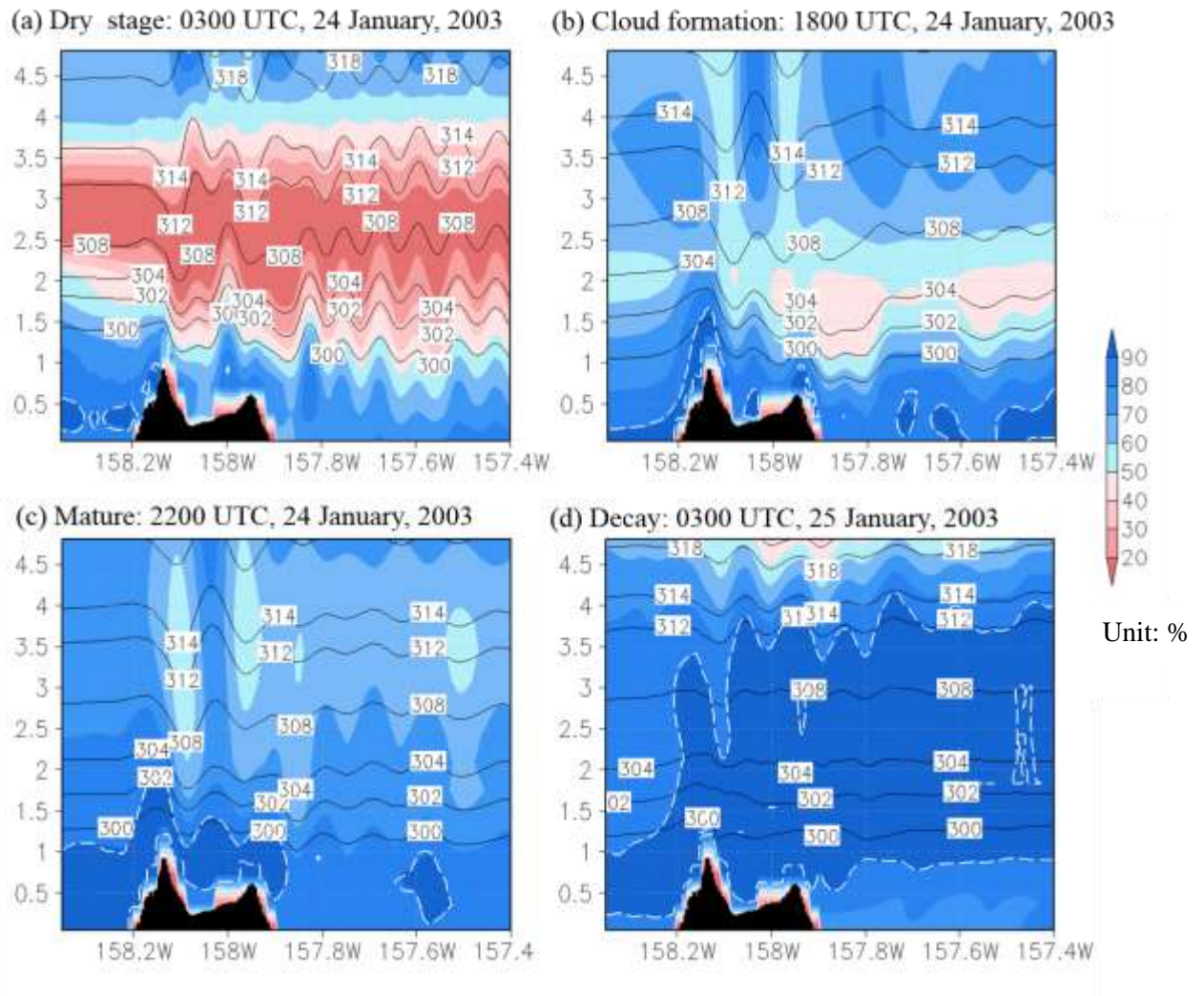


Figure 21. Equivalent potential temperature θ (contour) and relative humidity (shading) during the different phases of 24-25 January, 2003 trapped lee wave case. White dashed line outlines the area with relative humidity greater than 90%, where the clouds are very likely to occur.

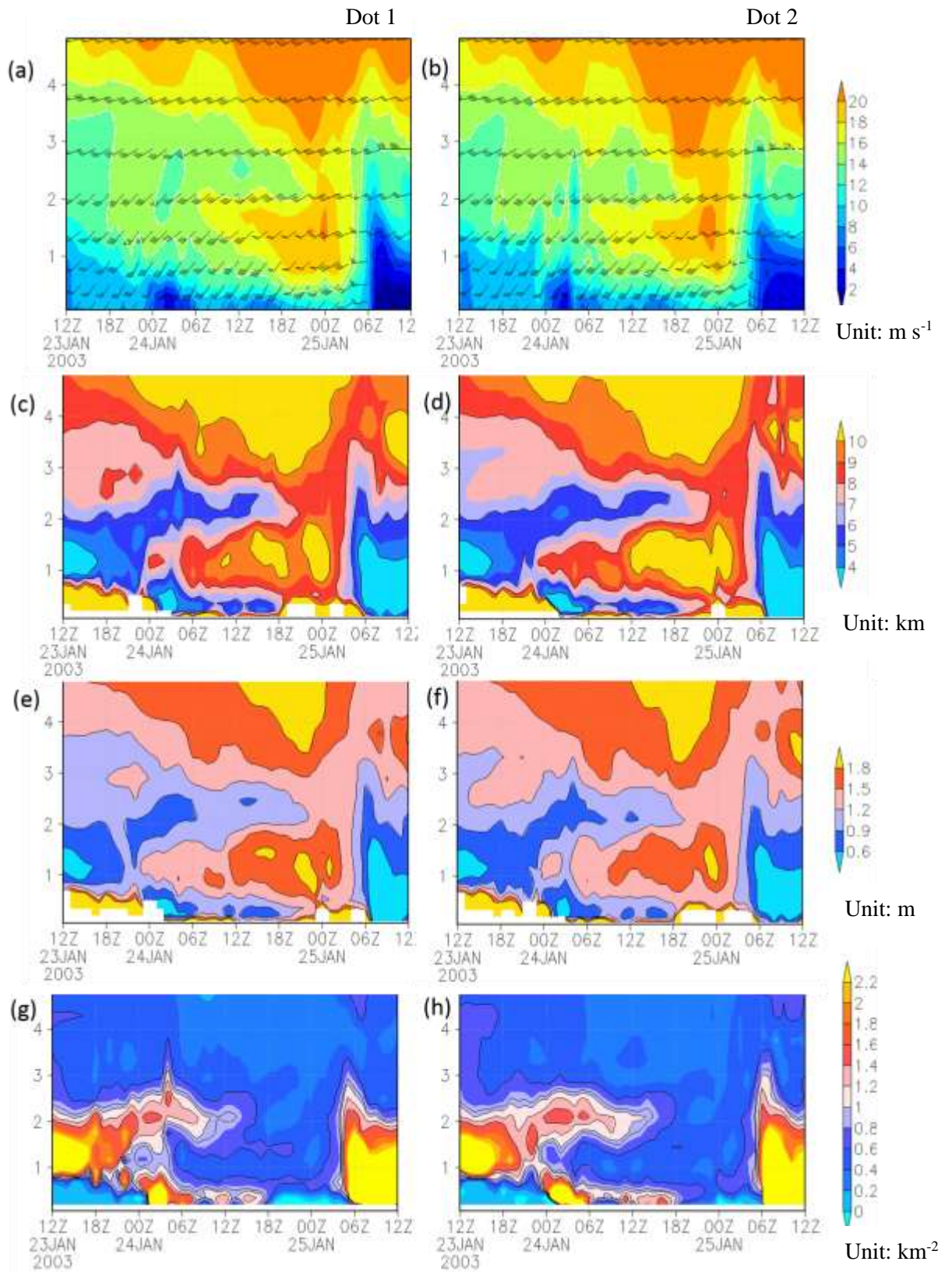


Figure 22. Time series of upstream airflow for the case on 24-25 Jan, 2003 on different properties: (a, b) upstream wind speed (contour) and horizontal wind vector (barb). One pennant, full barb, and half barb represent 20 , 4 , and 2 m s^{-1} , respectively; (c, d)

wavelengths of buoyancy oscillations in the unit of km. (e, f) U/N , where U (m s^{-1}) is cross-barrier wind speed and N (s^{-1}) is static stability; (g, h) square of the Scorer parameter L^2 . Figures in the left column (a, c, e, and g) are upstream properties located at Dot 1; Figures in the right column (b, d, f, h) are upstream properties located at Dot 2.

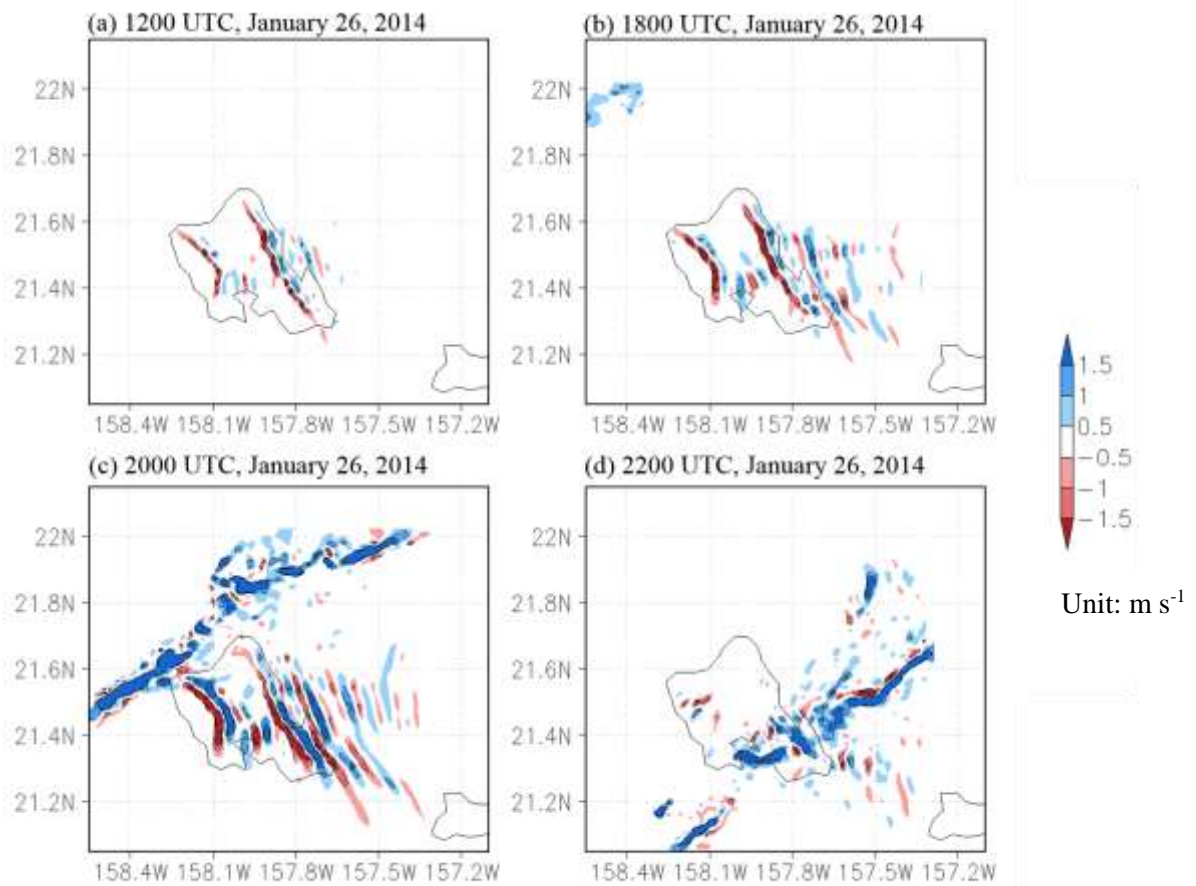


Figure 23. Model simulated vertical motion at 850 hPa for the trapped lee wave case of 26 January 2014. The corresponding moment is (a) before: 1200 UTC, 26 January 2014; (b) developing: 1800 UTC, 26 January 2014; (c) mature: 2000 UTC, 26 January 2014, (d) decay: 2200 UTC, 26 January 2014. The unit of vertical motion is m s^{-1} with upward motion being positive.

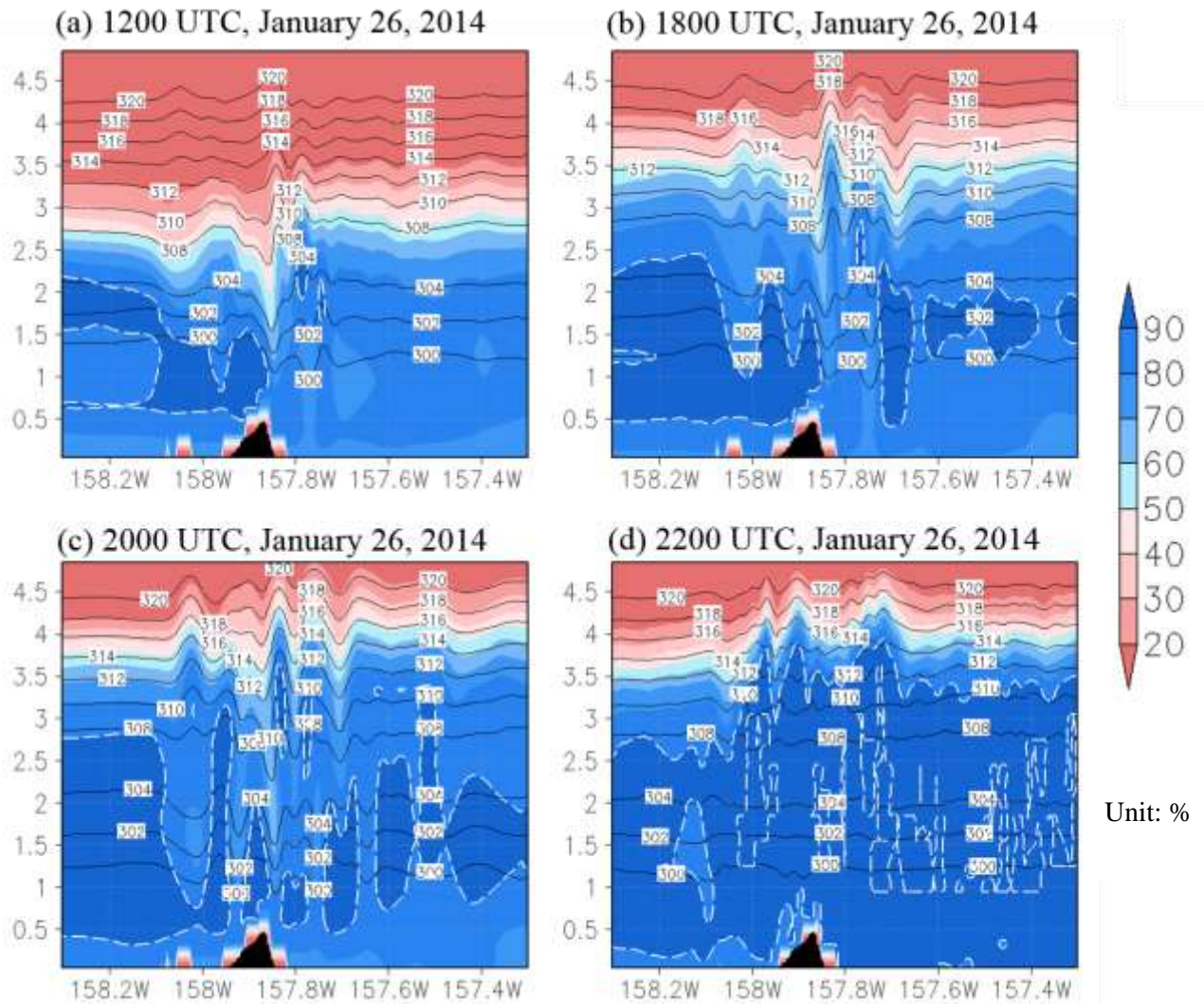


Figure 24. Equivalent potential temperature θ (contour) and relative humidity (shading) during the different phase of 26 January, 2014 trapped lee wave case. White dashed line outlines the area with relative humidity greater than 90%, where the clouds are very likely to occur.

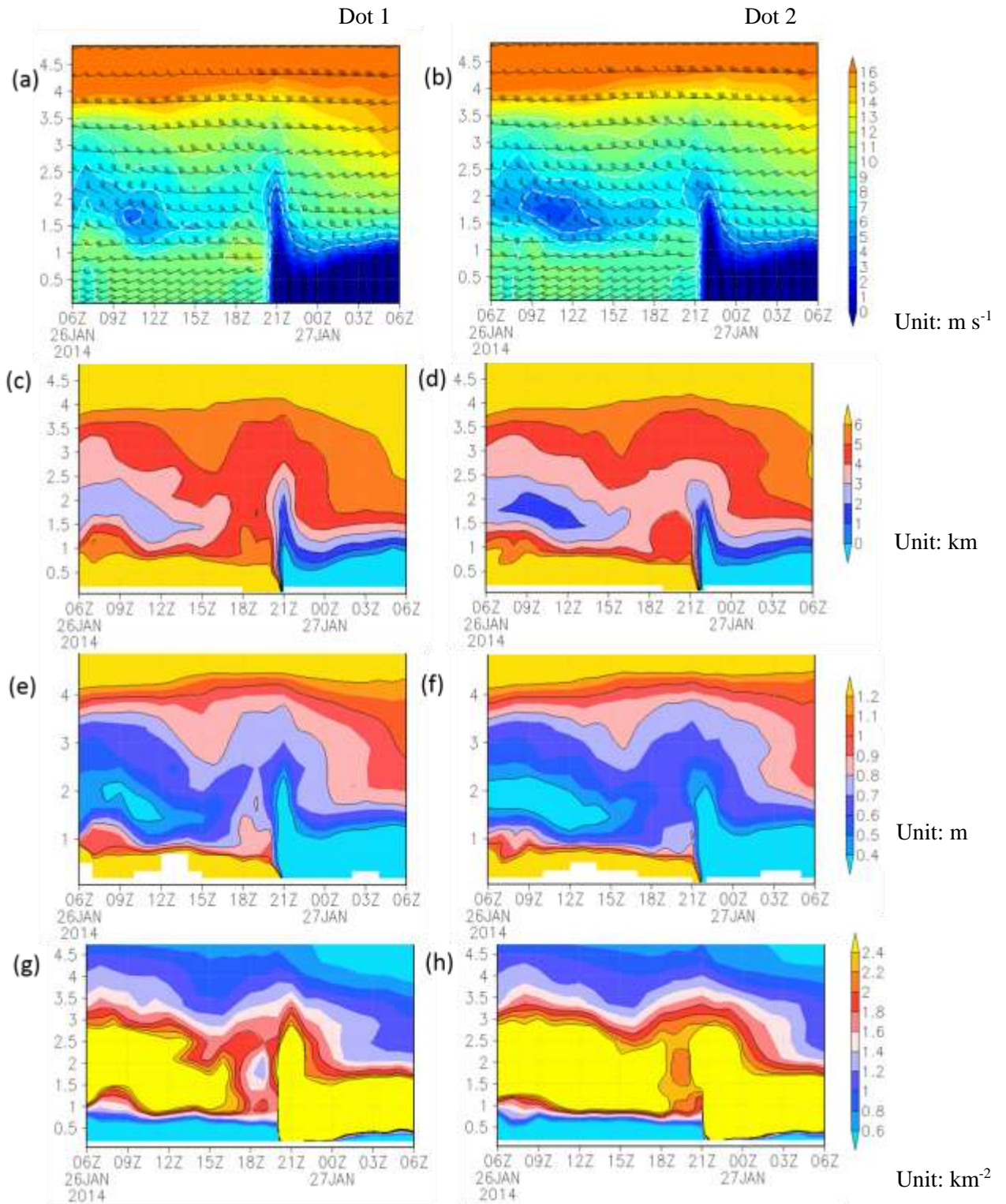


Figure 25. Time series of upstream airflow for the 26 Jan, 2014 case on different properties: (a, b) upstream wind speed (contour) and horizontal wind vector (barb). One pennant, full barb, and half barb represent 20, 4, and 2 m s^{-1} , respectively; (c, d) wavelengths of buoyancy oscillations in the unit of km. (e, f) U/N , where U (m s^{-1}) is cross-barrier wind speed and N (s^{-1}) is static stability; (g, h) square of the Scorer

parameter L^2 . Figures in the left column (a, c, e, g) are upstream properties located at Dot 1; Figures in the right column (b, d, f, h) are upstream properties located at Dot 2.

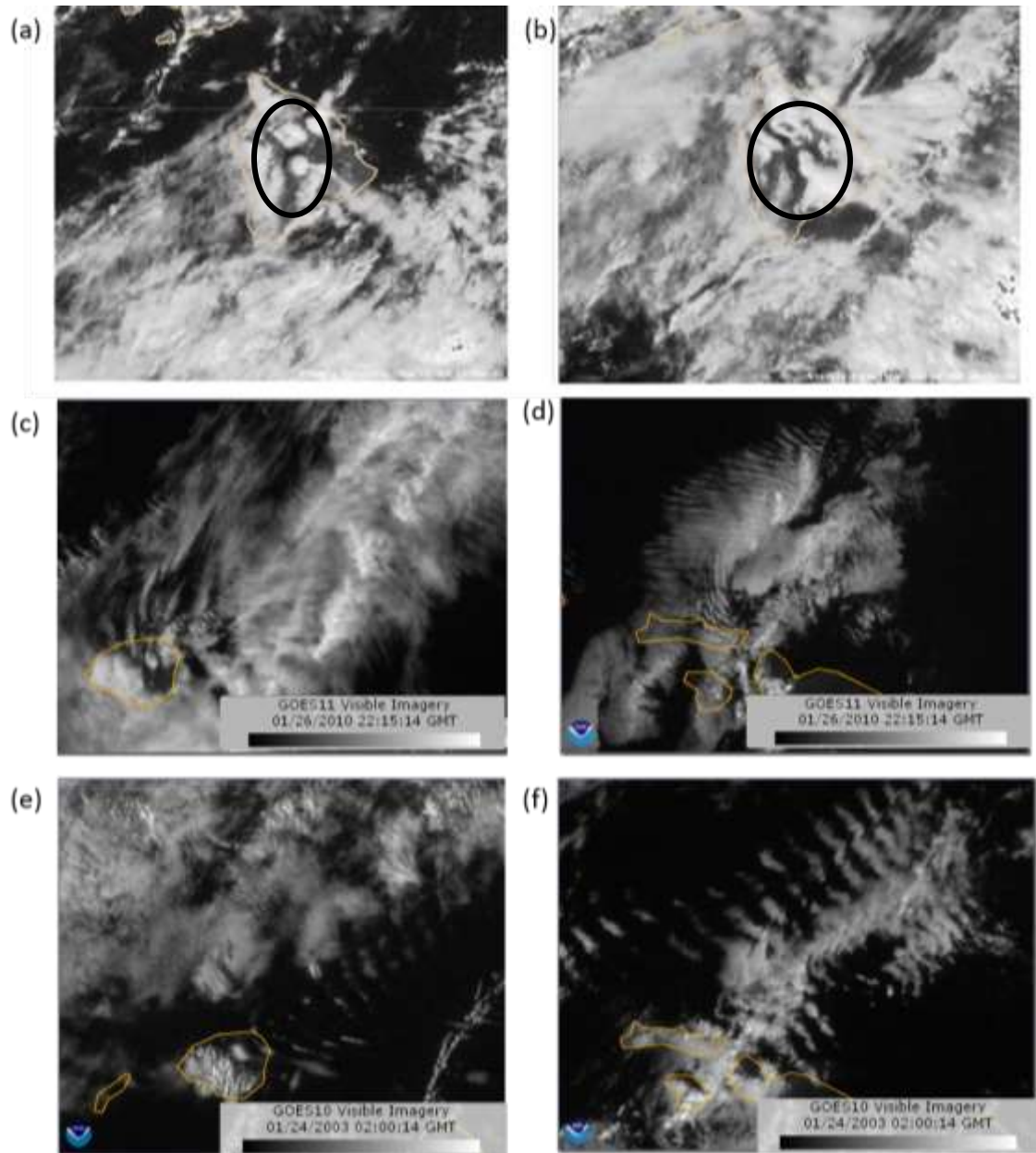


Figure 26. Trapped lee waves over other Hawaiian Islands. Upper-level lenticular clouds over Big Island at (a) 2000 UTC, November 25, 2003 and (b) 0000 UTC, November 26. In January 26, 2010 (TRAP1), the trapped lee wave clouds to the (c) northeast Kaua‘i at 2215 UTC and (d) lee side of Moloka‘i at 1900 UTC; In 24 January, 2003 (TRAP2), the trapped lee wave clouds observed to the northeast of (e) Kaua‘i at 0200 UTC and (f) Moloka‘i and western Maui at 2030 UTC.

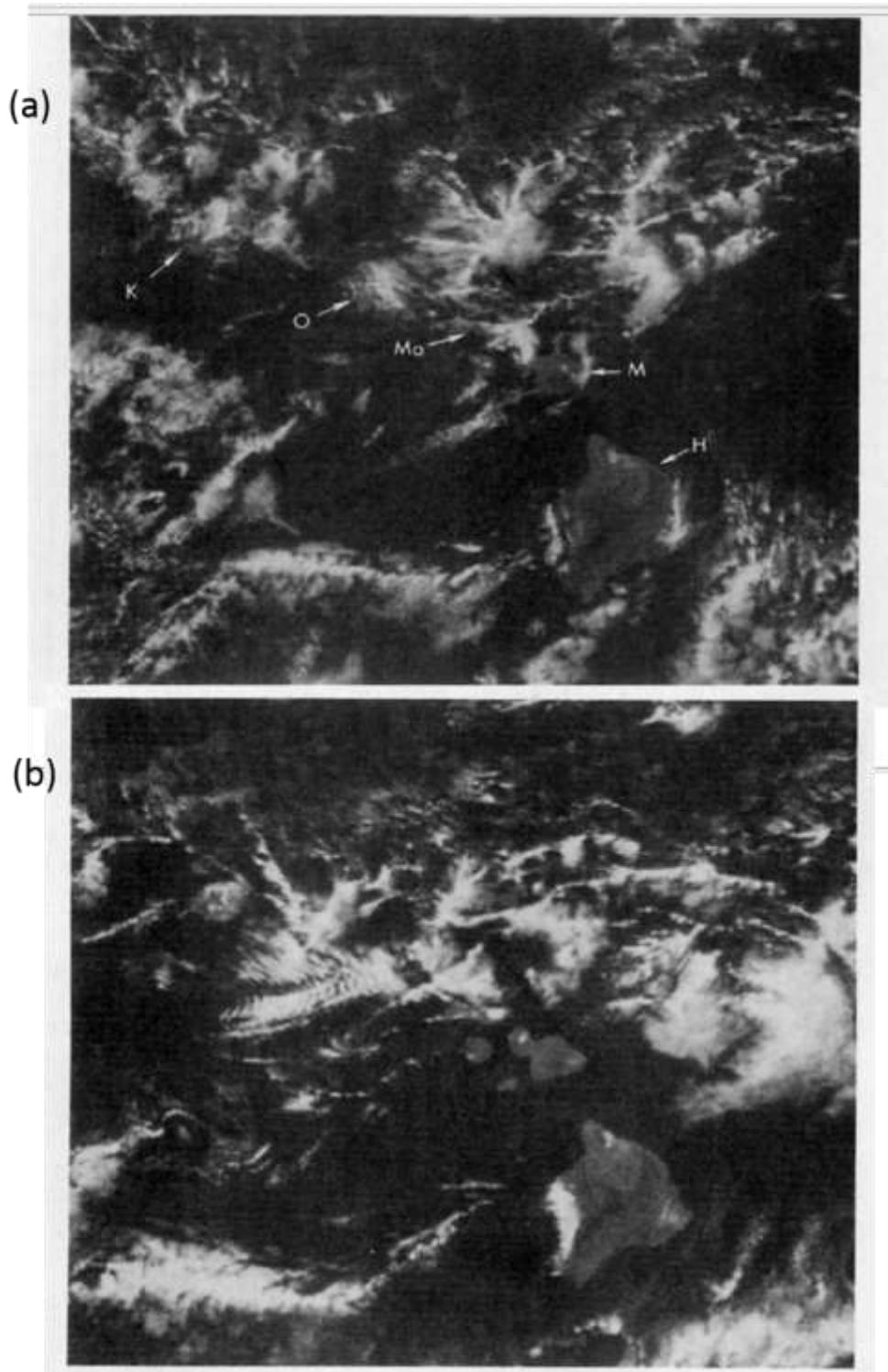


Figure 27. SMS-2 1 km VIS image for the trapped lee wave case in 25 August, 1977. The corresponding moment is (a) 1845 UTC, 25 August, 1977 and (b) 2145 UTC, 25 August, 1977. K—Kaua'i, O--O'ahu, Mo--Moloka'i, M--Maui and H--Hawai'i.

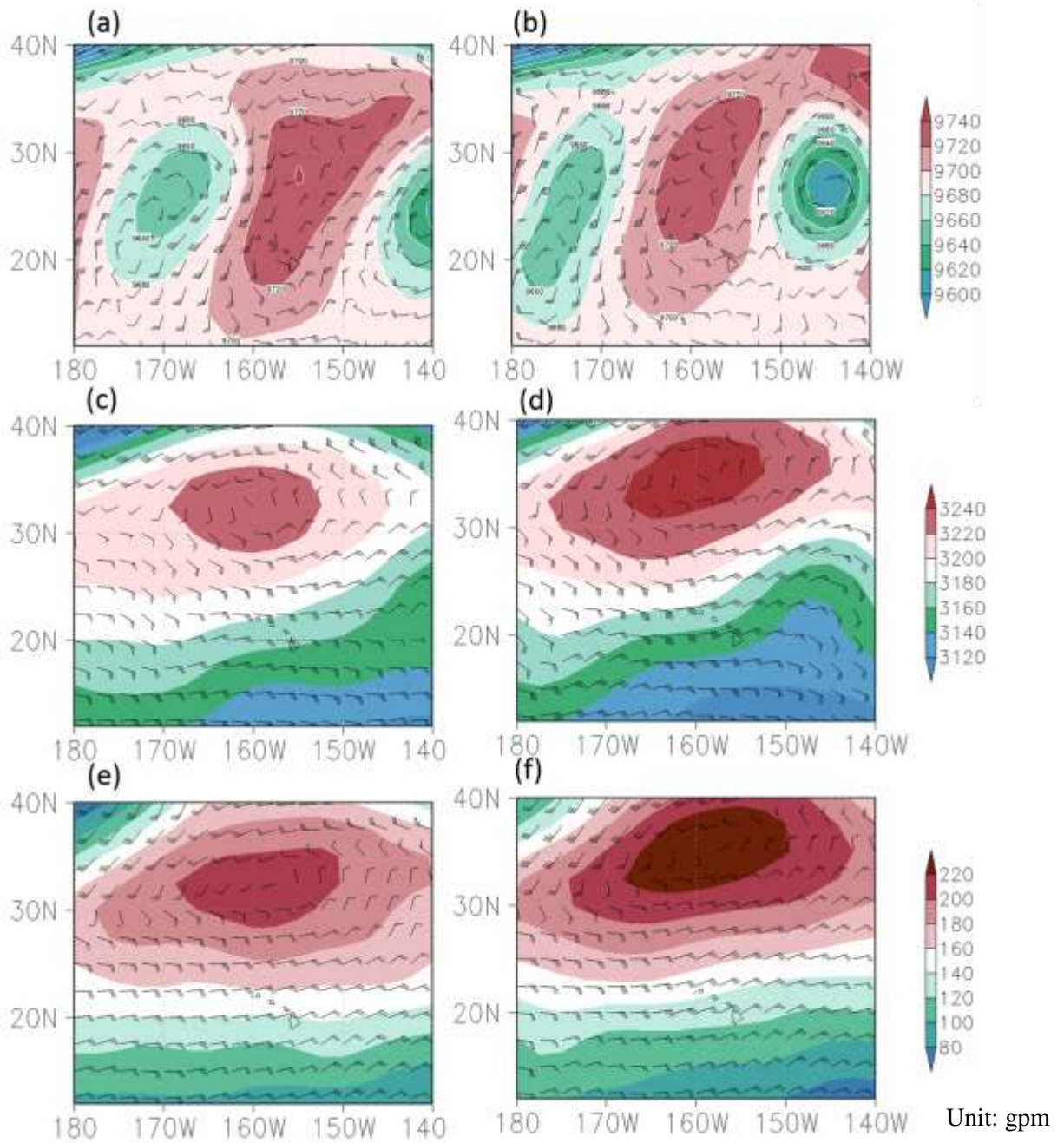
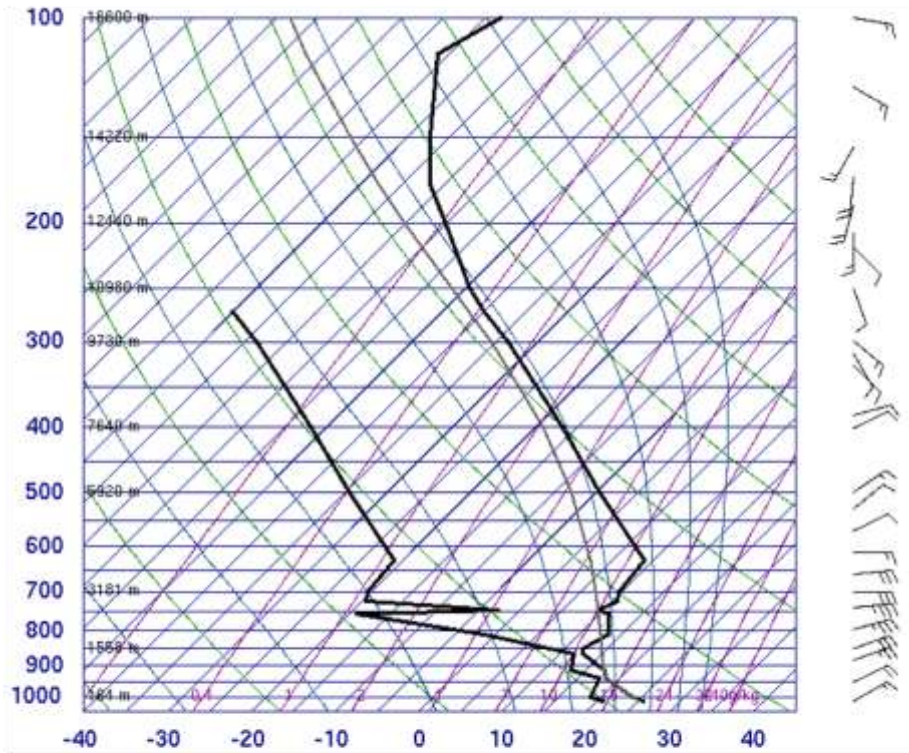


Figure 28. Geo-potential height (shading) and wind pattern (barb) in low, middle and upper level before and during the development of the trapped lee wave case on 25 August, 1977. (a), (b), (c) is at 0000 UTC, 25 August, 1977 in 300 hPa, 700 hPa and 1000 hPa, respectively; (d), (e), (f) is at 0000 UTC, 26 August, 1977 in 300 hPa, 700 hPa and 1000 hPa, respectively; One pennant, full barb and half barb represent 20, 4 and 2 m s^{-1} , respectively.

(a) 1200 UTC, 25 August, 1977



(b) 0000 UTC, 26 August, 1977

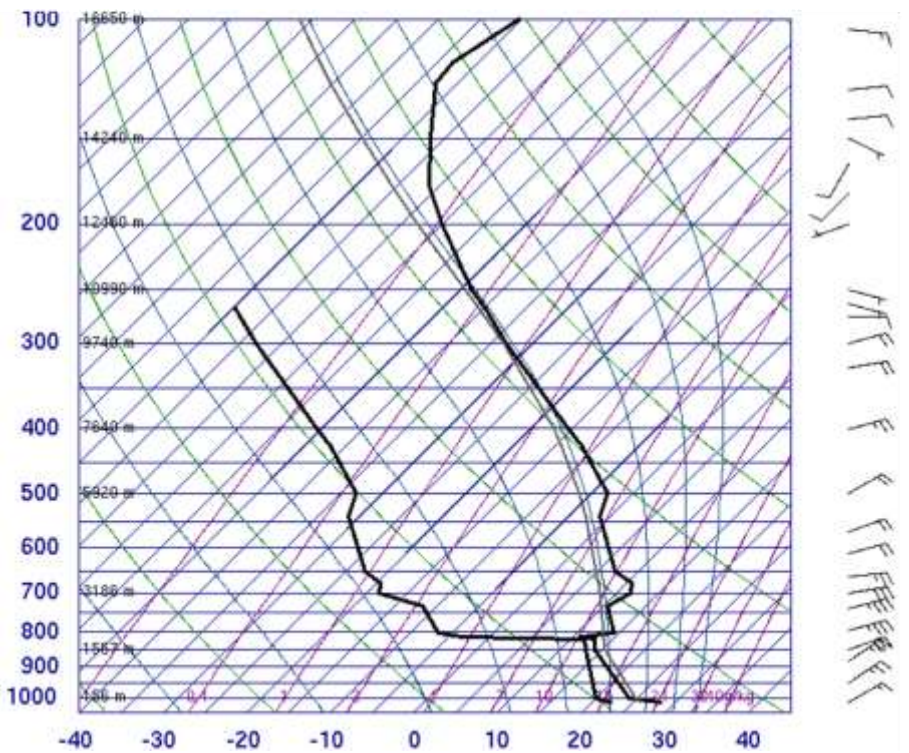


Figure 29. Skew T-log p soundings and vertical wind profiles from Lihue station at (a) 1200 UTC, 25 August 1977 and (b) 0000 UTC, 26 August 1977. Data is from University of Wyoming.

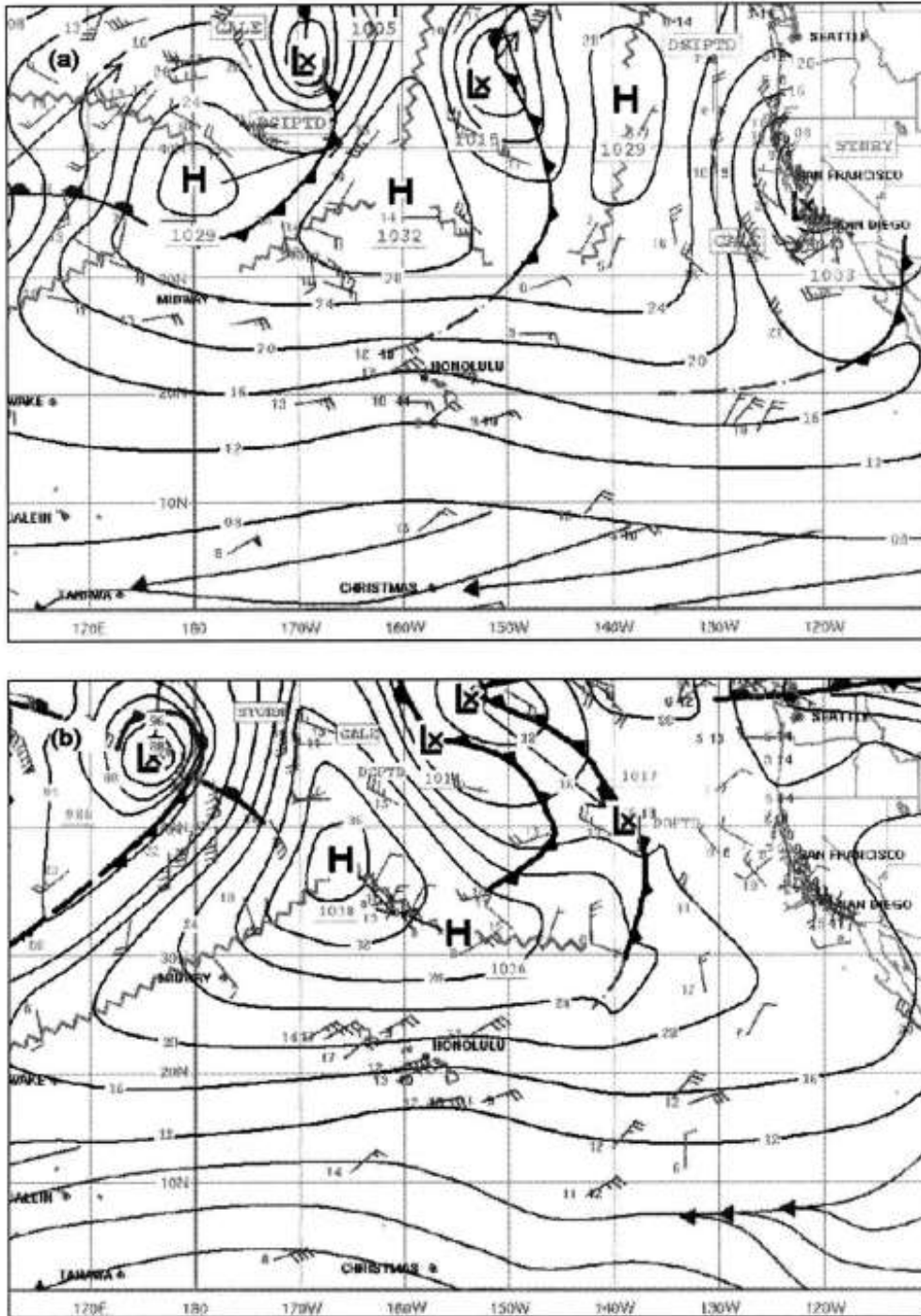


Figure 30. Surface analyses for 0000 UTC on (a) 13 and (b) 14 February 2001 (adapted from the subjective analyzes by forecaster at the NWS Forecast Office in Honolulu). Isobars are every 4 hPa. (From Yongxin's paper)

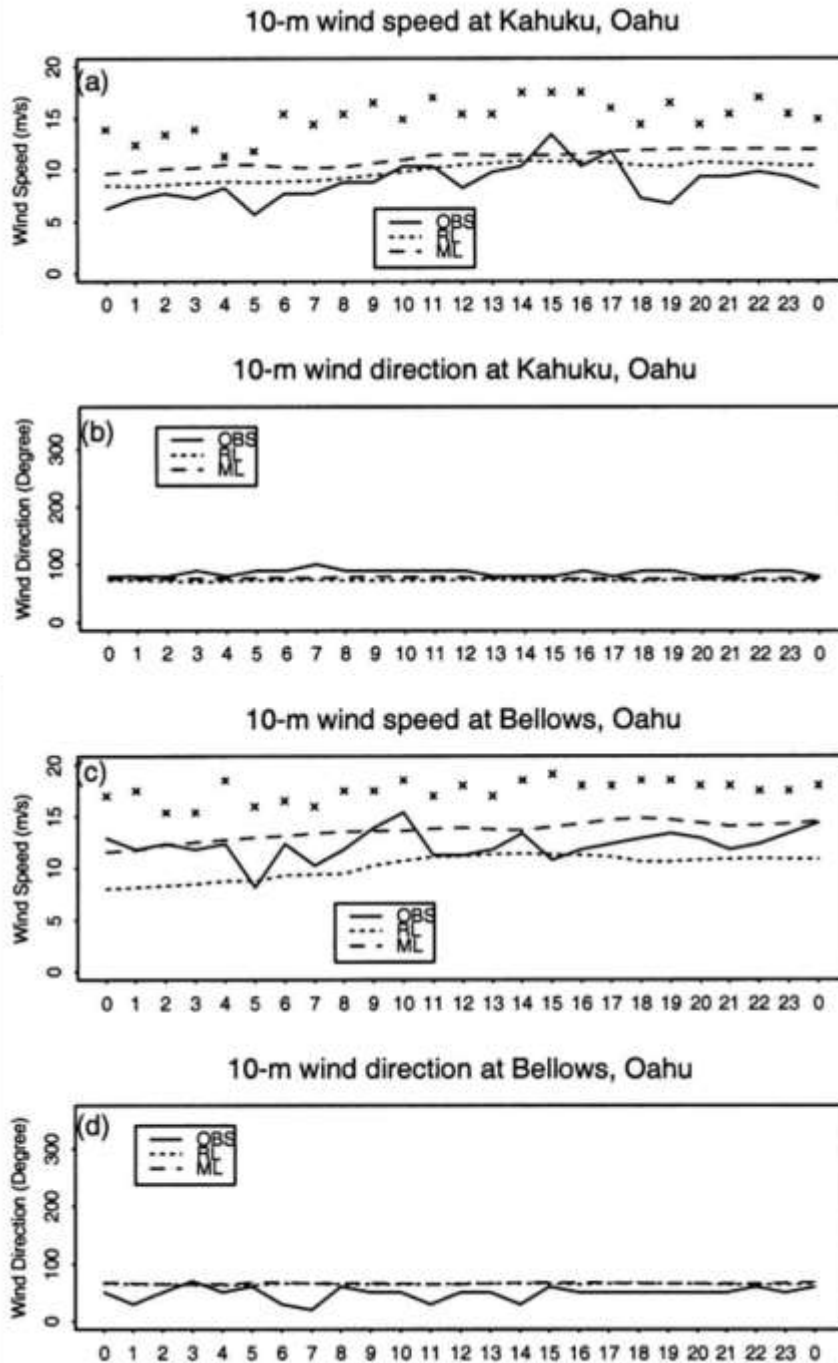


Figure 31. Observed, and RSM-LSM and MSM-LSM simulated 10m (left) wind speeds (m s^{-1}) and (right) wind direction at Kahuku, O‘ahu and Bellows O‘ahu. During the period of 1000 UTC, 14 February—1000 UTC, 15 February 2001. Solid, dotted, and dashed lines refer to the observations, RSM-LSM, and MSM-LSM simulations, respectively. Stars indicate the magnitudes of reported wind gusts (m s^{-1}). Refer to Figures 1a and 1c for the locations of these surface sites. (From Yongxin Zhang’s paper)

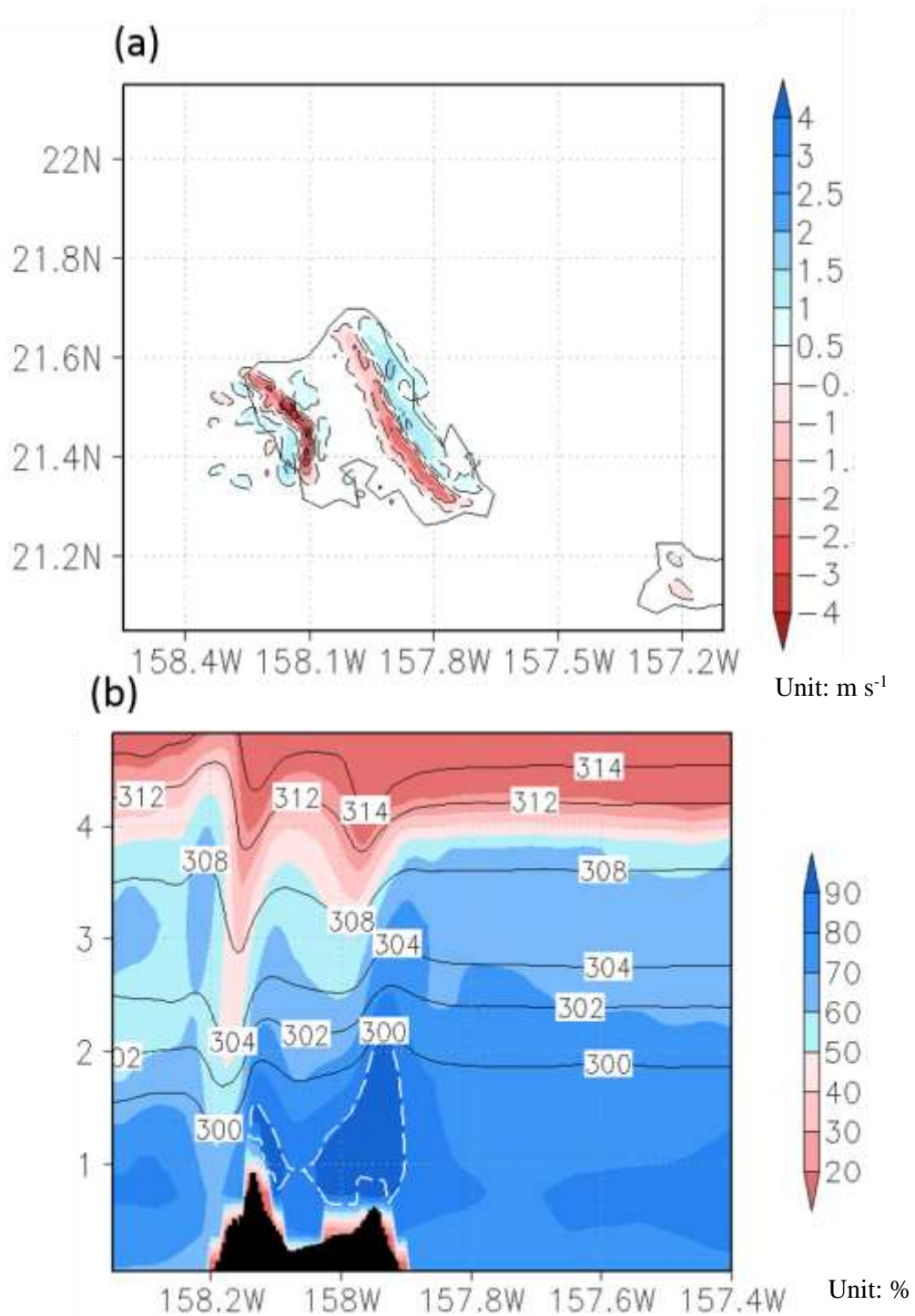


Figure 33. Model simulated vertical motion in 850 hPa for the mountain wave case on 01 August, 2001. The corresponding moment is 0100 UTC, 15 February 2001. The unit of vertical motion is m s^{-1} with upward motion being positive.

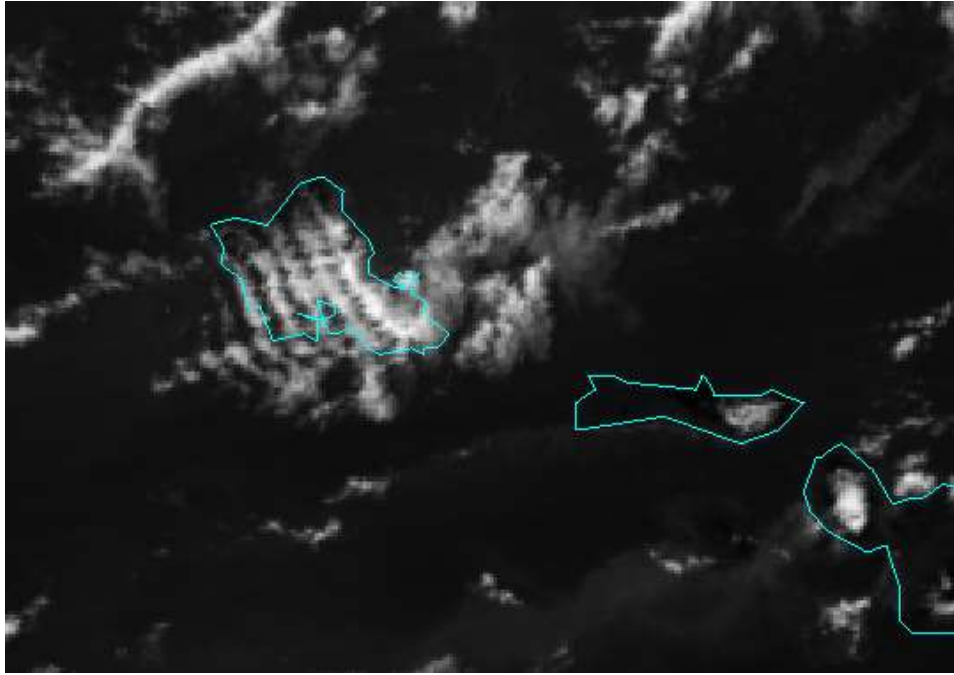


Figure 34. MODIS satellite image at 2337 UTC, 31 July, 2013 over the island of O‘ahu.

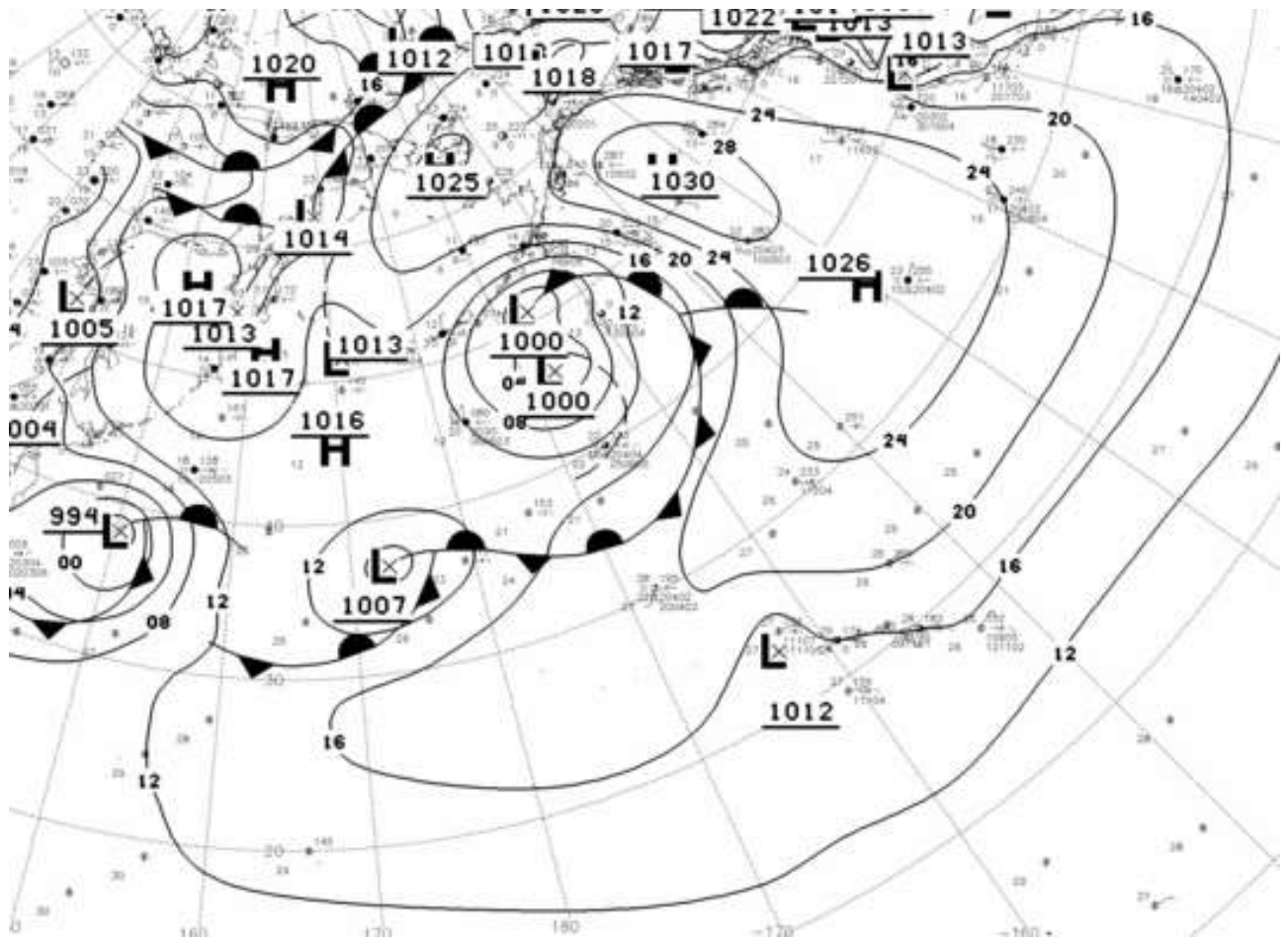


Figure 35. Surface analyses for 1800 UTC on 30 July, 2013 (from the subjective analyzes by forecaster at the NWS Forecast Office in Honolulu). Isobars are every 4 hPa.

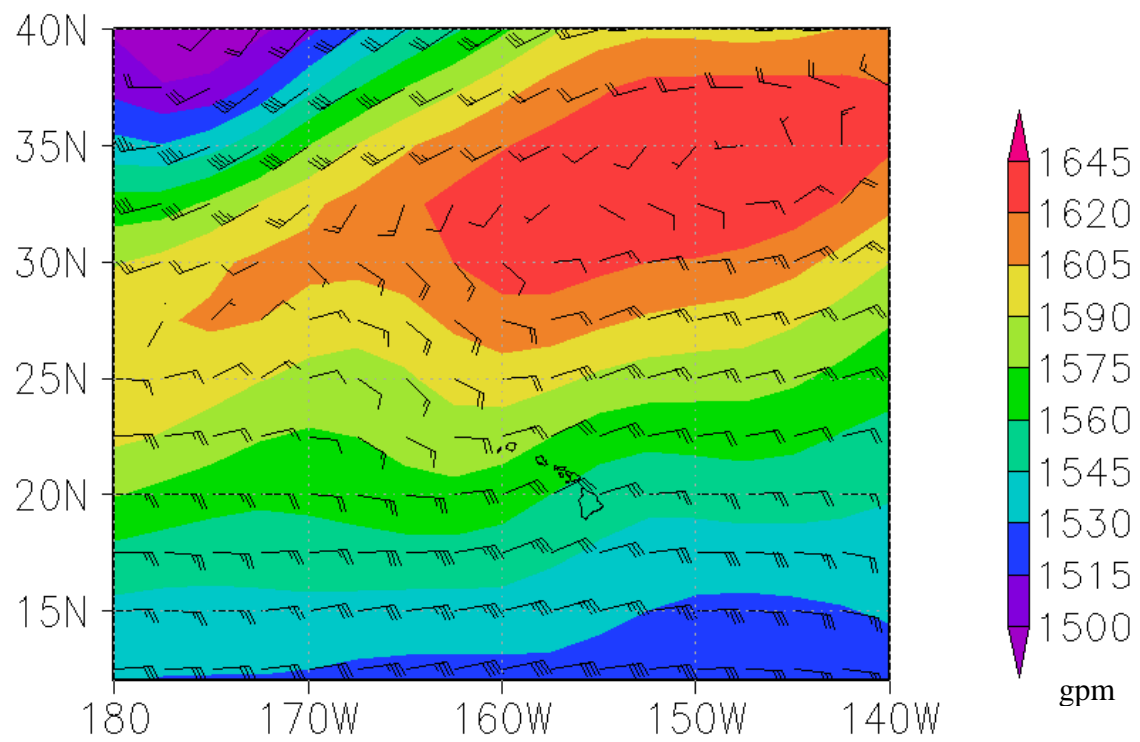


Figure 36. Geopotential height in the unit of gpm (shading) and horizontal wind barbs at 850 hPa over the Hawaiian Islands at 0000 UTC, 1 August, 2013.

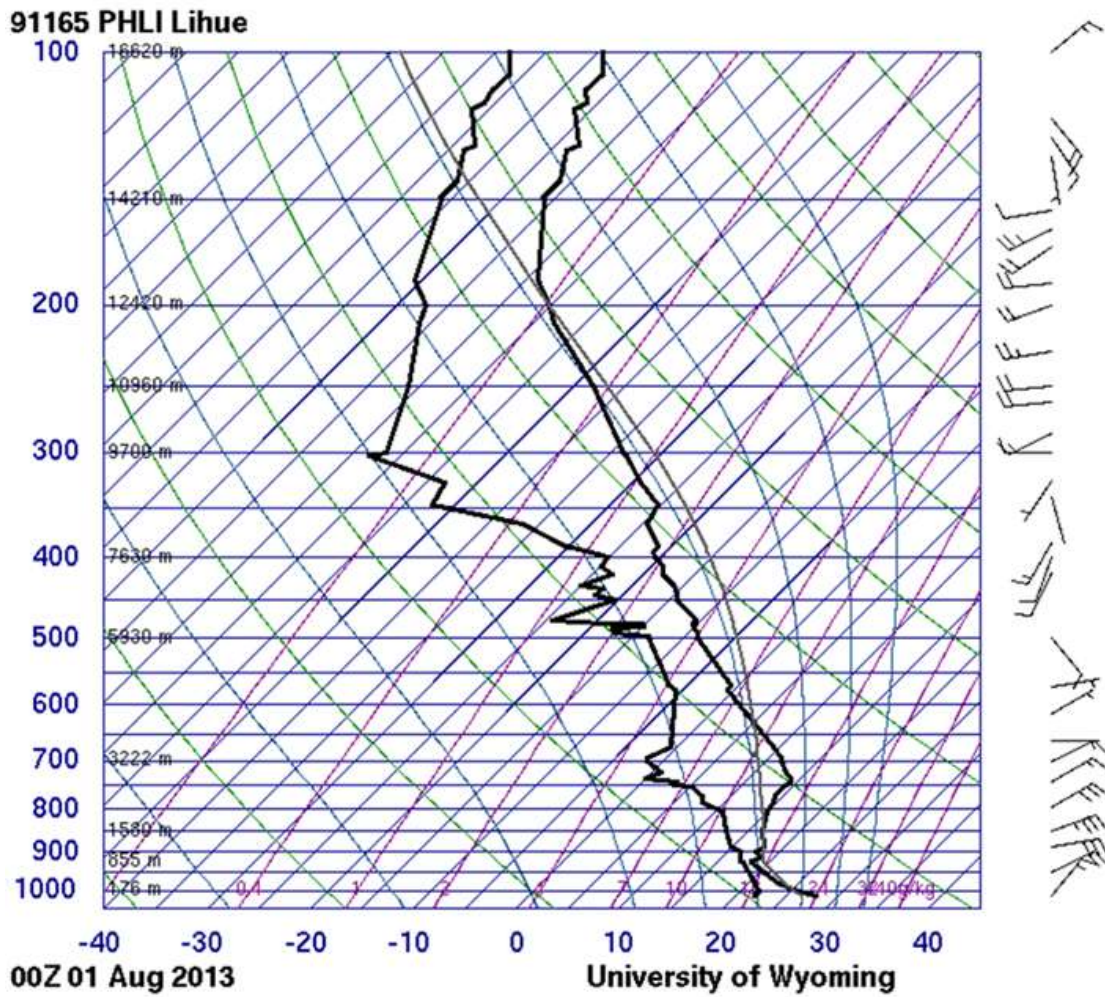


Figure 37. Skew-T chart (courtesy of the Department of Atmospheric Science, University of Wyoming; <http://weather.uwyo.edu/upperair/sounding.html>) for Lihue, Kaua'i at 0000 UTC, 01 August, 2013.

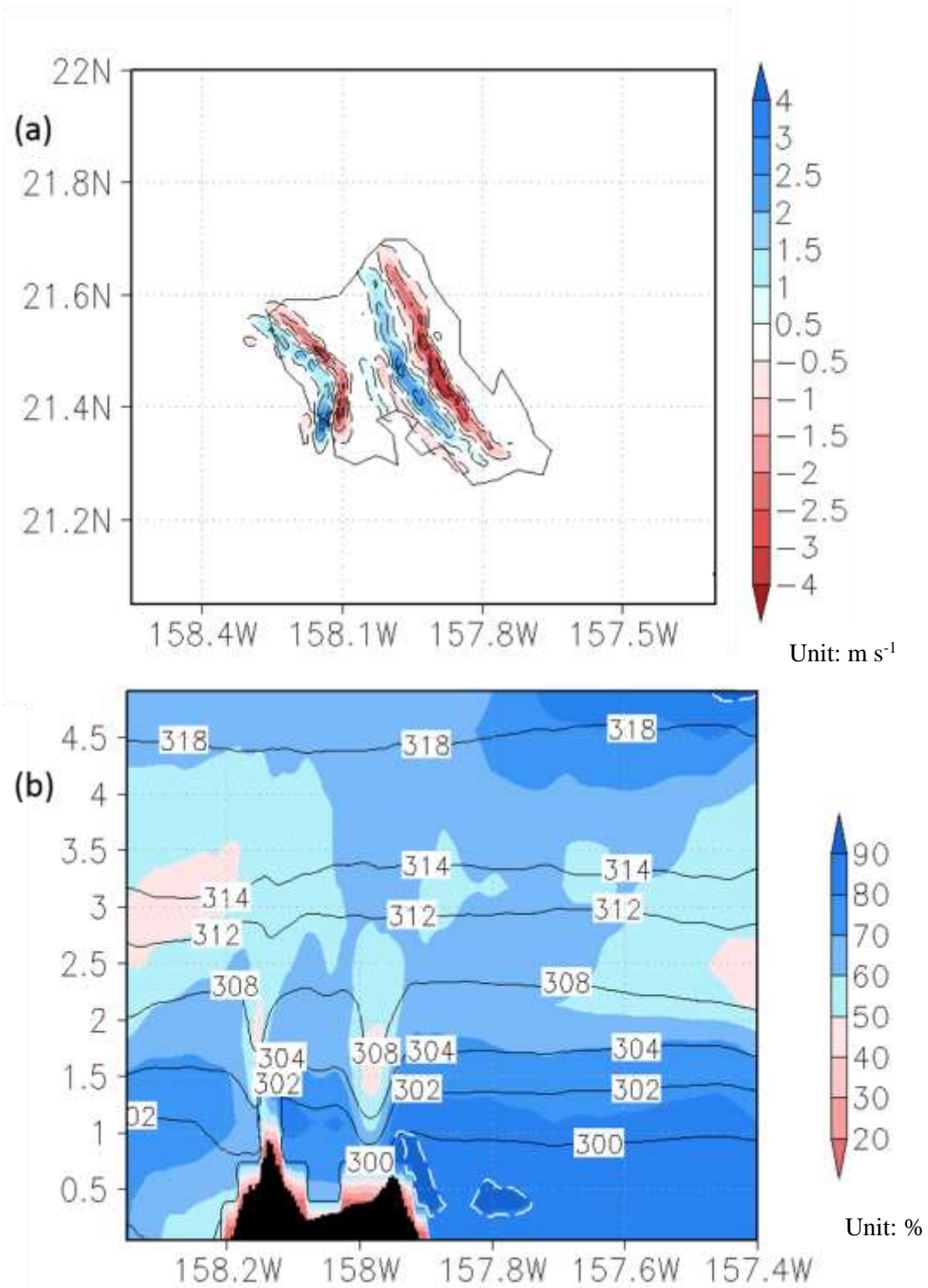


Figure 38. Model simulated (a) vertical motion at 850 hPa, (b) relative humidity and potential temperature for the mountain wave case on 01 August, 2013. The corresponding moment is 0000 UTC, 01 August 2013. The unit of vertical motion is m s^{-1} with upward motion being positive.

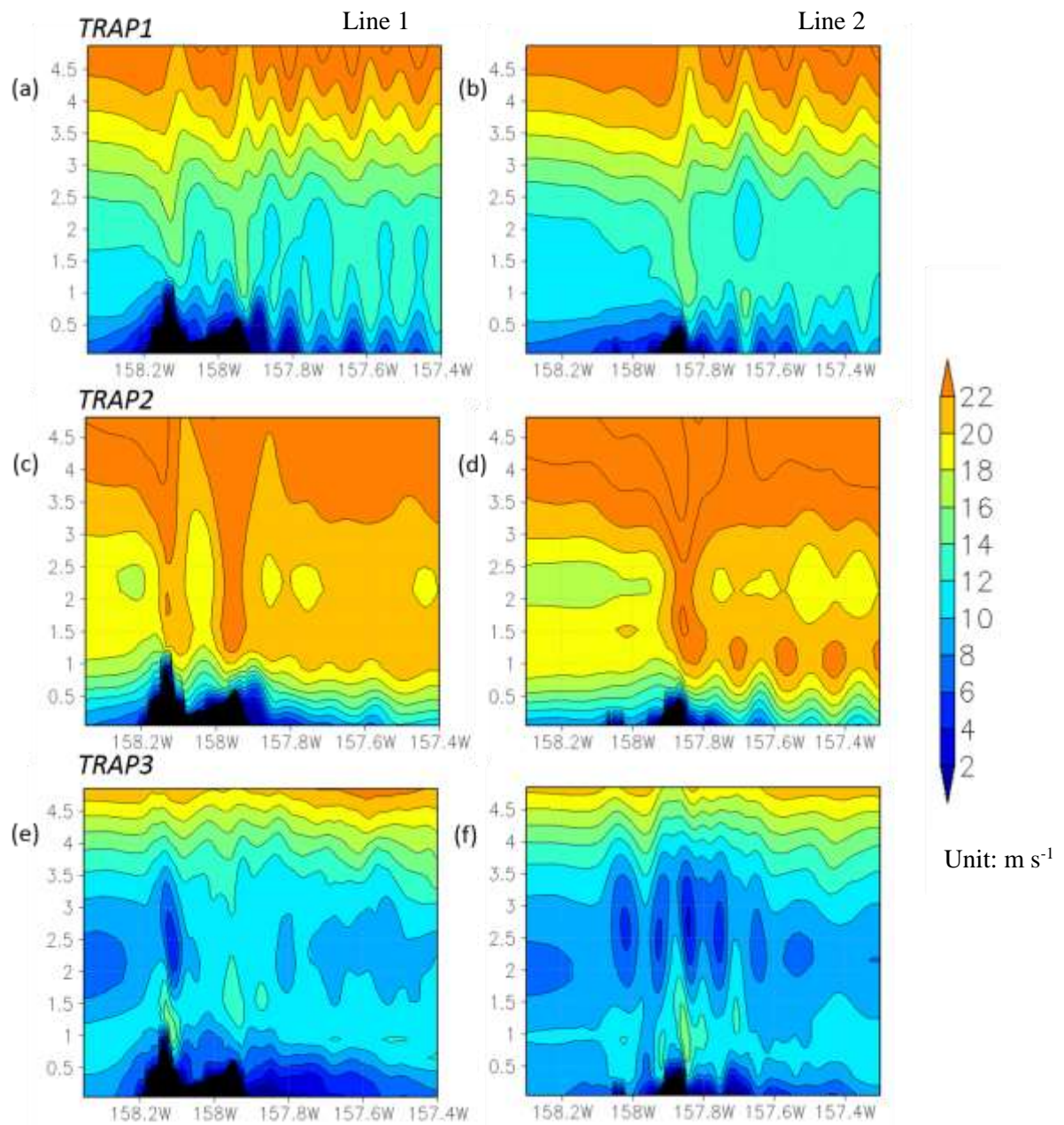


Figure 39. Model simulated cross-barrier wind speed (shading and contour) along vertical cross sections for trapped lee wave cases in wintertime. (a, b) TRAP1: 0300 UTC, 27 January 2010; (c, d) TRAP2: 2200 UTC, 24 January 2003; and (e, f) TRAP3: 2000 UTC, 26 January 2014. Figures in left column present the cross-barrier wind speed along transection line 1, and figures in right column are showing that along transection line 2.

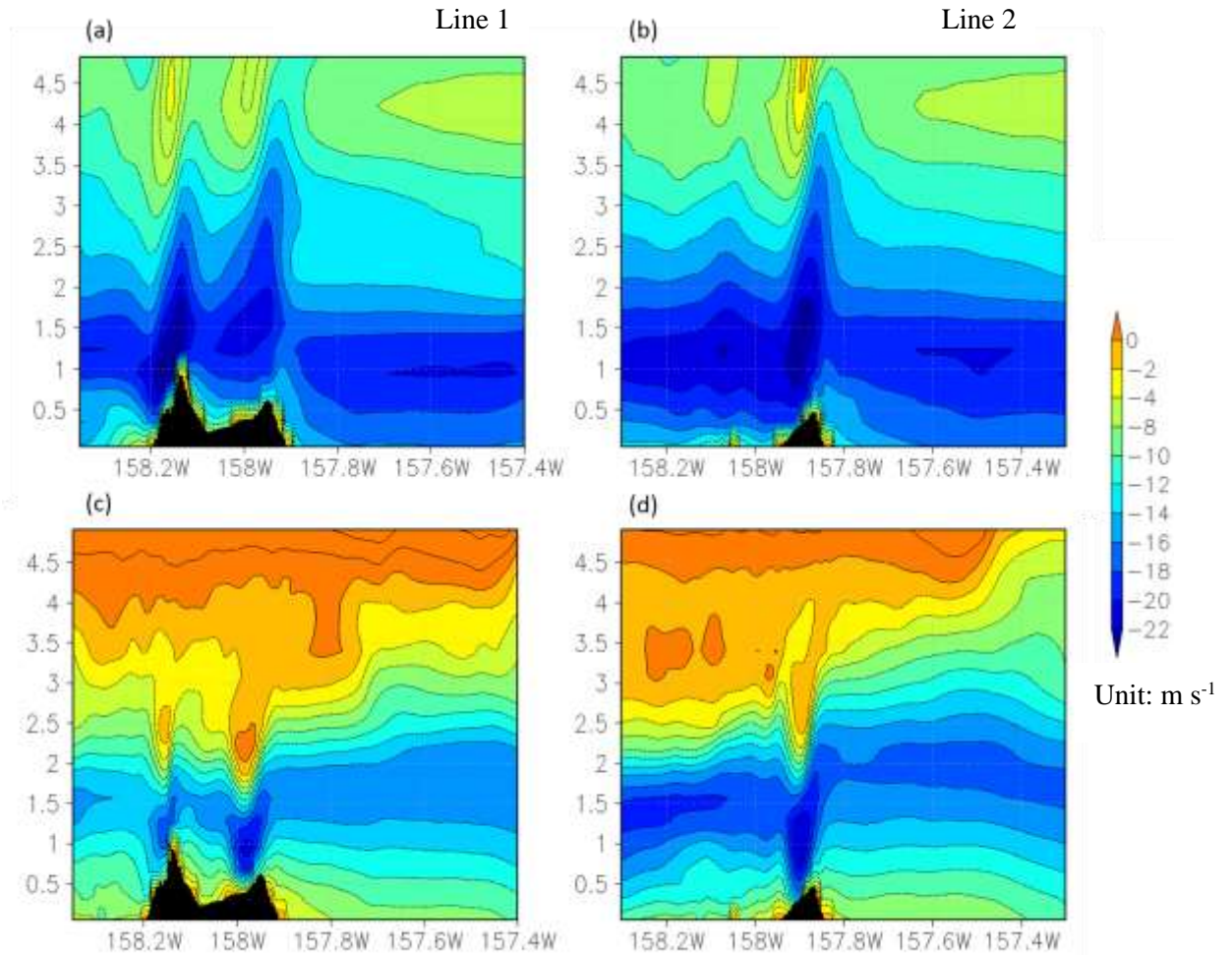


Figure 40. Model simulated cross-barrier wind speed (shading and contour) along vertical cross sections during the downslope wind case and the mountain wave case. (a, b) TRAP1: 0100 UTC, 15 February, 2001; and (c, d) 0000 UTC, August 01, 2013. Figures in left column present the cross-barrier wind speed along transection line 1, and figures in right column are showing that along transection line 2.

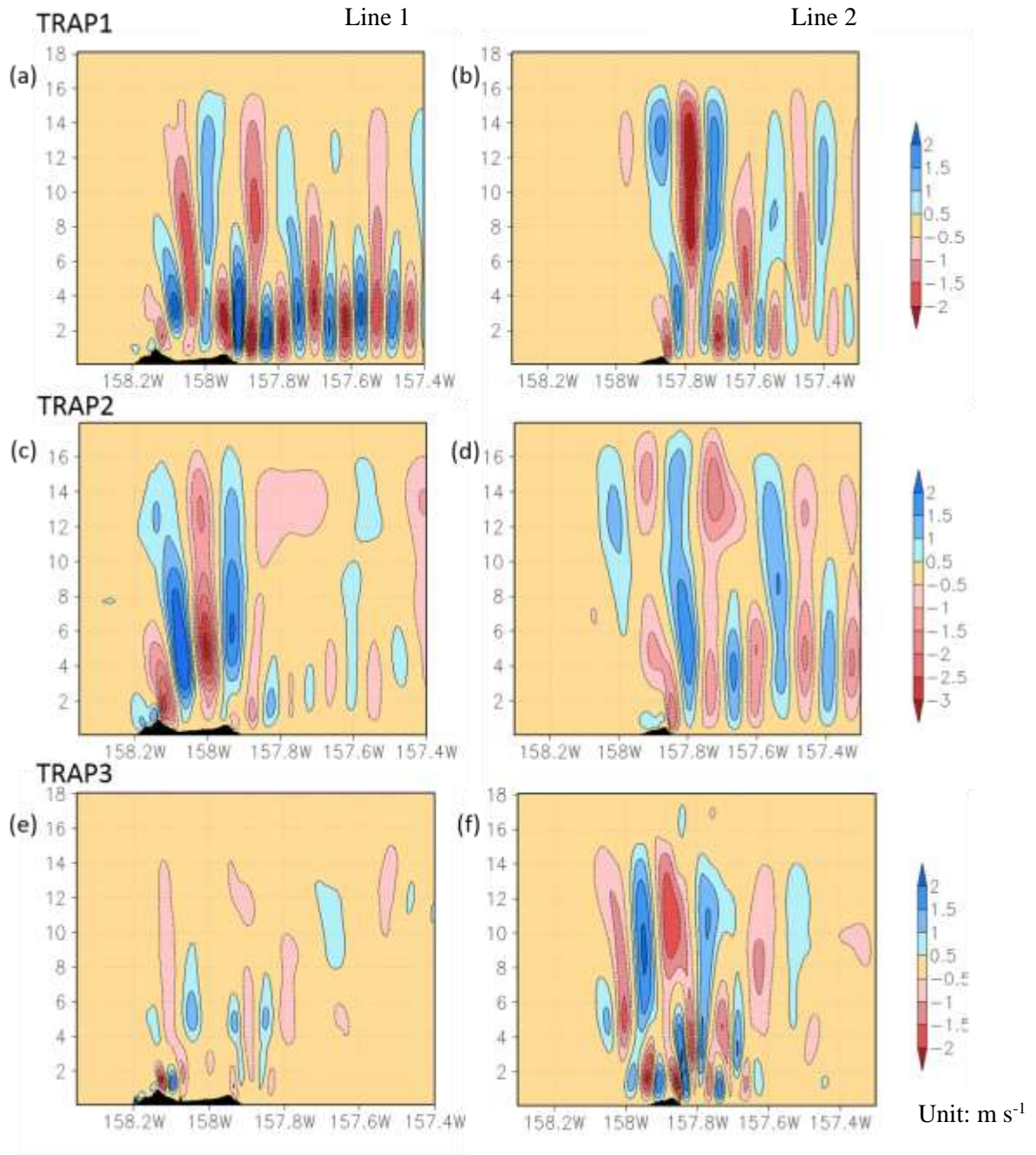


Figure 41. Model simulated w-component (shading and contour) along vertical cross sections for trapped lee wave cases in wintertime from surface to 18 km. (a, b) TRAP1: 0300 UTC, 27 January 2010; (c, d) TRAP2: 2200 UTC, 24 January 2003; and (e, f) TRAP3: 2000 UTC, 26 January 2014. Figures in left column present the cross-barrier wind speed along transection line 1, and figures in right column are showing that along transection line 2.

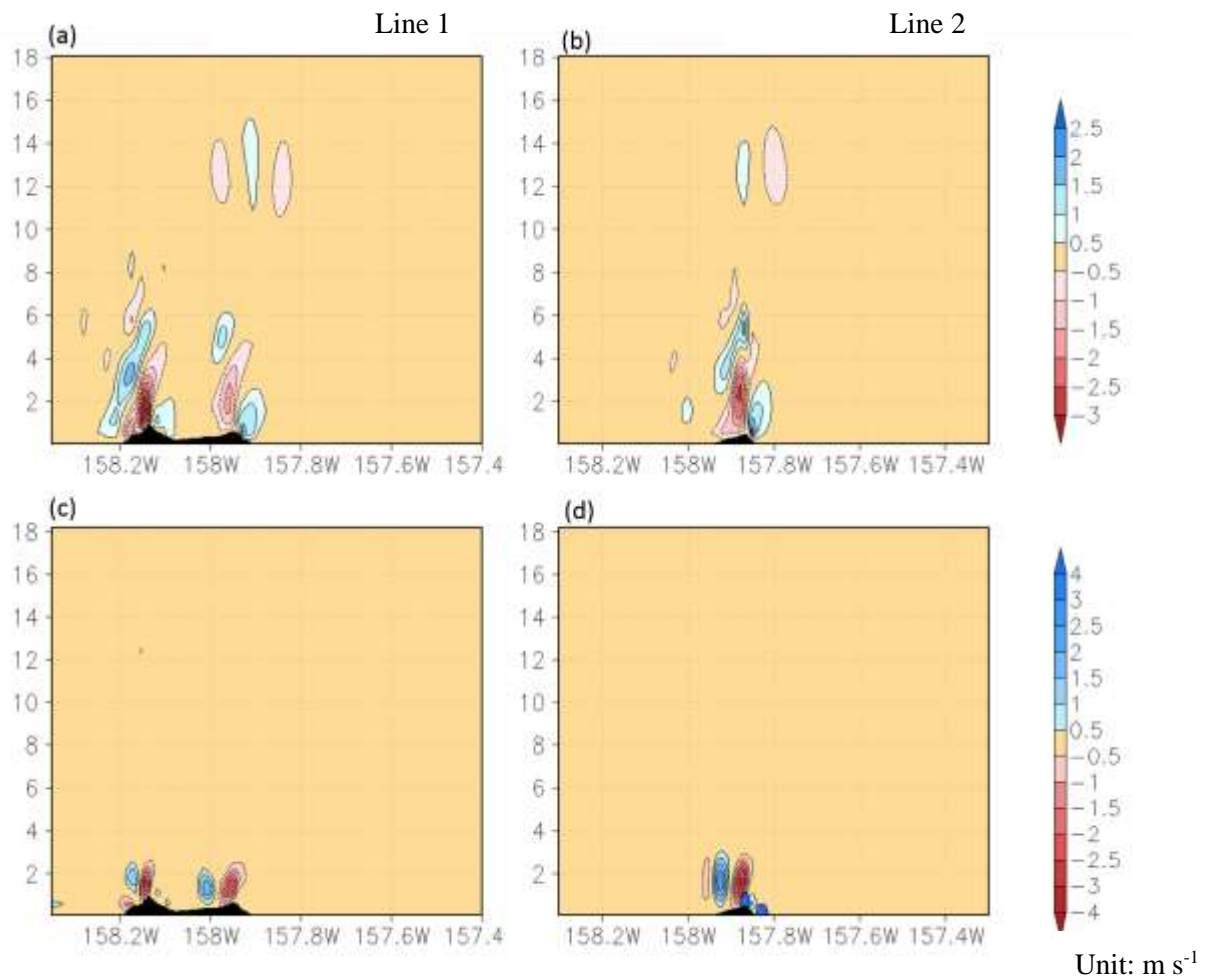


Figure 42. Model simulated w-component (shading and contour) along vertical cross section during downslope wind case and mountain wave case from surface to 18 km. (a, b) TRAP1: 0100 UTC, 15 February, 2001; and (c, d) 0000 UTC, August 01, 2013. Figures in left column present the cross-barrier wind speed along transection line 1, and figures in right column are showing that along transection line 2.

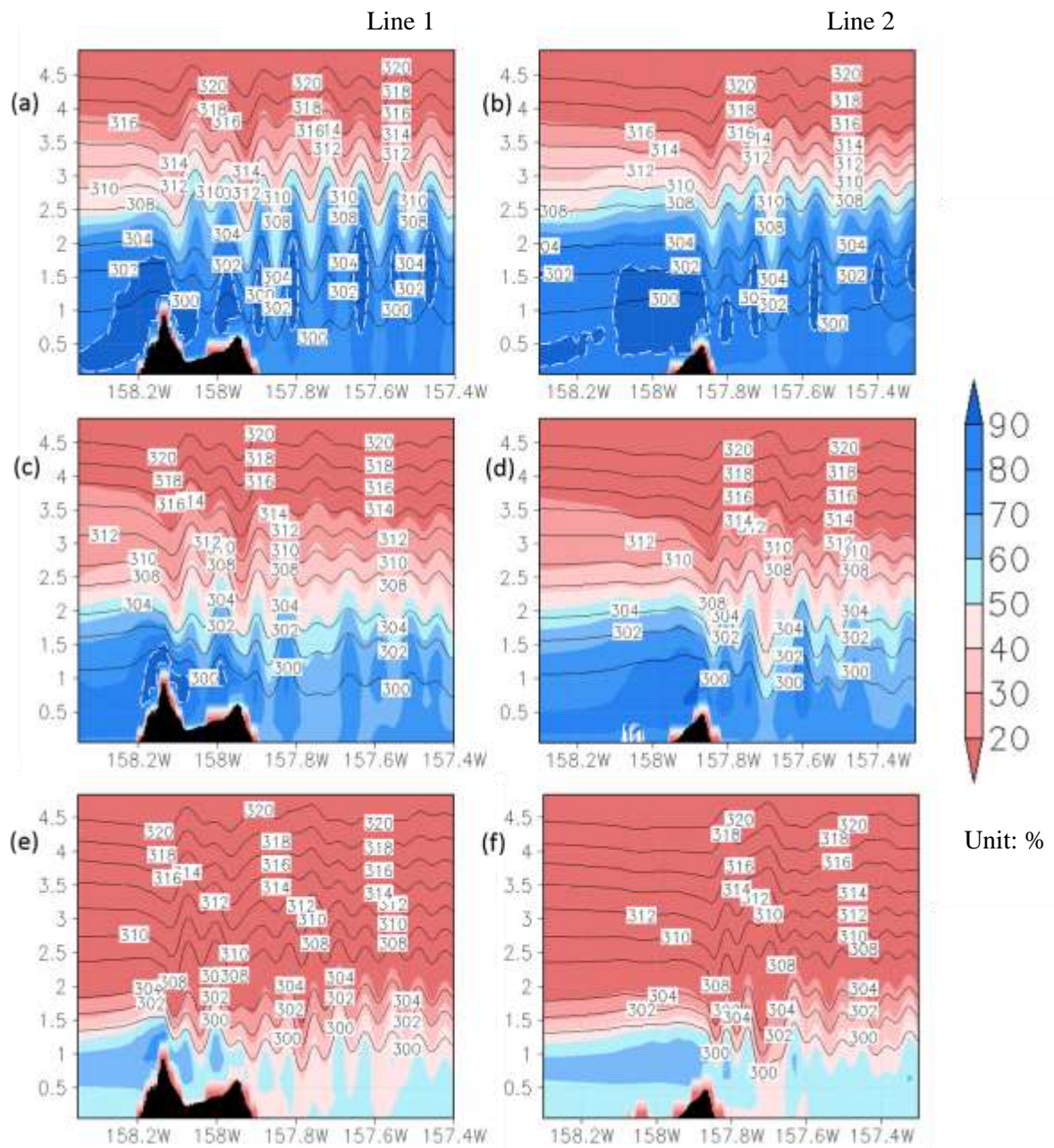


Figure 43. Time series of upstream airflow wavelengths in the unit of km. (a, b) control run without any change to relative humidity; RH80 (c, d) and RH30 (e, f) simulations with reduced relative humidity to 80% and 30% compared to the control run, respectively. The location of two vertical cross sections are shown in Figure 16.

	TRAP1	TRAP2	TRAP3
Moment	0300 UTC, 27 January 2010	2200 UTC, 24 January 2003	1800 UTC, 24 January 2014
Observed wavelength	12 km	18 km	10 km
Observed horizontal wave number k	0.52 km^{-1}	0.35 km^{-1}	0.628 km^{-1}
Calculated wavelength	6 km	10 km	4 km
Calculated horizontal wave number k	1.05 km^{-1}	0.628 km^{-1}	1.57 km^{-1}

Table 3. Observed wavelengths from satellite images and calculated wavelengths using equation (9), and corresponding horizontal wave number k for TRAP1, TRAP2 and TRAP3 cases.